

Electronic Properties of Low-Dimensional Materials Under Periodic Potential

Mehdi Jamei

Electrical Engineering and Computer Sciences
University of California at Berkeley

Technical Report No. UCB/EECS-2015-73

<http://www.eecs.berkeley.edu/Pubs/TechRpts/2015/EECS-2015-73.html>

May 13, 2015



Copyright © 2015, by the author(s).
All rights reserved.

Permission to make digital or hard copies of all or part of this work for personal or classroom use is granted without fee provided that copies are not made or distributed for profit or commercial advantage and that copies bear this notice and the full citation on the first page. To copy otherwise, to republish, to post on servers or to redistribute to lists, requires prior specific permission.

Electronic Properties of Low-Dimensional Materials Under Periodic Potential

By

Mehdi Jamei

A dissertation submitted in partial satisfaction of the
requirements for the degree of
Doctor of Philosophy
in
Engineering – Electrical Engineering and Computer Sciences
in the
Graduate Division
of the
University of California, Berkeley

Committee in charge:

Professor Alex Zettl, Chair
Professor Tsu Jae King
Professor Ali Javey
Professor Michael Crommie

Spring 2015

Electronic Properties of Low-Dimensional Materials Under Periodic Potential

Copyright 2015

by

Mehdi Jamei

Abstract

Electronic Properties of Low-Dimensional Materials Under Periodic Potential

by

Mehdi Jamei

Doctor of Philosophy in Electrical Engineering and Computer Sciences

Professor Alex Zettl, Chair

In the quest for the further miniaturization of electronic devices, numerous fabrication techniques have been developed. The semiconductor industry has been able to manifest miniaturization in highly complex and ultra low-power integrated circuits and devices, transforming almost every aspect of our lives. However, we may have come very close to the end of this trend. While advanced machines and techniques may be able to overcome technological barriers, theoretical and fundamental barriers are inherent to the top-down miniaturization approach and cannot be circumvented.

As a result, the need for novel and natural alternatives to replace old materials is valued now more than ever. Fortunately, there exists a large group of materials that essentially has low-dimensional (quasi-one- or quasi-two-dimensional) structures. Graphene, a two-dimensional form of carbon, which has attracted a lot of attention in recent years, is a perfect example of a prime material from this group. Niobium tri-selenide (NbSe_3), from a family of trichalcogenides, has a highly anisotropic structure and electrical conductivity. At sufficiently low temperatures, NbSe_3 also exhibits two independent “sliding charge density waves”—an exciting phenomenon, which could be altered by changing the overall size of the material.

In NbSe_3 (and Blue Bronze $\text{K}_0.3\text{MoO}_3$ which has a similar structure and electrical behavior), the effect of a periodic potential could be seen in creating a charge density wave (CDW) that is incommensurate to the underlying lattice. The required periodic potential is provided by the crystal ions when ordered in a particular way. The consequence is a peculiar non-linear conductivity behavior, as well as a unique narrow-band noise spectrum. Theoretical and experimental studies have concluded that the dynamic properties of resulting CDW are directly related to the crystal impurity density, and other pinning potentials. Therefore, reducing the overall size of the crystal could potentially alter the CDW behavior in a significant way.

Theoretical studies, as well as preliminary experimental results, suggest exceptionally interesting charge carrier behavior, including an energy gap opening and an anisotropic modulation of carrier mobility, in graphene when it is under a periodic potential. The fabrication process to achieve the desired periodic structure, with the required length scale on graphene is a challenging one. Therefore, in this manuscript, the fabrication process and its challenges are discussed.

The arrangement of the manuscript is as follows: In Chapter 1, first, I study the theory of charge density waves and their dynamics. Next, I describe the fabrication process for thin NbSe₃ and Blue Bronze crystals and devices. Finally, I discuss the device measurement results, and compare them with bulk crystals. In Chapter 2, I focus on the fabrication of periodic potentials on graphene layers. I begin by providing the theoretical background and motivations of the project. Then, the fabrication process is discussed in details. And lastly, I present the fabrication and preliminary electrical measurement results. Chapter 3 is a summary of additional experiments that I performed during the course of my PhD.

Contents

1. Finite-Size Effect on Charge Density Waves	
1.1. An Introduction to Charge Density Waves	1
1.1.1. Realization of CDW and its dynamics	2
1.1.2. Frequency dependent conductivity	7
1.1.3. Current oscillations, narrow-band and broad-band noise	9
1.1.4. Materials and CDW transitions	12
1.1.5. Motivations	16
1.2. Thin NbSe ₃ Crystals	18
1.2.1. Device Fabrication and Characterization	18
1.2.1.1. Crystal growth	18
1.2.1.2. Exfoliation technique	19
1.2.1.3. E-beam lithography and nitrogen plasma treatment	19
1.2.1.4. Electrical measurement methods	22
1.2.2. Results and Discussion	29
1.2.2.1. Exfoliation	29
1.2.2.2. Indium deposition	30
1.2.2.3. Contact resistance and plasma treatment	31
1.2.2.4. Device fabrication	32
1.2.2.5. Bulk crystal electrical measurements	33
1.2.2.6. Thin NbSe ₃ crystal measurements	36
1.2.3. Discussion and Conclusion	40
1.3. Thin Blue Bronze K _{0.3} MoO ₃ Crystals	45
1.3.1. Device Fabrication and Characterization	45

1.3.1.1. Crystal growth	45
1.3.1.2. Exfoliation technique	46
1.3.1.3. E-beam lithography and nitrogen plasma treatment	47
1.3.1.4. Electrical measurement methods	48
1.3.2. Results and Discussion	48
1.3.2.1. Exfoliation	48
1.3.2.2. Contact resistance and plasma treatment	48
1.3.2.3. Device fabrication	49
1.3.2.4. Preliminary Electrical measurements	49
2. Graphene Under Periodic Potential	
2.1. Theory and Background	51
2.1.1. Two-dimensional electron systems	52
2.1.2. Theory of Graphene	54
2.1.3. Effect of periodic potential on graphene	57
2.2. Device Fabrication	63
2.2.1. Exfoliation of graphene	63
2.2.2. CVD graphene growth and transfer method	64
2.2.3. Device fabrication strategies	68
2.2.4. Sub-15nm electron beam lithography	73
2.2.5. Metal-Oxide multilayer stack system	80
2.3. Results and discussion	84
2.3.1. Sub-15nm e-beam lithography	84
2.3.2. Metal-Oxide multilayer stack system	90
2.3.3. Conclusion and future experiments	90
3. Other Experiments	
3.1. C ₆₀ filled carbon and boron-nitride nanotubes	91
3.2. Single boron-nitride nanotube optical waveguide and transducer	95
4. Bibliography	99

Acknowledgements

First and foremost, I would like to thank Professor Alex Zettl, my advisor. His support and guidance has been a constant inspiration in my entire graduate studies life. During these years, discussions and consultations that I have had with him, have taught me new ways of thinking and problem solving skills, which have influenced me in both professional and personal level.

I would like to thank all Zettl group members who helped me in different parts of my experiments. Specifically, I would like to thank Dr. Claudia Ojeda-Aristizabal and Seita Onishi for their constant support.

I would also thank my parents and my two sisters. They always have been supporting me with their prayers and best wishes.

I would like to express my deepest gratitude to my parents-in-law, Shohreh Doustani and Mehdi Rajabzadeh, for their care, guidance and help. Thank you for providing me with an atmosphere of peace and love.

Finally, and most importantly, I would like to thank my wife, Shokoofeh Rajabzadeh, who has always been my unceasing inspiration. Her support, patience, and unwavering love have always been the dependable bedrock upon which, the past several years of my life have been built. In my most difficult times, she has always been there to cheer me up, and has stood by me through the good times and bad.

Chapter One

Finite-Size Effect on Charge Density Waves

1.1 An introduction to charge density waves

In 1955, and in independent attempts, Rudolf Peierls [1] and Herbert Fröhlich [2] predicted that in a one-dimensional electronic system, i.e. a one-dimensional metal, under a periodic potential, the electronic charge density undergoes a periodic modulation. This phenomenon was later called charge density waves (CDW). The periodic potential can be provided by either the lattice distortion or by an external potential. This chapter is a brief review of the properties of low-dimensional solids in a natural periodic potential from

their corresponding lattice distortions. It also covers some aspects of the sliding CDW dynamics [3-6].

1.1.1 Realization of CDW and its dynamics

In this section, when I talk about one-dimensional material, I do not refer to the overall size of the crystal. Here, I am discussing a form of crystal structure that allows the charge carriers to move easily in one direction, while at the same time, limits their movement in two other directions. An example of such crystals is transition metal trichalcogenides (e.g. NbSe₃), which I will discuss later. The atomic structure of this type of material is composed of infinitely long conductive chains, in which, the nearest-neighbor distance between atoms is comparable to that of a pure metallic crystal. However, these conductive chains are separated from each other by a far greater distance, and thus, are virtually independent. Such crystals are called quasi-one-dimensional (Q1D) materials. Similarly, quasi-two-dimensional materials (Q2D) could be understood. For example, graphite is a Q2D electronic system. As will be discussed later, CDW appears in low-dimensional conductors (i.e. Q1D or Q2D material) at sufficiently low temperatures.

In order to model a one-dimensional metal in a periodic potential, first, consider a nearly free electron gas (NFE) in a periodic potential. The periodic potential can be written as

$$V = \Delta e^{iQx}. \quad (1.1)$$

Here, Δ is the potential amplitude, and Q is the wave vector [7]. The real part of this potential is shown in Figure 1.1. Applying this potential as a perturbation potential, on a free electron gas system, results in the coupling of $|k\rangle$ and $|k + Q\rangle$ states. This coupling opens an energy gap at $k = \pm Q/2$. The energy of this gap can be easily calculated as $E_g = 2\Delta$.

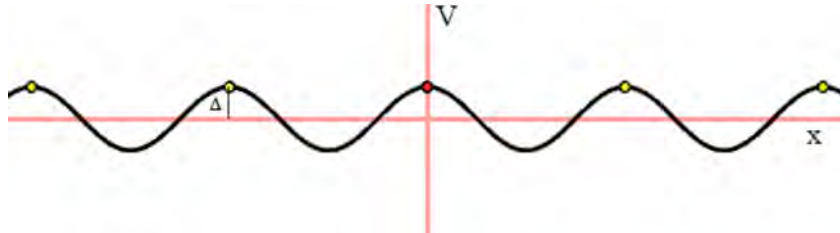


Figure 1.1: A periodic potential with amplitude Δ . If applied on a Q1D material, this potential forms a CDW at low temperatures.

Such a periodic potential can be provided by displacement of lattice ions, as shown in Figure 1.2. In this displaced ion system, the electronic charge density can be perturbed by a phonon with the wavenumber q , where q is the corresponding wavenumber of ion displacement. In a special case of $q = 2k_F$, where k_F is the Fermi wavenumber, the energy gap opening results in a reduction in the total energy of the electronic and lattice system [8]. Hence, the ions favor this new position, and thus, lock into it.

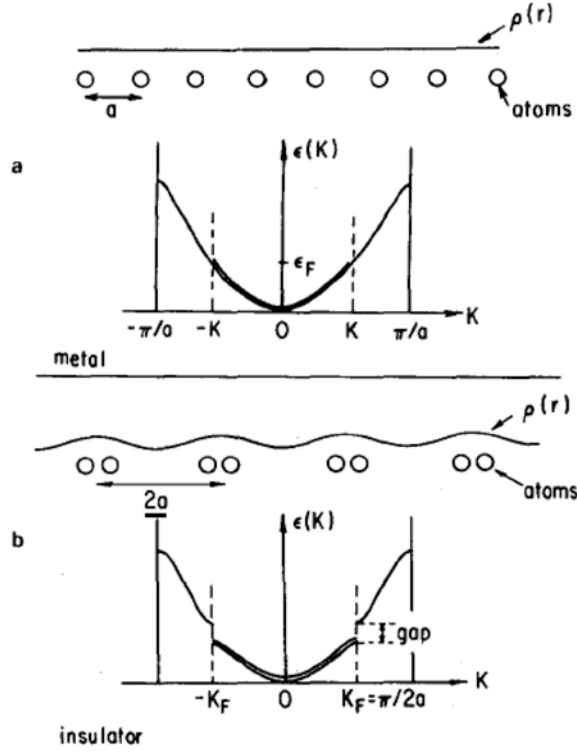


Figure 1.2: Peierls transition in a one-dimensional electron gas. (a) Undistorted lattice, (b) distorted lattice which cause a gap opening in the single particle excitation spectrum [8].

The effect of this interaction on the charge density can be written as $\delta\rho = -\chi(q)V(q)$, where $\chi(q)$ is the electronic susceptibility, and $V(q)$ is the mean-field potential of the phonons. The mean field potential for ion displacement phonons can be written as

$$V(q) = gU_0 e^{iqx} \quad (1.2)$$

where g is the electron-phonon coupling constant, and U_0 is the displacement amplitude. In comparison with relation 1.1, $\Delta = gU_0$.

Lindhard function gives the electron susceptibility as

$$\chi(q) = \sum_k \frac{f(k) - f(k+q)}{E(k+q) - E(k)} \quad (1.3)$$

where $f(k)$ is the temperature-dependent Fermi-Dirac distribution function, and $E(k)$ is the electronic energy at k . The sum goes on all the occupied states [9]. Figure 1.3 (a) shows the real part of the Lindhard function for a one-dimensional Nearly Free Electron Gas (NFEG) at $T = 0$ [10]. For simplicity, it is assumed that $\hbar = e = m = k_F = 1$. As

indicated in this plot, $\chi(q)$ diverges logarithmically near $q = 2k_F$. This is a unique characteristic of this function in 1D. In 3D, however, calculating $\chi(q)$ results in a characterless function of q . This function is displayed in Figure 1.3 (b)

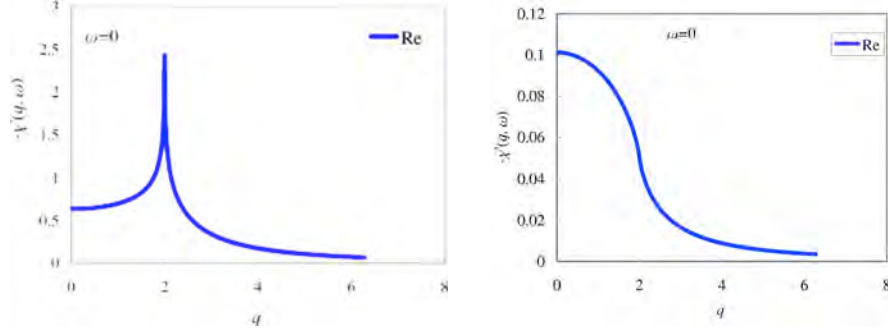


Figure 1.3: The real part of the Lindhard function for (a) one-dimensional, and (b) three-dimensional nearly free electron gas (NFEG) as a function of wavenumber q . For simplicity it is assumed that $\hbar = e = m = k_F = 1$. This shows that $\chi(q)$ diverges logarithmically near $q = 2k_F$. This divergence is responsible for the creation of CDW [10].

The physics of this singularity can be understood by noting that, in a one-dimensional metal, all Fermi states with $k < 0$ can be translated to their corresponding $k > 0$ states by a single wave vector $q = 2k_F$. This unique translation is called nesting of the Fermi surface. The total nesting of the Fermi surface is a unique characteristic of 1D systems. In higher dimensions, even though, a large electron susceptibility behavior could occur at $2k_F$, and thus, nest a significant fraction of the Fermi surface, however, total nesting phenomenon never occurs. Therefore, in low-dimensions, charge carriers are strongly responsive to the $2k_F$ phonon mode.

As mentioned before, the $2k_F$ peak in $\chi(q)$, which also exists at $T > 0$, can strongly modulate electronic charge density at $2k_F$. The electronic force from this modulation is given by $F = -2g^2\chi U_0$. This force acts on the ions and tries to increase their displacement and hence reduce the phonon frequency $\omega(2k_F)$. By considering this effect and noting that the electronic force function is equivalent to that of a simple harmonic oscillator, the $2k_F$ phonon frequency becomes [7]

$$\omega^2(2k_F) = \omega_0^2 - \frac{2g^2\chi(2k_F)}{M} \quad (1.4)$$

where ω_0 is the initial $2k_F$ phonon energy and M is the ionic mass.

As the temperature decreases, $\chi(2k_F)$ will increase, until, at a critical temperature where $\chi(2k_F) = M\omega_0^2/2g^2$, the $2k_F$ phonon frequency $\omega(2k_F)$ becomes zero. This temperature is called the Peierls transition temperature or T_c^{MF} . Therefore, at the Peierls transition temperature, the lattice ions lock in their new position, and create charge density waves.

Also, at T_c^{MF} an energy gap of $E_g = 2\Delta$ forms at the Fermi surface. Because this gap opens up at $E = E_F$, it reduces the total energy of the electrons. This reduction in the electronic energy, balances out by an increase in the elastic energy of the crystal, due to the permanent displacement of ions. It is a straightforward calculation to minimize the total lattice + electrons energy and find Δ [7]

$$\Delta = 2E_F e^{-1/\lambda} \quad (1.5)$$

Here, $\lambda = D(E_F)g^2/M\omega_0^2$, and is a dimensionless coupling constant, where $D(E_F)$ is the density of states (DOS) at the Fermi energy. Using the temperature dependent form of $\chi(2k_F)$, Δ can be calculated in terms of T_c^{MF} , which is the famous BCS superconductivity relation:

$$2\Delta = 3.52 k_B T_c^{MF} \quad (1.6)$$

where k_B is the Boltzman constant.

This analysis has neglected the inter-chain coupling and three-dimensional ordering. Lee, Rice and Anderson [11] has shown that by considering those effects, the Peierls transition temperature is much lower; because the three-dimensional ordering does not occur above $T_c \approx T_c^{MF}/4$. In fact T_c^{MF} can be considered the transition temperature for each individual metallic chain in the crystal network. However, in order for the macroscopic effect to be observed, all chains have to transit to the CDW state. This total transition happens at T_c , and it is this temperature that is measured in the lab.

As discussed above, the Peierls transition in a metal opens an energy gap at E_F . Therefore, the metal makes a transition to semiconductor at the Peierls transition temperature. Also, it is important to note that, the periodicity of CDW wave $\lambda = \pi/k_F$ can be imagined to be independent of the lattice periodicity [2]. In this case, the CDW is called incommensurate with the lattice. This phenomenon had been a very promising model to describe superconductivity, before the BCS model. Frohlich's superconductivity theory was based on CDW states that could slide with no or minimum resistance from the underneath lattice. In this picture, the ions would fluctuate around their permanent position, and thus, would not contribute to the macroscopic current. However, this ionic fluctuation would significantly increase the CDW effective mass. Consequently, this effectively heavy charge waves would carry the supercurrent.

Peierl and Fröhlich's intriguing CDW and superconductive mode was not verified experimentally, until the early 1970's. Until then, no quasi-one- or quasi-two-dimensional material was known. The first Q1D material that Peierl's transition was observed in, was $K_2Pt(CN)_4Br_{0.3}(KCP)$, which consists of linear chains of potassium salt [12]. Organic charge-transfer salts (e.g. TTF-TCNQ) were also shown to undergo the Peierl's transition [13].

Monceau et al. observed the first sliding CDW in 1976 [14]. $NbSe_3$, a linear chain conductor, which undergoes two separate Peierl's transition at $T_{c1}=144$ K and $T_{c2}=59$ K, was observed to exhibit a non-linear dc conductivity in its both CDW states. It is worth to mention that, both $NbSe_3$ Peierl's transitions open a partial gap in the Fermi surface, and hence, the material still behaves metallically after the transition. Figure 1.4 shows the normalized resistance of $NbSe_3$ as a function of temperature in both Peierl's transitions.

As indicated in this figure, by increasing the bias voltage (or the current density), both non-linear anomalies in the resistance become less noticeable, and in a very large dc electric field, the resistivity saturates to its linear value. In the beginning, this phenomenon was explained in terms of the single particle Zener tunneling across the small CDW energy gap [14]. However, afterwards, X-ray diffraction experiments showed that Zener tunneling explanation is not correct, and CDW does not break down in the non-linear regime [15].

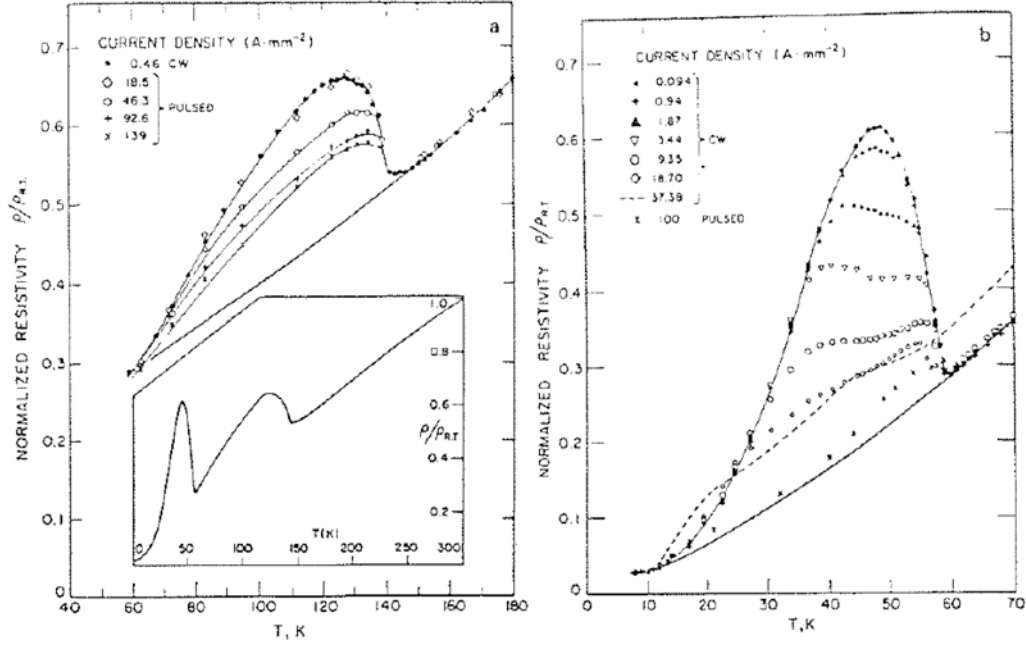


Figure 1.4: The dc electrical resistance of NbSe₃ as a function of temperature in both upper (a) and lower (b) Peierls states for various dc current biases. The inset in (a) is the dc resistivity in the low-field limit as function of temperature down to 4.2K. [14]

Ultimately, in 1979, Bardeen suggested that, as Frohlich predicted, the sliding CDW could be responsible for the non-linear resistivity of NbSe₃ [16]. Subsequently, differential resistance measurements verified this theory, by showing that the threshold field, E_T , at which the non-linearity begins, is a strong function of temperature [17-18]. The threshold field E_T , separates the Ohmic linear and non-Ohmic non-linear regions in current versus voltage characteristics of sliding CDW materials. This is shown in Figure 1.5. The reason that the threshold field is non-zero, or in other words, no Frohlich superconductivity mode is observed, is that the lattice impurities pin down the CDW [19].

In the case of NbSe₃, the non-linear dc conductivity could be described by the empirical expression [20]

$$\sigma_{dc}(E) = \sigma_A + \sigma_B \left(1 - \frac{E_T}{E}\right) e^{-\frac{E_0}{E-E_T}} \quad (1.7)$$

Here, σ_A is the linear Ohmic conductivity, and σ_B and E_0 are fitting parameters.

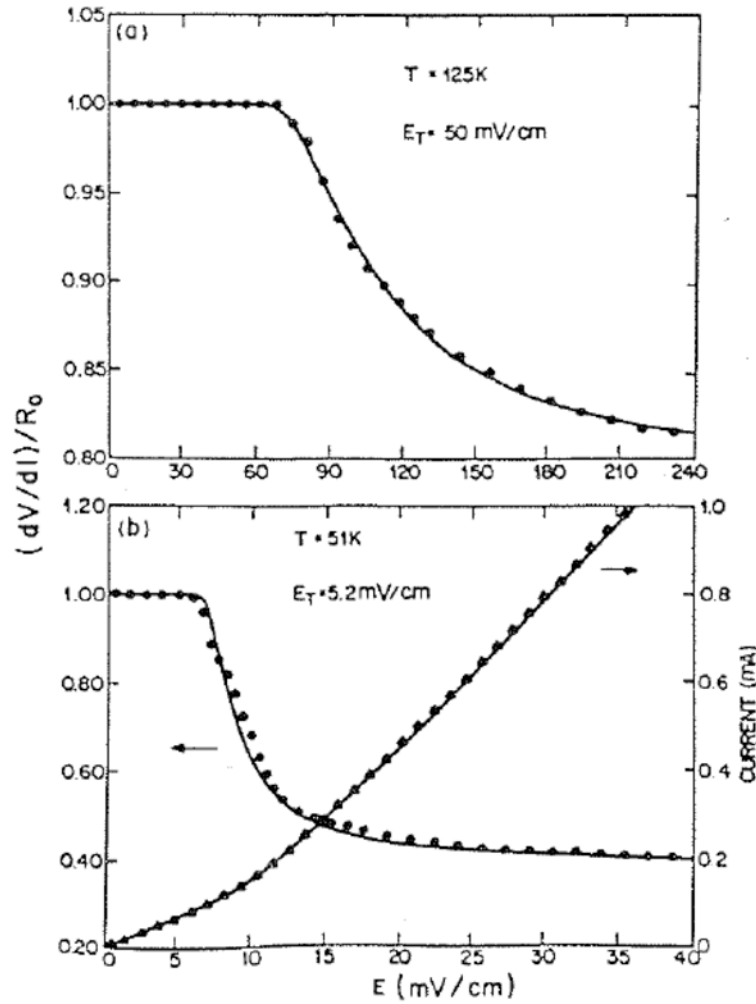


Figure 1.5. Differential resistance and current-voltage curve of NbSe₃ in both 144 K (a) and 59 K (b) CDW states. The solid lines are fitted to Fleming's empirical expression 1.7 [18].

The next section is a brief summary of dynamical properties of sliding CDW.

1.1.2 Frequency dependent conductivity

Figure 1.6 shows the frequency dependence of the electrical conductivity of NbSe₃ and TaS₃ [21-22]. In both materials, an increase in the real part of the conductivity starting from 1-10 MHz region is observed. The real part of the conductivity saturates to a maximum value in 1-10 GHz region. In both cases, the conductivity becomes zero in the microwave domain ($>10^3$ GHz). This strong frequency dependence could also be observed in the imaginary part of the conductivity. This is shown in Figure 1.7, which suggests an overdamped simple harmonic oscillator model. The characteristic crossover frequency ω_{CO} , has been shown to increase with increasing the impurities in the crystal.

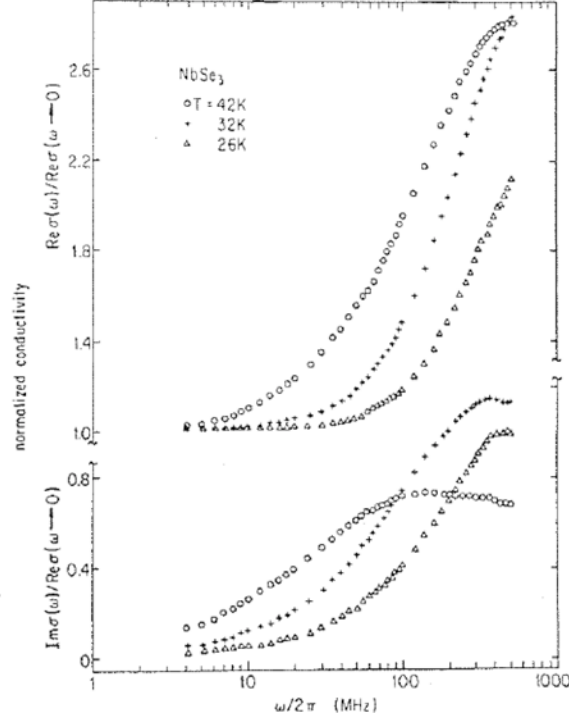


Figure 1.6: Real and imaginary parts of the electrical conductivity of NbSe₃ as a function of frequency [21].

This impurity concentration dependence is similar to that of the threshold electric field E_T . This similarity suggests that the peak in the real part of the conductivity versus frequency originates from a collective-mode excitation of charge density waves [23]. The conductivity dependence in low-frequency regime is a characteristic behavior of all sliding CDW materials.

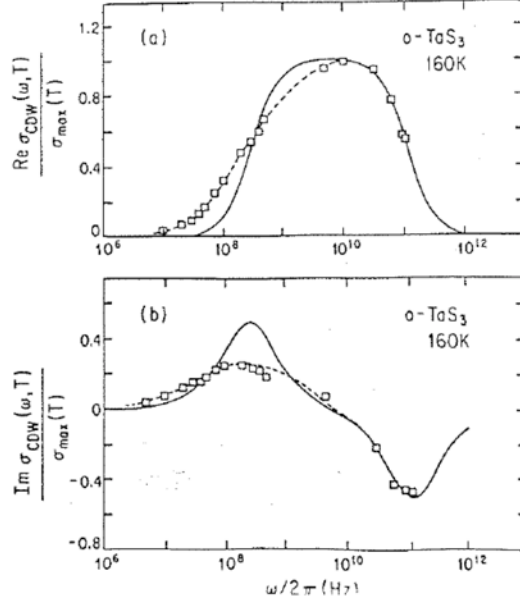


Figure 1.7: Normalized real and imaginary parts of the frequency dependent conductivity of TaS₃. The experimental data are fitted to an overdamped simple harmonic oscillator with a single relaxation time (solid line) and a distribution of relaxation times (dashed line). [22]

1.1.3 current oscillations, narrow-band and broadband noise

In 1979, Fleming and Grimes observed the current oscillations and narrow-band noise phenomena in sliding charge density wave systems [17]. Conduction “noise” is one of the most peculiar and interesting phenomena associated with sliding CDW. For electric fields above E_T , a sliding CDW system current response, in addition to the dc CDW current, contains an unusually large amount of broadband noise, and also coherent ac current oscillations. Fourier analysis on these coherent current oscillations reveals very sharp frequency components. Figure 1.8 shows a typical coherent current oscillation spectrum in NbSe₃, when biased above E_T . Sharp peaks in this spectrum are referred to as narrow band noise (NBN). A typical current oscillation spectrum contains a fundamental noise peak at f_{NBN} and several harmonics of f_{NBN} at $f = nf_{NBN}$ where $n = 1, 2, 3, \dots$, and the amplitude of harmonic peaks decreases as n increases.

An important observation regarding narrow-band noise is the linear relation between the fundamental noise frequency f_{NBN} and the dc current density of CDW. The excess current due to the sliding CDW can be written as $I_{CDW} = V_{dc}(\frac{1}{R} - \frac{1}{R_0})$, where V_{dc} is the applied voltage, R is the field-dependent sample resistance, and R_0 is the low-field Ohmic resistance of the sample. Therefore, we may write CDW current density J_{CDW} as a function of f_{NBN} .

$$J_{CDW} = cf_{NBN} \quad (1.8)$$

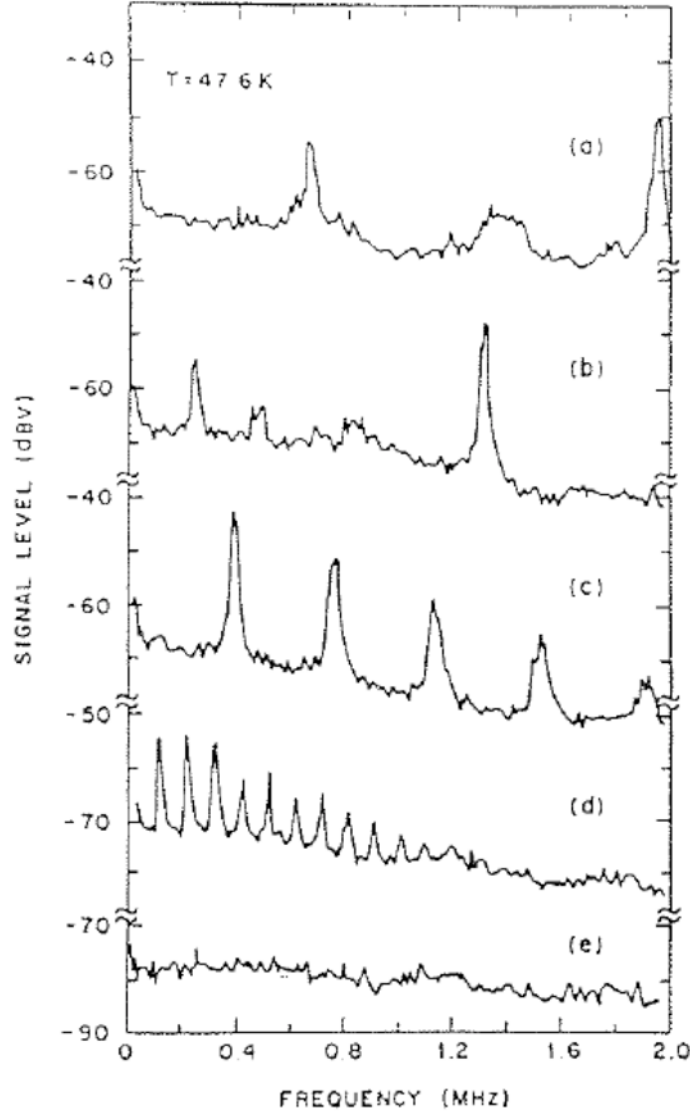


Figure 1.8: Noise spectra of sliding CDW in NbSe₃ crystal for various bias currents: (a) I=270 μA, (b) I=219 μA, (c) I=154 μA, (d) I=123 μA and (e) I=0 [17].

Here, c is a constant, which is a function of the type and quality of material, and temperature. Monceau et al. first proposed this relation. [24]

Figure 1.9 shows the experimental evidence of this linear relation. In this experiment, the fundamental noise frequency is plotted as a function of CDW current density, for NbSe₃ crystals in different temperatures [24].

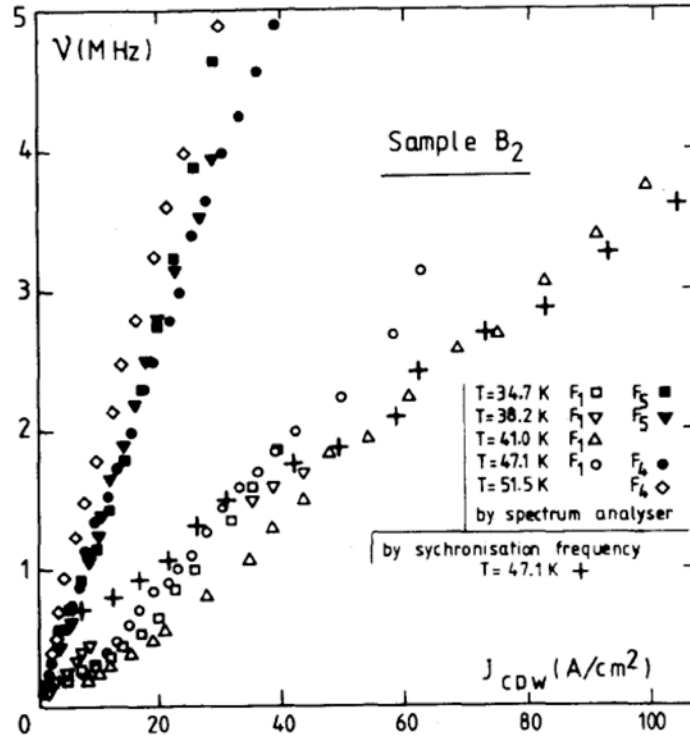


Figure 1.9: Noise frequency as a function of CDW current density for NbSe₃ for various temperatures. F₁ is the fundamental frequency. [24]

The narrow-band noise phenomenon can be explained by considering the interaction of the sliding CDW with the pinning periodic potential made by impurities in the crystal. [25]. In order to understand the periodic nature of the pinning potential, it worth noting that “displacing the CDW by one period, results in the same energy configuration.” [8]. Therefore, the periodicity of the pinning potential is $Q_p = 2\pi/\lambda$. In a classical single particle theory, this potential results in the following equation of motion:

$$\frac{d^2x}{dt^2} + \frac{1}{\tau} \frac{dx}{dt} + \frac{\omega_0^2}{Q_p} \sin Q_p x = \frac{eE}{m^*}$$

This is a model for a “charged particle in a sinusoidal potential tilted by the applied electric field.” [8] Figure 1.10 shows a schematic of such a potential. This model could explain variety of experimental data, including the narrow band noise behavior. The moving charge particles create an electrical current that has a clear time-dependence as they change speed in moving along the staircase potential.

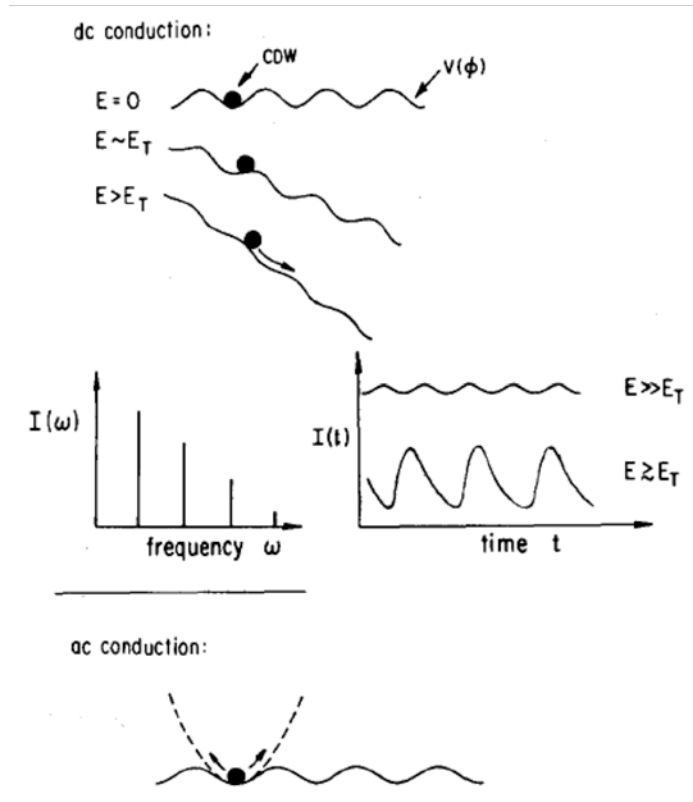


Figure 1.10: Classical model for CDW transport. In this model a charge particle is moving in a sinusoidal potential resulting from the pinning impurities. Finite E_T , NBN characteristics and ac conduction behavior in CDW materials can be described with this model. [8]

1.1.4 Materials and CDW transitions

In this manuscript, static and dynamic properties of $K_{0.3}MoO_3$ and $NbSe_3$ thin crystals have been examined. In the following subsections the structure and electronic properties of these two materials are presented.

Transition metal trichalcogenides, $NbSe_3$

The transition metal trichalcogenides, MX_3 , with $M=Nb$ or Ta and $X=S$ or Se are classified as quasi-one-dimensional crystal structures. In $NbSe_3$, as shown in Figure 1.11 (a), trigonal prisms stack end-to-end to form infinite chains. Niobium atom is located at the center of each selenium prism [28-29]. The axis parallel to chains is the b axis of crystal structure. All chains in the c direction are linked together via Nb-Se bonds. These bonds have ionic-covalent nature, and form slabs or ribbons in b and c directions.

A $NbSe_3$ unit cell has a monoclinic structure, and consists of six prismatic units. This is depicted in Figure 1.11 (b), where the six distinctive prisms are labeled. “In type III

chains, each unit is rotated by 180° and displaced by $b/2$ with respect to the adjacent one.” [28] These units are grouped based on the distance between the selenium pairs. In type III, the Se-Se distance is 2.37\AA , and thus has the strongest pairing. Type II has the weakest pairing (Se-Se distance is 2.91\AA), and type I has the intermediate pairing (Se-Se distance is 2.49\AA).

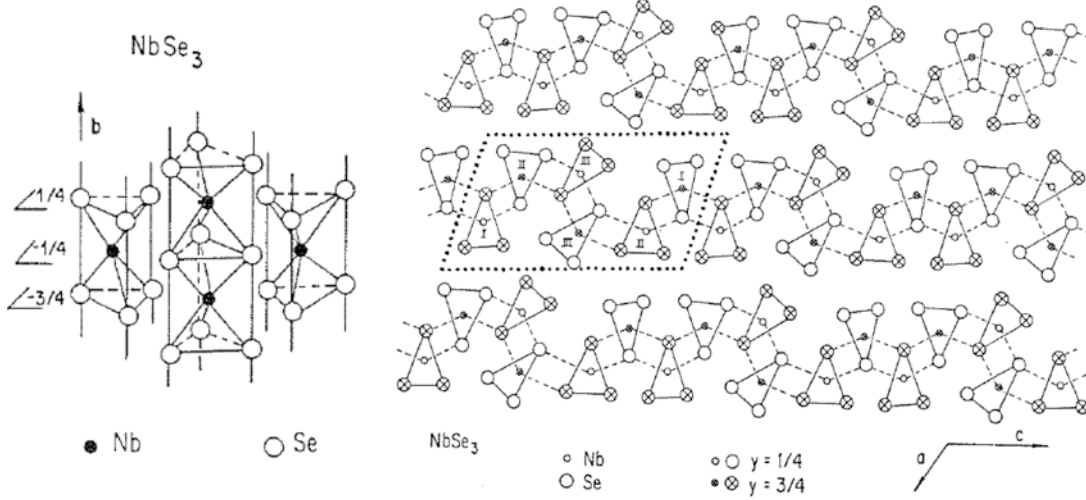


Figure 1.11: (a) The chain structure of NbSe₃. The b axis is parallel to the chains. (b) NbSe₃ crystal structure projected on the a-c plane. A unit cell is highlighted by the dotted line. This includes a pair each of the three chain types [28-29].

The band filling of NbSe₃ strongly depends on the bond nature of the three types of basis chains, and is as follows [30-31]: Each cation (niobium in this case) has 5 valence electrons, and therefore, there are 30 valence electrons per unit cell. The four chains with stronger Se-Se bond (i.e. type III and I) fill up 4×2 electrons for Se_2^{2-} , and 4×2 electrons for Se^{2-} , i.e. the total of 16 electrons. The two chains with weaker Se-Se bonds (i.e. type II) account for $2 \times 6 = 12$ electrons. The remaining 2 electrons are shared across four Nb atoms (0.5 electron each), which in a one-dimensional system, translates to a quarter-filled band.

The room temperature conductivity of NbSe₃ along the chain axis (i.e. the b-axis), is high with the value of $\sigma_{||} \sim 4 \times 10^3 \Omega^{-1} \text{cm}^{-1}$ [32-34]. However, the transverse conductivity (i.e. along a and c axis) is almost an order of magnitude lower. This is a quality of a moderately anisotropic compound.

Two Peierl's transitions have been observed in NbSe₃. The first transition at $T_{c1} = 144\text{K}$, forms a CDW that is incommensurate, and the corresponding wavevector is $Q_1 = (0, 0.243, 0)$ [15]. The second Peierl's transition at $T_{c2} = 59\text{K}$, creates another independent CDW which is also incommensurate, and its corresponding wavevector is $Q_2 = (0.5, 0.259, 0.5)$. As discussed before, neither of these transitions can fully nest the Fermi surface, and consequently, NbSe₃ stays metallic even below CDW transition temperatures. There are numerous experimental evidences [35-37] suggesting the existence of the CDW mode, exclusively in type III chains. The reason is the highly one-

dimensional structure of these chains. Therefore, type I and type II chains remain ungapped, and thus, the overall characteristic of the crystal remains metallic.

Potassium Molybdenum blue bronze $K_{0.3}MoO_3$

Ternary transition metal oxides are a class of materials, which have the common chemical form of A_xT_yO , where A is an alkali metal, and T is a transition metal. In this class, a group of colored bronzes show exciting electronic properties.

The red bronze $K_{0.33}MoO_3$, which is a semiconductor across all temperatures [38], and the purple bronze $K_{0.9}Mo_6O_{17}$, which is a metal with a Peierl's transition at $T = 120 K$ [39], both have a quasi-two-dimensional structure. However, potassium and rubidium blue bronzes ($K_{0.3}MoO_3$ and $Rb_{0.3}MoO_3$ respectively), have quasi-one-dimensional structures, are metallic at room temperature, and exhibit Peierl's transitions [40-41]. In $K_{0.3}MoO_3$ and $Rb_{0.3}MoO_3$, the CDW mode occurs at $T_c = 180 K$, and the CDW is incommensurate to the lattice. Here, I review the electronic properties of potassium blue bronze $K_{0.3}MoO_3$ in more details.

The first thorough investigation on Potassium blue bronze $K_{0.3}MoO_3$ was conducted in 1981 [42]. The X-ray diffraction, dc electrical measurements [42], and the optical reflectivity [43] experiments concluded that this material is a quasi-one-dimensional metal at room temperature, and undergoes a metal to semiconductor transition at $180 K$. Furthermore, this transition was linked to the Peierl's transition and the formation of an incommensurate charge density wave [44]. Other unique transport properties of sliding CDW such as non-linear transport and narrow-band noise oscillations were also observed in potassium blue bronze, and were explained successfully within the collective CDW motion scheme [45].

The blue bronze crystal is a side-centered monoclinic structure with the space group $c2/m$ [46-48]. This material is made of infinite sheets of MoO_6 octahedra separated by potassium ions. The MoO_6 octahedra, are packed in groups of ten, and these groups are joined at the corners in $[010]$ and $[102]$ directions. Therefore, the blue bronze consists of infinitely long chains along the b axis, which also create a weakly connected sheet structure in the $[101]$ direction. This is shown in Figure 1.12 (a). Three distinguished types of MoO_6 octahedra are present in the blue bronze unit cell, which can be identified by their relative positions within the unit cell. This is depicted in Figure 1.12 (b).

At room temperature, blue bronze, conducts almost an order of magnitude better along the b-axis, than along the a- or c-axis. The conductivity along the b-axis is $\sigma_{||} \sim 7 \times 10^3 \Omega^{-1} cm^{-1}$ [49]. This anisotropy in conductivity is comparable to that of $NbSe_3$.

Figure 1.13 shows the resistance of the potassium blue bronze $K_{0.3}MoO_3$ as a function of $1/T$. Below the Peierl's transition temperature, $K_{0.3}MoO_3$ follows the typical temperature dependence of a semiconductor [42,51]. Diffuse X-ray experiments strongly support the formation of CDW below this transition temperature. From the strong satellite optical reflection, the reduced wavevector of $Q=(0, 0.74, 0.5)$ [44] can be calculated for the created CDW. From dc transport, the deduced energy gap is $2\Delta \approx 8k_B T_c$. This is in rough agreement with equation 1.6. It is worth noticing that $T_c \approx T_c^{MF}/4$ [50].

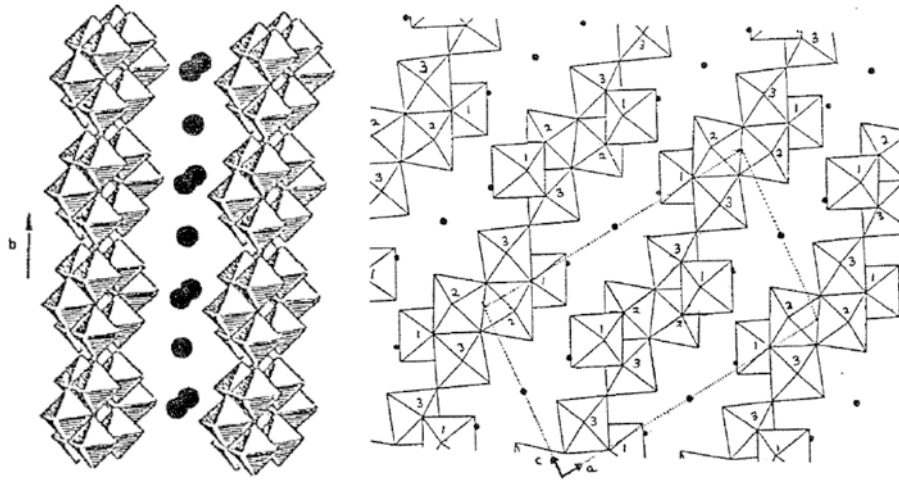


Figure 1.12: (a) Infinite chains of MoO₆ octahedra along the b-axis in the blue bronze K_{0.3}MoO₃ structure. These chains are separated by potassium ions. (b) K_{0.3}MoO₃ crystal structure in a-c plane. The side-centered monoclinic unit cell is shown by the dotted lines. Three different kinds of MoO₆ octahedra are indicated by numbers (1, 2 or 3) [48].

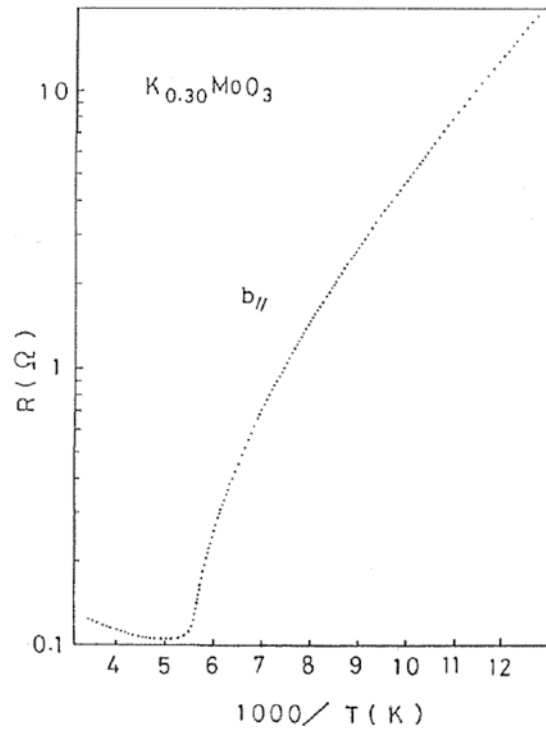


Figure 1.13: The b-axis electrical resistance of potassium blue bronze K_{0.3}MoO₃ as a function of $1/T$ [51].

By comparing the dc resistance versus temperature data for NbSe₃ (Figure 1.6) and blue bronze K_{0.3}MoO₃ (Figure 1.13), two different CDW transitions are observed. The crystal structure in blue bronze K_{0.3}MoO₃ is more one-dimensional than NbSe₃; and therefore, blue bronze has a higher Peierl's transition temperature. Also, Peierl's transition in NbSe₃ is incomplete, and the material does not become fully gapped below transition temperature. However, in blue bronze K_{0.3}MoO₃, Peierl's transition opens up an energy gap in the entire Fermi surface, and change the compound from a metal to a semiconductor.

Beside NbSe₃ and K_{0.3}MoO₃, there are number of other materials that show CDW characteristics, and exhibit sliding CDW. Table 1.1, compares the structure and the electrical properties of different CDW materials [8].

	Symmetry	Space group	Chain axis	Room temp. conductivity ($\Omega^{-1} \text{ cm}^{-1}$)	Room temp. character	Low temp. character	CDW transition temp. (K)	CDW wavevector	Common surability	
NbSe ₃	monoclinic	p2 _{1/m}	b	$\sigma_1 = 4000$ $\sigma_1/\sigma_{\perp} = 10$	metallic	"metallic" resistive anomalies	$T_1 = 144$	(0, 0.243, 0)	4.12	
							$T_2 = 59$	(0.5, 0.259, 0.5)	3.86	
TaS ₃	Type I	orthorhombic	C222 ₁	c	$\sigma_1 = 2600$ $\sigma_1/\sigma_{\perp} = 100$	metallic	Peierls semiconductor	$T_P = 220$	(0.5, ± 0.125 , 0.25)	4.0(?)
	Type II	monoclinic	p2 _{1/m}	b	$\sigma_1 = 100$ $\sigma_1/\sigma_{\perp} = 200$	metallic	Peierls semiconductor	$T_1 = 240$	(0, 0.253, 0)	3.95
								$T_2 = 160$	(0.5, 0.245, 0.5)	4.08
	Type I	triclinic	p $\bar{1}$	b	$\sigma_1 = 10$	Peierls semiconductor	Peierls semiconductor	$T_P > 300$	(0, 0.5, 0)	2.0
NbS ₃	Type II		b		semiconductor	Peierls semiconductor	$T_P < 300$	(0.5, 0.297, 0) (0.5, 0.353, 0)	3.37 2.83	
	Type III			$\sigma_1 = 80$	semi-metallic	Peierls semiconductor	$T_P = 155$			
	(TaSe ₄) ₂ I	tetragonal		c	$\sigma_1 = 350$	semi-metallic	Peierls semiconductor	$T_P = 265$	(0.5, 0.5, ± 0.085)	11.76
(NbSe ₄) ₃ 3I	tetragonal	p4/mmc	c	$\sigma_1 = 67$	semi-metallic	Peierls semiconductor	$T_P = 285$			
K _{0.3} MoO ₃	monoclinic	c2/m	b	$\sigma_1 = 7000$ $\sigma_1/\sigma_{\perp} = 10$	metallic	Peierls semiconductor	$T_P = 180$	(0, 0.74, 0.5)	1.35	

Table 1.1: The structural and electrical properties of some of CDW materials [8].

1.1.5 Motivations

With recent advancements in understanding graphene's unique electronic properties, and its dramatic difference with the bulk form, a new area of research in experimental solid-state physics, generally known as "beyond graphene", has been started. In this area the finite-size effect, as well as fundamental changes in few-layer form of previously studied solids with layered structure are investigated. The layered structure of these materials allows for relatively easy exfoliation to create thin samples.

Electronic properties of materials with CDW phases have been shown to be a strong function of the overall crystal dimension. For example, Thorn and associates [52] have comprehensively studied the finite-size effect on NbSe₃ crystals as thin as 50nm.

However, two other dimensions of samples were kept larger than their corresponding phase correlation length L .

In studying finite-size effect on CDW materials, two distinct characteristic lengths are relevant: The phase-correlation length, L (also known as Larkin-Ovchinnikov or Fukuyama-Lee-Rice length), and the amplitude correlation length, ξ . The amplitude correlation length, ξ is proportional to the Fermi velocity and is inversely proportional to the energy gap [35]:

$$\xi \sim \frac{\hbar v_F}{\Delta}$$

In NbSe_3 ξ is 10-50 Å for both CDW phases [53].

X-ray diffraction measurements have shown that typical values for L in NbSe_3 are $10\mu\text{m}$ and $1\mu\text{m}$ for the along the chain, L_{\parallel} and, transverse, L_{\perp} correlation lengths, respectively. Samples with these dimensions are experimentally realizable. Finite size effects are observed in samples having at least one dimension below the characteristic length. Figure 1.14 shows a simple classification of dimensionality of the finite-size effects.

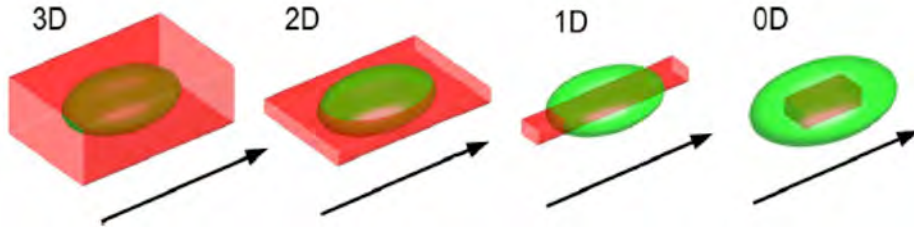


Figure 1.14: “Dimensionality of finite-size effects for the most usual cases. A phase-correlation volume is shown in green, a sample is red. Arrows denote the chain direction.” [54]

In previous studies [52], finite size effects on CDW have been analyzed in 2D systems, where a noticeable increase in E_T in thin samples was observed. However, no comprehensive studies on the finite-size effect on 1D and 0D CDW systems have been conducted. Since CDW dynamics are closely related to the underlying pinning potentials, and because the distribution and density of these pinning potentials dramatically change by reducing the dimension, a strong finite-size effect in 1D and 0D CDW systems is expected.

1.2 Thin NbSe₃ Crystals

1.2.1 Device Fabrication and Characterization

In order to get the highest possible quality of crystal, I decided to use a top-down approach, by exfoliating thin samples from high-quality large crystals of NbSe₃. I used NbSe₃ crystals previously made in the Zettl group. Next, samples were thinned down using an exfoliation technique. Then, final devices were prepared by an e-beam lithography method, on a silicon-silicon dioxide substrate with pre-patterned alignment marks.

1.2.1.1 Crystal growth

I used NbSe₃ crystals, previously grown by Michael Hundley [55], using a vapor-transport technique, in the Zettl group. In this method, “Nb and Se in stoichiometric quantities, together with a transport agent (I₂, ICl₃, or excess Se) and any dopant, are placed in one end of a fused quartz ampoule, which is then evacuated and sealed. The ampoule is placed in a gradient furnace, and slowly heated to 700°C in a reverse temperature gradient, i.e., with the starting material end coldest. The Nb and Se react to form a powder of NbSe₃, and any Nb on the walls of the ampoule transports to the source material end. A forward temperature gradient is then slowly established. NbSe₃ and related volatile species transport from the starting material end to the cold end, where NbSe₃ crystals nucleate at the ampoule walls and grow. Removal of Nb from the ampoule walls by the reverse gradient and slow establishment of the forward gradient minimizes the number of nucleation points and maximizes crystal size.

“Crystals thus grown, have the form of long flat ribbons, with typical lengths of several centimeters, widths of 10-100 μm, and thicknesses of 1-10 μm. The total transported crystal mass is usually only a few percent of the mass of the starting materials.” [55] Figure 1.15 is a SEM image of a typical NbSe₃ ribbon [56].

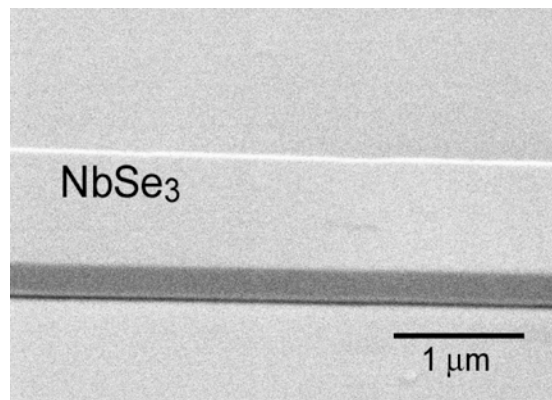


Figure 1.15: SEM image of a NbSe₃ crystal which was grown using the vapor-transport technique [56].

1.2.1.2 The exfoliation technique

My experience with exfoliating graphene helped me refine the exfoliation process in order to apply it to NbSe₃ crystals. Single crystalline NbSe₃ usually comes in thin, ribbon-shaped whiskers, and are several centimeters in length. Since the bonds between quasi-one-dimensional chains in NbSe₃ are very weak, this material can be exfoliated very easily. I started with a few long ribbons of NbSe₃ and placed them on a piece of scotch tape. After folding the tape onto itself several times, it was covered with thin NbSe₃ ribbons, which formed a grey film on the tape. I transferred a small amount of this film by exfoliating with a new tape. I repeated this process until the NbSe₃ film on the tape became semi-transparent. Next, I applied the final tape, containing thin NbSe₃ ribbons onto the target substrate. After applying pressure with my thumb, and leaving it for 15 minutes, I slowly removed the tape, and examined the exfoliated crystals under the optical and electron microscope. Figure 1.15 shows a thin NbSe₃ crystal, exfoliated on a Si-SiO₂ substrate with pre-patterned gold alignment marks.

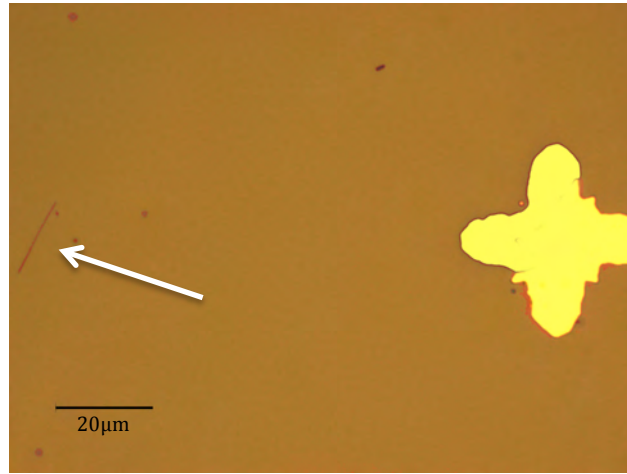


Figure 1.15: The SEM micrograph of NbSe₃ crystals on a Si-SiO₂ substate with pre-patterned gold alignment marks

1.2.1.3 E-beam lithography and nitrogen plasma treatment

For this experiment, I used silicon wafers with a 285 Å silicon dioxide layer on top, as the substrate. Before transferring the crystals to the substrate, I patterned a network of gold alignment marks, using conventional photolithography and lift-off techniques. I designed a photolithography mask, containing a network of 2×2 μm crosses separated by 200 μm. The UV exposure step was completed in Marvell Nanolab Facilities, using the ksaligner photolithography machine. The metal evaporation and lift-off steps were carried out in the Zettl lab.

After transferring the exfoliated crystals to the substrate, I located the thinnest crystals by using a combination of optical microscopy, Scanning Electron Microscopy (SEM), and Atomic Force Microscopy (AFM) techniques. Next, using SEM, I mapped the selected crystals to find their relative position with the alignment marks network. After that, I fabricated the electrical contacts, using e-beam lithography and lift-off procedures.

First, I experimented with the standard e-beam resist, a bilayer of MMA-PMMA. After exposing the resist with an electron beam, and subsequently developing it in a MIBK-IPA solution, I deposited a thin film of indium-chromium-gold tri-layer using e-beam evaporation technique. Indium has been proven to form a great electrical contact with a large variety of crystals including the blue bronze [57]. The final contact patterns were formed with a lift-off step in acetone.

I selected the indium-chromium-gold tri-layer, because it created the most uniform metal film on NbSe₃ crystals. If deposited on NbSe₃ crystals alone, indium does not form a uniform film, but forms isolated balls. I also tried depositing indium at liquid nitrogen temperature, using a thermal evaporation machine equipped with a sample cooling system. This also did not improve the quality of the indium film.

However, even with the tri-layer metal film, the contact resistances of the final devices were too high. In order to solve the high contact resistance problem, right before placing the samples in the e-beam evaporation chamber, I performed a plasma treatment step. However, since PMMA has a very weak physical structure when placed in a reactive plasma environment, it gets etched and re-deposited, and hence, does not hold its pattern. Therefore, I changed the e-beam resist to ZEP, which has better resistance in etching environments than PMMA. Section 2.2.4 provides an overview of different e-beam resists and advantages of each. Table 1.2 compares the properties of PMMA and ZEP e-beam resists [58].

The e-beam lithography step with the ZEP resist is as follows: A spin coating technique was used to coat a bi-layer of MMA EL6 and ZEP-520A, at 4000 rpm and 3000 rpm respectively, on substrates with previously mapped NbSe₃ crystals. Next, samples were baked at 180°C in air on a hot plate. For large patterns (i.e. contact pads), the e-beam lithography step was carried out in a NPGS system in the Zettl lab. For small features, I used the Crestec machine in the Nanolab, as described in section 2.2.4. The nitrogen plasma treatment step was performed in a 50 sccm flow of nitrogen, at 50 W power and for 30 seconds. In this condition, the plasma treatment step had a minor effect on the ZEP e-beam resist film. For this step, I used a Reactive Ion Etching (RIE) machine in the Zettl lab.

Sensitivity to e-beam	ZEP is ~5x more sensitive
Resolution	Almost equivalent
Edge roughness	ZEP has a greater line edge roughness (LER)
Durability	Etch selectivity of Si/ZEP is ~3x higher

Table 1.2: Comparison between ZEP and PMMA e-beam resists [58].

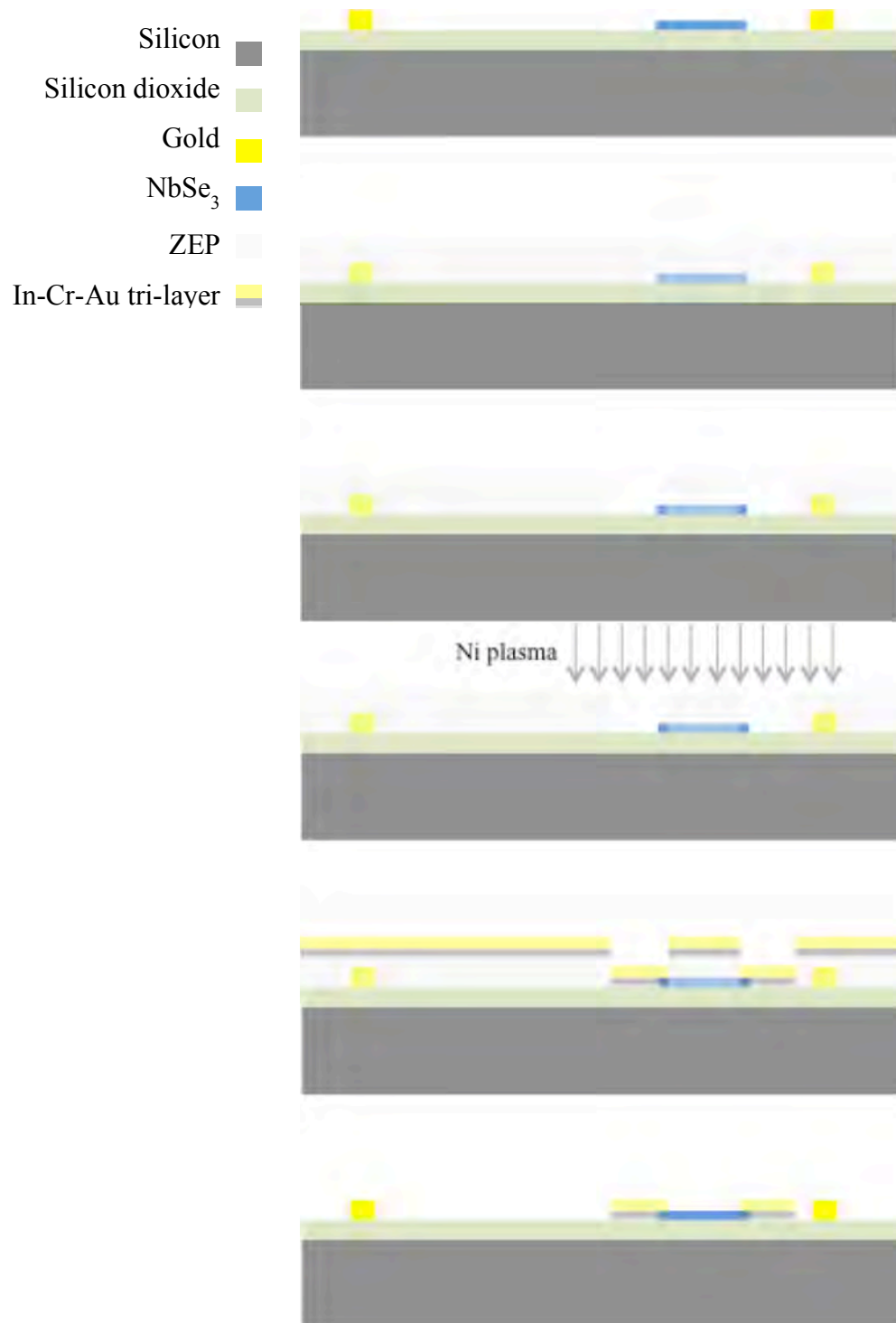


Figure 1.16: Schematic of the fabrication process for NbSe₃ devices. The process steps were as follows: 1-Crystal exfoliation on a Si-SiO₂ substrate with alignment marks. 2- Deposition of ZEP e-beam resist. 3-E-beam lithography to pattern metal contacts. 4- Nitrogen plasma treatment to enhance the ohmic contacts. 5-Deposition of indium-chromium-gold tri-layer as the metal contact. 6-Lift-off.

After the RIE step, I immediately transferred the samples to an e-beam evaporation chamber where I deposited metal contact layers. The final thicknesses of indium, chromium, and gold films were 15nm, 5nm and 30nm, respectively. The deposition rate was maintained at 1 Å/s, for all metal films. For metal deposition, I used the e-beam evaporation machine in Zettl lab. Figure 1.16 shows a schematic of the entire fabrication process.

1.2.1.4 Electrical measurement methods

Gas-flow cryostat

Most of low-temperature electrical measurements were performed in a continuous gas-flow cryostat system, which was built in Zettl group. The system was composed of a helium dewar, a double walled stainless steel tube, and a cylindrical sample chamber with an opening port to place the sample for measurement. A schematic of the system is shown in Figure 1.17 (a). By controlling the current that passed through a resistive heater inside the dewar, the flow of the cold helium gas was controlled.

Figure 1.17 (b) shows a schematic of the sample chamber. Cold helium gas exited through the two valves, located in the opposite end of the port. These valves could further regulate the flow of helium, and hence, the temperature inside the chamber.

The sample holder consisted of a copper cup with a coil heater and a diode. I placed a secondary diode close to the sample, and provided multiple pairs of wires to bias and measure the sample, bias the heater coil, and read the diodes voltages. I also provided a stainless steel SMA coaxial cable for noise and high-frequency measurements. A schematic of the copper cup is shown in Figure 1.17 (c).

The copper cup heater coil and the attached diode were connected to a PID temperature controller. The gas-flow cryostat system was able cool down the sample to 10K in less than 30 minutes, and control the sample temperature with 0.01K accuracy.

DC-resistance versus temperature

Figure 1.18 shows a schematic of the measurement setup for low-field dc-resistance vs. temperature. A NI Labview program was written to synchronize, measure and store the data from different instruments. A DT-670 silicon diode was used for a precise temperature measurement. A thermally conductive stycast was used to attach the diode and sample to a copper mounting post, and put them in thermal contact. Figure 1.19 shows the calibration plot for DT-670 diode. This diode had a very high precision in 0-20K range and a high precision above 20K.

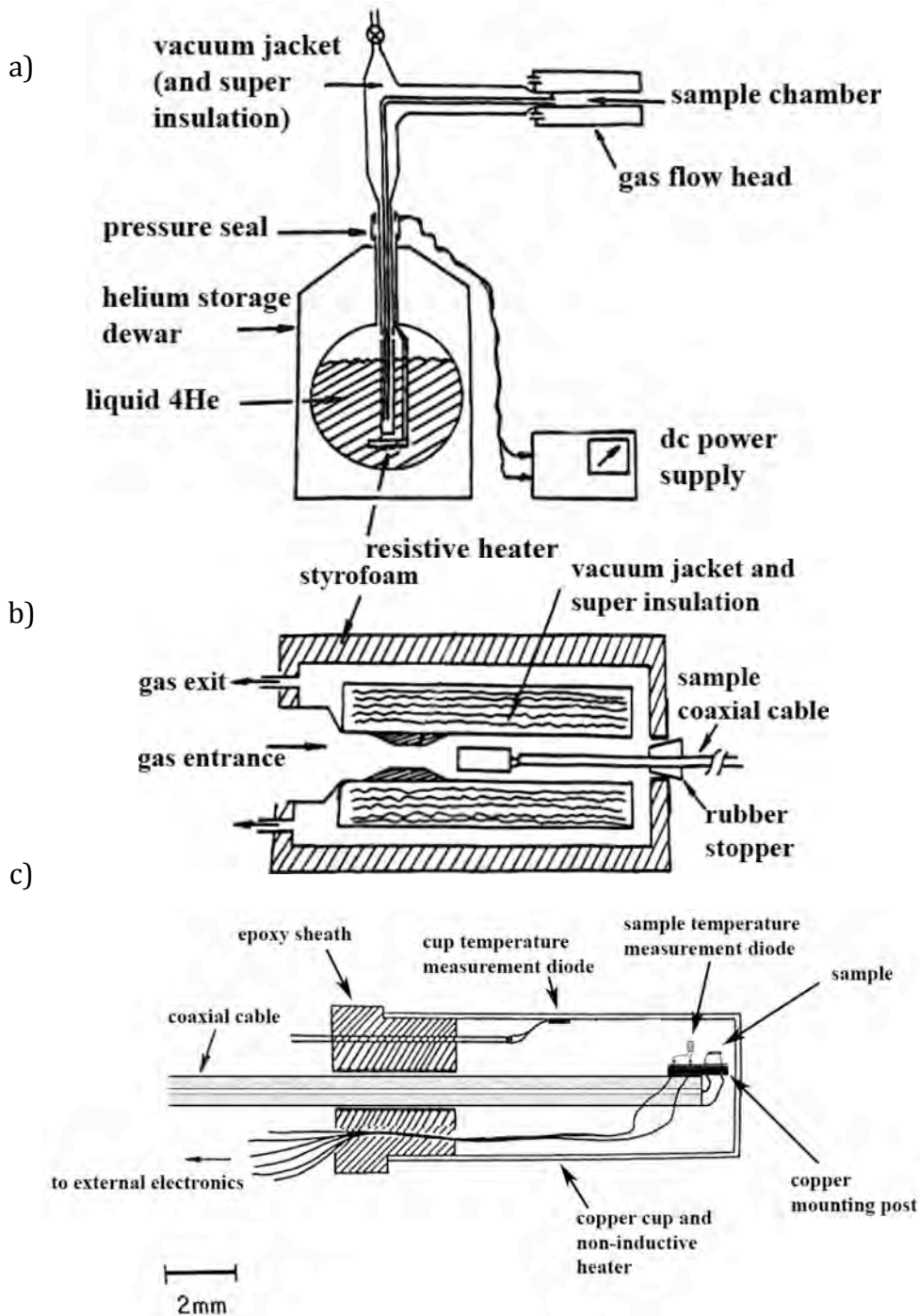


Figure 1.17: (a) The gas-flow cryostat, (b) the sample chamber, and (c) the copper cup. Cold helium gas passed through the double-walled vacuum tube and exited from the two valves in the sample chamber. A PID temperature controller, connected to the copper cup, controlled the temperature of the sample inside the cup. From [59] with changes.

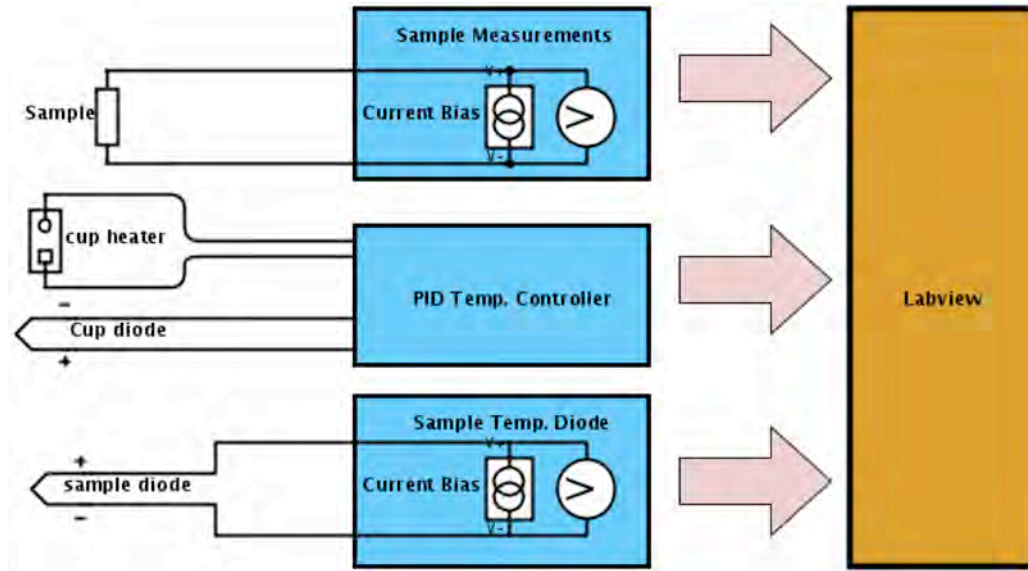


Figure 1.18: A schematic of the setup used to measure the dc-resistance versus temperature. Sample was biased and measured with a Keithley 2602A system, the copper cup temperature was controlled with a PID temperature controller, and a DT-670 silicon diode measured the sample temperature. A Labview program synchronized, stored, and controlled different modules.

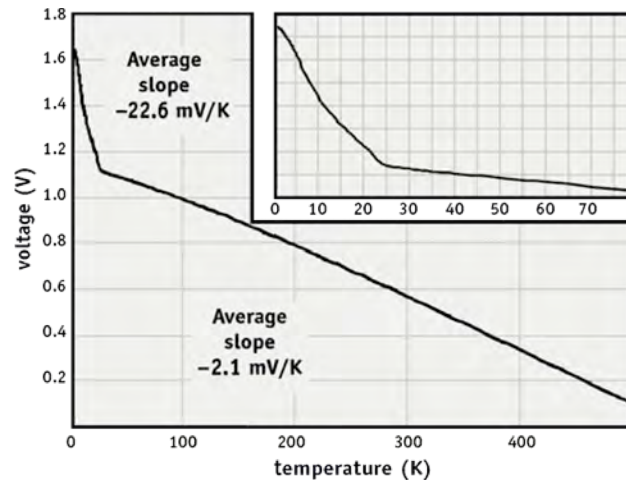


Figure 1.19: Voltage versus temperature characteristics for a DT-670 temperature measurement silicon diode [60], when biased with $10\mu\text{A}$ dc current.

In order to precisely measure the dc-resistance, the effect of temperature on the conductivity had to be taken into account. In order to address the thermal effect multiple methods were employed, and the results were compared to ensure the accuracy of the measurement. These methods are as follows:

1. The sample was biased with a dc-current in positive and negative polarities. The positive (V_p) and negative (V_n) voltages were measured, and the average

of the two $(V_p - V_n)/2$ was recorded as the output. Thus, any voltage shift caused by thermal effects was neutralized.

2. The sample was biased using a continuous low-duty cycle pulse signal with a microsecond pulse width and 1Hz frequency. The long period between pulses allows the sample to cool down.
3. Using a lock-in amplifier, the sample was biased with a low-power ($P=0.01$ nW) and low-frequency (500Hz) ac-signal. The lock-in allowed me to lower the power, and thus, minimize the heating effect.

Threshold field detection

Figure 1.20 (a) shows the measurement setup that was used to detect the threshold field. This measurement technique is based on the fact that, above the threshold field, a crystal with a charge density wave becomes a non-linear conductor where the charge densities carry the excess current. Figure 1.21 shows a typical NbSe_3 I-V curve at 36K. The deviation from the linear conductivity starts at the threshold field.

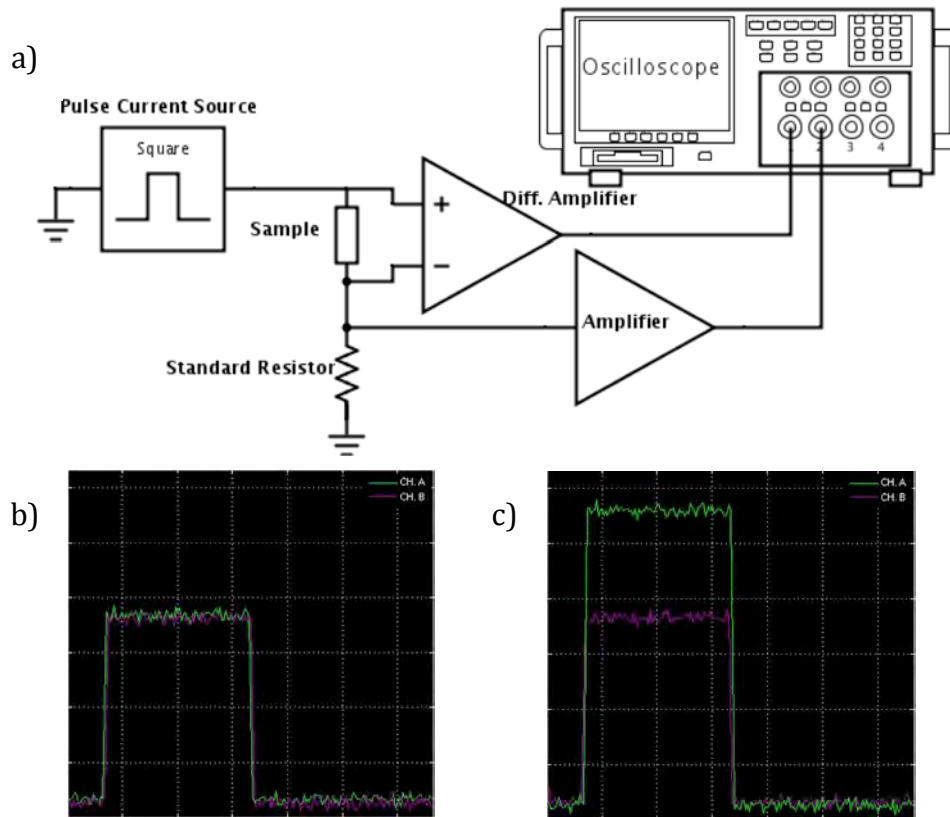


Figure 1.20: (a) The setup used to measure the threshold field. (b) The output signals from the two amplifiers follow each other closely, while the sample is in the linear regime. (c) As soon as the sample becomes non-linear (above the threshold field), the two pulses separate on the oscilloscope display.

In the measurement setup shown in Figure 1.20 (a), amplifier gains can be fine-tuned such that, in a low-field regime, the output signal from the sample and the standard resistor (which is chosen to be close to the low-field resistance of the sample) on the oscilloscope precisely follow each other. While the sample is in the linear regime, increasing the current source power will increase, both V_{sample} and V_{resistor} , at the same rate, and therefore their respective pulse shapes on the oscilloscope will follow each other. However, above the threshold field, the increasing current source power will cause a faster increase in V_{resistor} versus V_{sample} . This is because, above the threshold field, sliding CDW carriers will decrease the total resistance of the crystal and hence the lower voltage. Therefore, the threshold field can be measured by measuring the bias current at

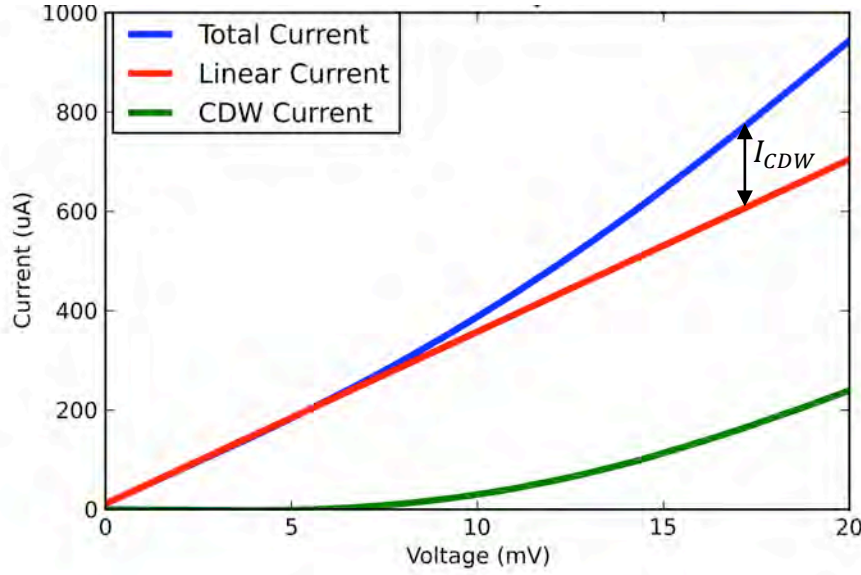


Figure 1.21: Current versus voltage characteristic of a bulk NbSe_3 crystal at 36°K . The crystal becomes non-linear above the threshold field, where the CDW carriers slide and carry the excess current.

which the two signals on the oscilloscope display start to separate. In order to minimize the heating effect, a microsecond current pulse, with a low duty-cycle, was employed as the bias source.

Noise measurement circuit

Charge density wave states have been shown to have interesting Narrow Band Noise (NBN) characteristics. A spectrum analyzer was used to detect the NBN signal from the sample. However, since the input impedance of most spectrum analyzers are 50Ω , the direct measurement of the low-power NBN signal was not possible, and a low-noise amplifier was required.

In order to fix the above problem, I built a low noise, large bandwidth amplifier circuit, similar to the circuit used in a previous study on bulk crystals with charge density waves [59]. The overall structure of the circuit was kept intact. However, the input impedance and the gain of the circuit were increased to support the higher impedance and the weaker signal of the thin film crystals.

A schematic of the low-noise measurement circuit is shown in Figure 1.22. The overall size and the relative position of different components were important to achieve the desired bandwidth. At the heart of the circuit a UA733 low-noise video differential amplifier was used. Figure 1.23 (a) shows the gain vs. frequency for a UA733 IC. After amplification, the next module is a follower circuit, which utilizes a NTE108 NPN RF transistor and provides sufficient power for the spectrum analyzer. The output impedance of the circuit was designed to be close to 50Ω to match the input impedance of the spectrum analyzer. The circuit was tested to amplify signals up to 50MHz.

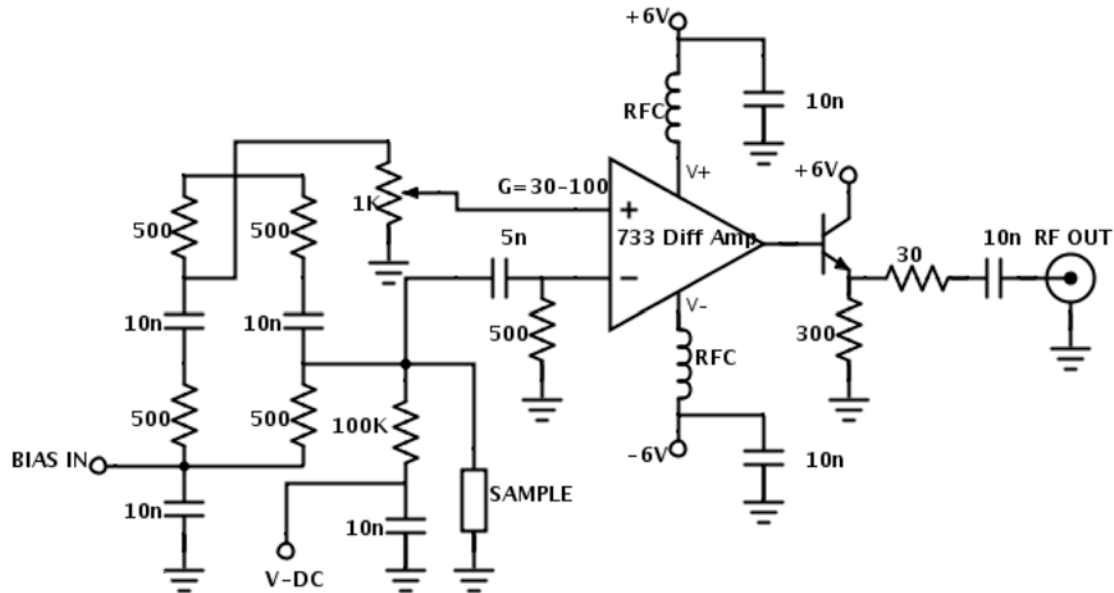


Figure 1.22: Noise measurement circuit. First, UA733 amplifies the signal. Next, a follower circuit provides the required power for the spectrum analyzer. The circuit was built similar to [59] with some modifications.

In order to measure the NBN signal, the sample was biased with a dc electric current

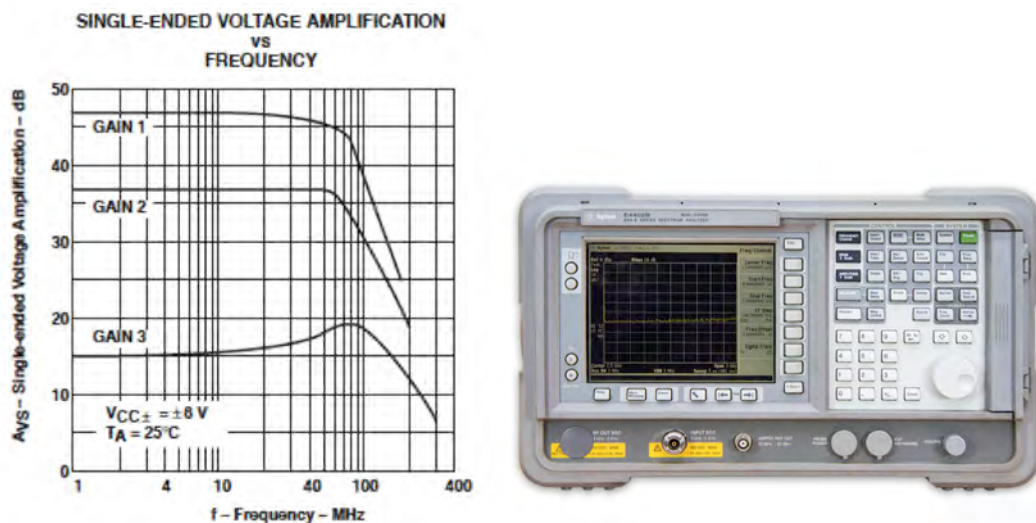


Figure 1.23: (a) UA733 gain versus frequency characteristics [61] and (b) an Agilent E4402B spectrum analyzer [62]

using a Keithley 2602A system. A SMA coaxial cable transferred the noise signal to the noise measurement circuit. An Agilent E4402B spectrum analyzer (Figure 1.23 (b)) detected the amplified NBN signal. A Labview program was written to read and store the bias data from the Keithley, signal data from the spectrum analyzer, and temperature from the sample diode. The NBN detection setup is shown in Figure 1.24.

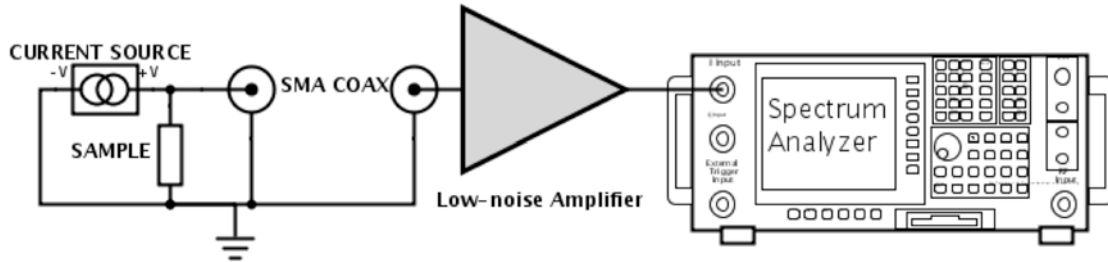


Figure 1.24: Narrow-band noise measurement setup. The noise signal from the dc-biased sample was transferred to the noise measurement circuit. After amplification, the signal was detected in a spectrum analyzer.

1.2.2 Results and Discussion

1.2.2.1 Exfoliation

The exfoliation technique, described in section 1.2.1, was very effective, and I was able to achieve NbSe_3 crystals as small as 18nm in thickness. Figure 1.25 shows an optical image of a typical exfoliated NbSe_3 sample before (a) after (b) the removal of tape residue. The typical lateral dimension of the exfoliated crystals was 1-10 μm . The thickness of the resulting crystals was mostly in 30-60nm range, and NbSe_3 crystals as thin as 18nm was achieved with this method.

NbSe_3 crystal structure is composed of quasi-one-dimensional wires. Therefore, after exfoliation, high aspect ratio NbSe_3 crystals were expected. In my experiments, the typical aspect ratio of exfoliated NbSe_3 crystals were 1:10 to 1:20.

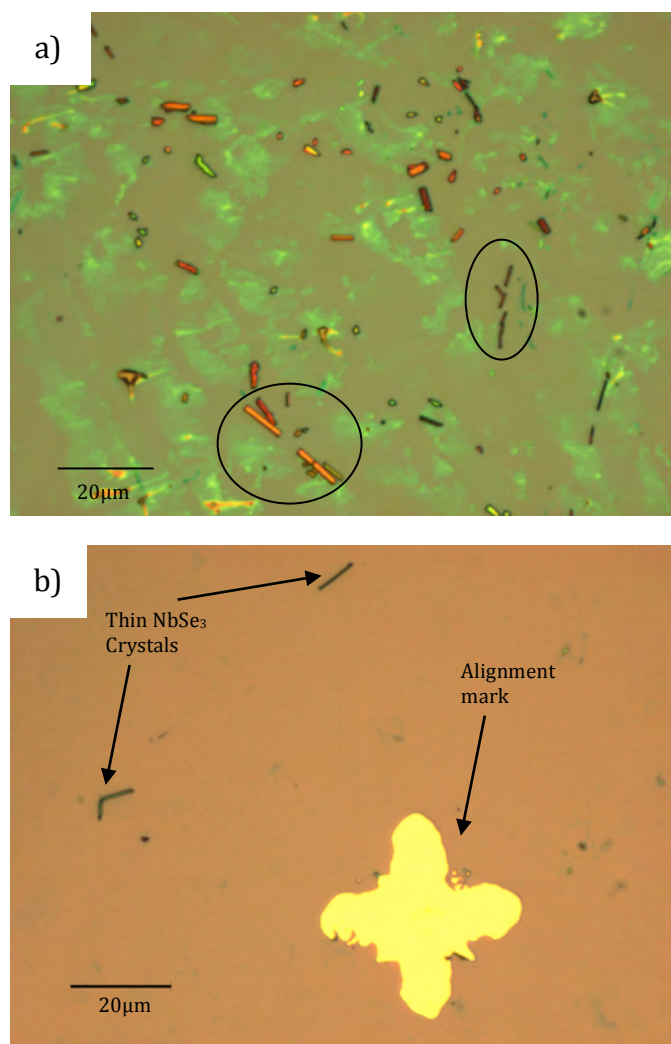


Figure 1.25: Optical image of exfoliated NbSe_3 crystals on Si-SiO_2 substarate before (a) and after (b) the removal of tape residue. Some exfoliated crystals are encircled in (a) and mapped crystals, as well as an alignment mark are denoted by arrows in (b).

Wafer dicing tape from the Nanolab facilities was used for exfoliation.

1.2.2.2 Indium deposition

Indium has a lower work function (4.09 eV) than gold (5.1-5.47 eV) or chromium (4.5 eV) [63]. The lower work function (and thus higher Fermi energy) makes indium a good candidate for electrical contacts to blue bronze and NbSe₃ crystals [57]. However, it is difficult to deposit a conformal layer of indium, because it does not wet the surface of blue bronze, NbSe₃ or silicon dioxide, and instead, forms isolated balls of indium. An 80 nm thin film of indium, deposited on a silicon dioxide substrate, is shown in Figure 1.26. Similar results were observed when depositing indium on blue bronze or NbSe₃ crystals.



Figure 1.26: An 80nm film of indium on Si-SiO₂ substrate. The deposition was carried out at the room temperature, and the rate was 3 Å/s.

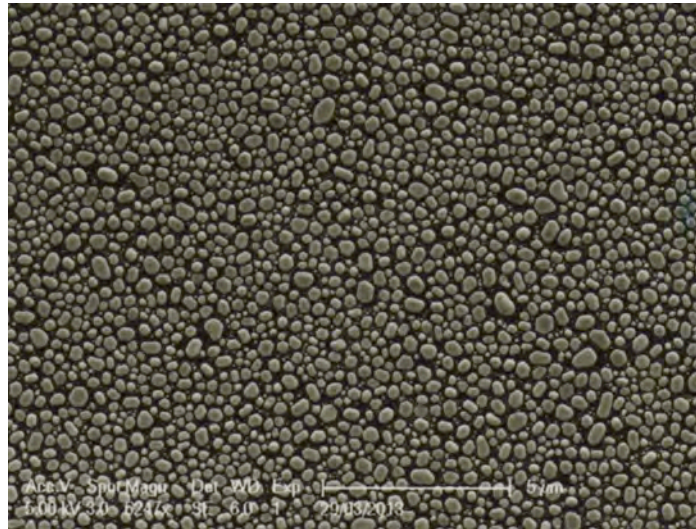


Figure 1.27: Indium film deposited on Si-SiO₂ substrate. The substrate temperature was kept at 70K and the deposition rate was maintained at 1 Å/s.

I also studied the effect of the deposition rate by examining the indium films deposited with different deposition rates (3 Å/s, 1 Å/s, 0.7 Å/s and 0.5 Å/s). However, I observed no major differences in the deposited indium film. Furthermore, I experimented with low-temperature deposition. The goal was to decrease the kinetic energy of deposited atoms

on the surface. In this study, the substrate was held at liquid nitrogen temperature during the deposition. Several deposition rates at this temperature were also experimented. Figure 1.27 shows an indium film deposited at 70K at 1 Å/s rate. The low-temperature deposition also did not improve the quality of the indium film.

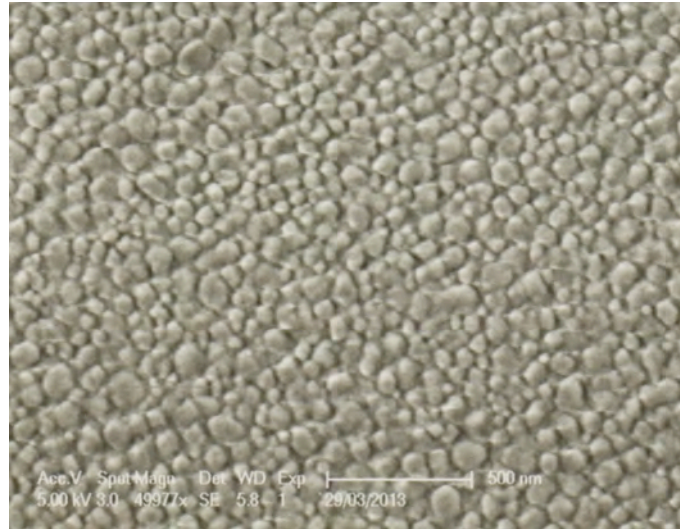


Figure 1.28: SEM micrograph of indium-chromium-gold (15nm, 3nm, and 40nm respectively) tri-layer on NbSe₃. The deposition was performed at the room temperature and the rate was maintained at 1 Å/s for all layers.

The most uniform film was obtained in a tri-layer of indium-chromium-gold. The thicknesses of the layers were 15nm, 3nm and 40nm for indium, chromium, and gold, respectively. The inner Indium layer ensured good electrical contact with the crystal. I chose chromium as the second layer in order to enhance the adhesion of the film to the substrate. And an outer gold layer was selected to prevent oxidation and improve the wire-bonding step. A SEM micrograph of an In-Cr-Au tri-layer, deposited on a NbSe₃ crystal, is shown in Figure 1.28.

1.2.2.3 Contact resistance and plasma treatment

As was expected, the condition of the crystal was important in order to achieve low contact resistance. The ideal metal contact can only be made on a freshly cleaved surface of a crystal [57]. Therefore, in previous studies, large crystals were cleaved and contacted with silver paste inside a ventilated glove box. However, since the crystals were small in this study, lithography procedures were required. Therefore, I employed an alternative process to clean the surface. In this process, the samples were treated with a short nitrogen plasma step, right before the deposition of metal contacts. The nitrogen plasma removed any hydrocarbon residue on the surface, slightly doped the surface, and created surface roughness to lower the contact resistance. The SEM micrograph of a device fabricated with this method is shown in Figure 1.29. In this method, the contact resistance was 10-15% of the total resistance.

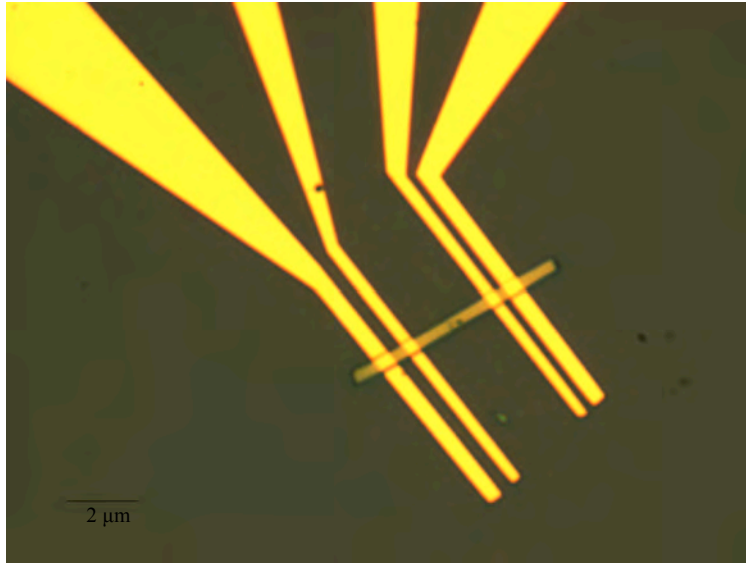


Figure 1.29: SEM image of a four probe NbSe₃ device. An indium-chromium-gold tri-layer was used as the metal contact. A plasma treatment step enhanced the ohmic contact.

1.2.2.4 Device fabrication

Figure 1.30 shows two NbSe₃ devices on a Si-SiO₂ substrate. First, NbSe₃ crystals were exfoliated on a silicon dioxide substrate, with pre-fabricated alignment marks. Next, large metal pads were patterned using an NPGS-SEM machine in the Zettl lab. Finally, using a Crestec e-beam lithography machine in the Marvell Nanolab, NbSe₃ crystals were connected to the large metal pads. Two and four probe devices were fabricated in order to study the contact resistance effect.

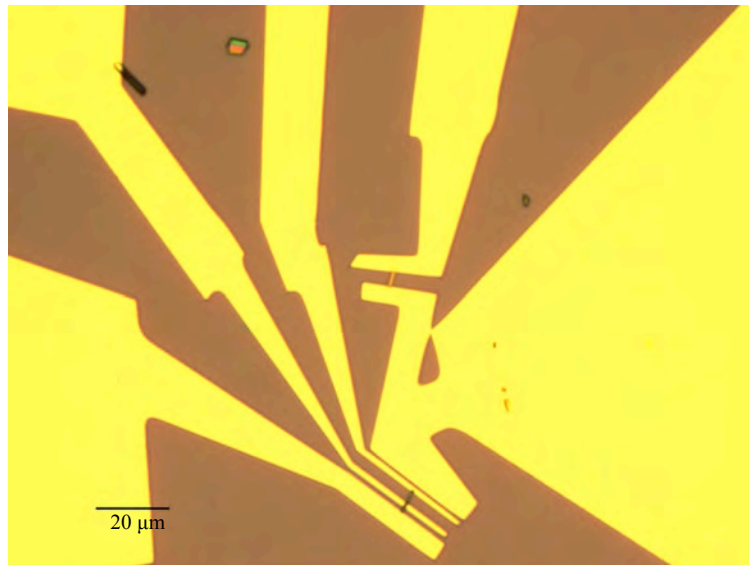


Figure 1.30: The final structure of two and four probe NbSe₃ devices, fabricated on Si-SiO₂ substrate.

1.2.2.5 Bulk crystal electrical measurements

a) dc-resistance study

Resistance of a bulk sample versus temperature was measured in 10-220°K range. Figure 1.31 shows the normalized dc resistance versus temperature for a bulk NbSe₃ crystal. In order to find the transition temperature, T_c , $1/R_0 (dR/dT)$ was calculated and its plot is shown in Figure 1.32. From this graph, the transition temperature for the first charge density wave state T_{c1} was 144 °K, and for the second charge density wave state T_{c2} was 59°K. These numbers were in good agreement with previous reports, [15, 32-34] which indicated a strong thermal coupling between the temperature measurement diode and the sample.

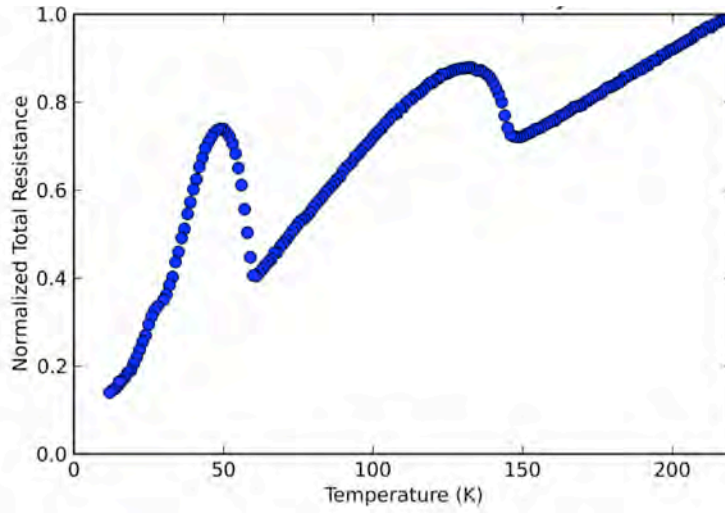


Figure 1.31: dc-resistance versus temperature for a bulk NbSe₃ crystal.

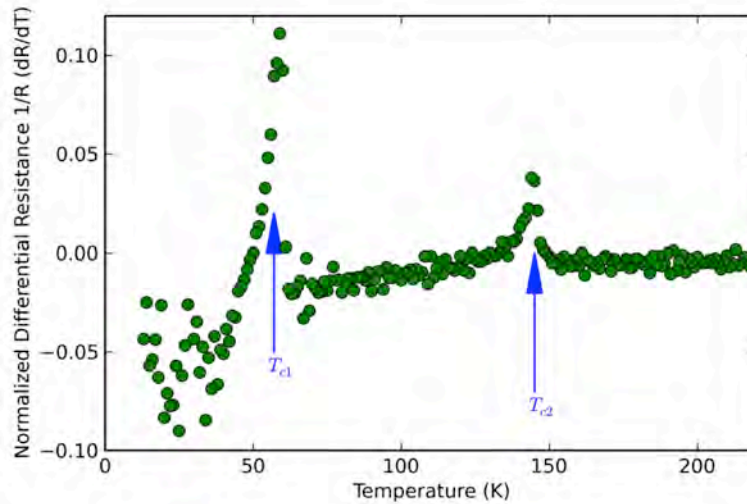


Figure 1.32: First derivative of dc-resistance versus temperature. Transition temperatures can be measured from this plot $T_{c1} = 144^\circ K$ and $T_{c2} = 59^\circ K$

b) Threshold Field Study

I measured the threshold field in a bulk NbSe₃ sample using the technique discussed in section 1.2.1.4. Figure 1.33 shows the threshold field for the first and the second charge density wave states in NbSe₃ bulk crystals. These results are in good agreement with previous studies [52]. In addition, differential resistance was measured using a lock-in amplifier at low frequencies.

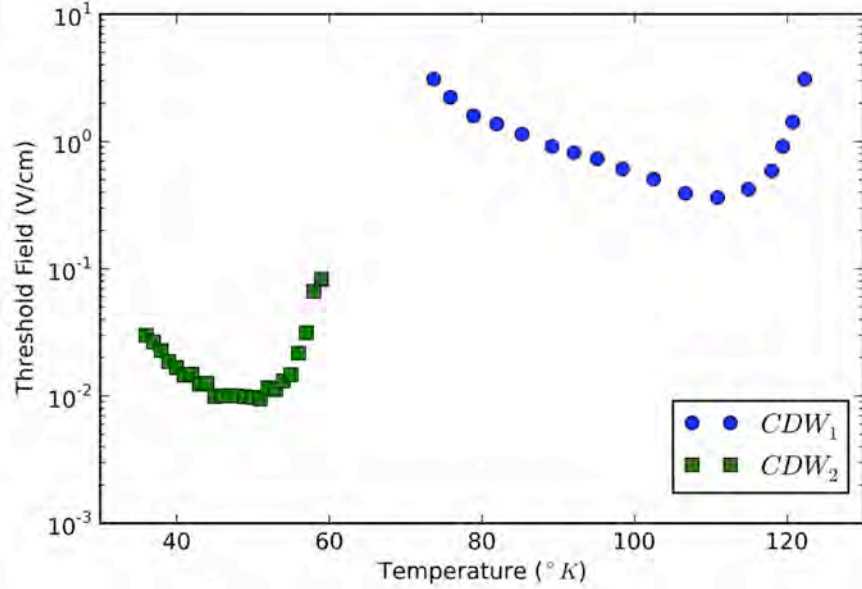


Figure 1.33- Threshold field of the first and the second CDW state versus temperature for a bulk NbSe₃ crystal.

c) Narrow-Band Noise Study

Figure 1.34 shows the output signal from the noise detection circuit for a bulk NbSe₃ sample under a dc-bias at 49°K. The charge density wave current can be calculated by subtracting the expected linear current from the total current, when the sample is in the non-linear regime (Figure 1.21).

As discussed in section 1.1.3, NBN peak frequency and charge density wave current have a linear relation. Furthermore, the slope of their linear relation has shown to be directly proportional to the density of charge density carriers [64]. Particularly:

$$I_{CDW} = neAf\bar{\lambda}$$

where n is the CDW carrier density, A is the cross section of the sample and λ is the charge density wavelength which can be measured from x-ray diffraction data.

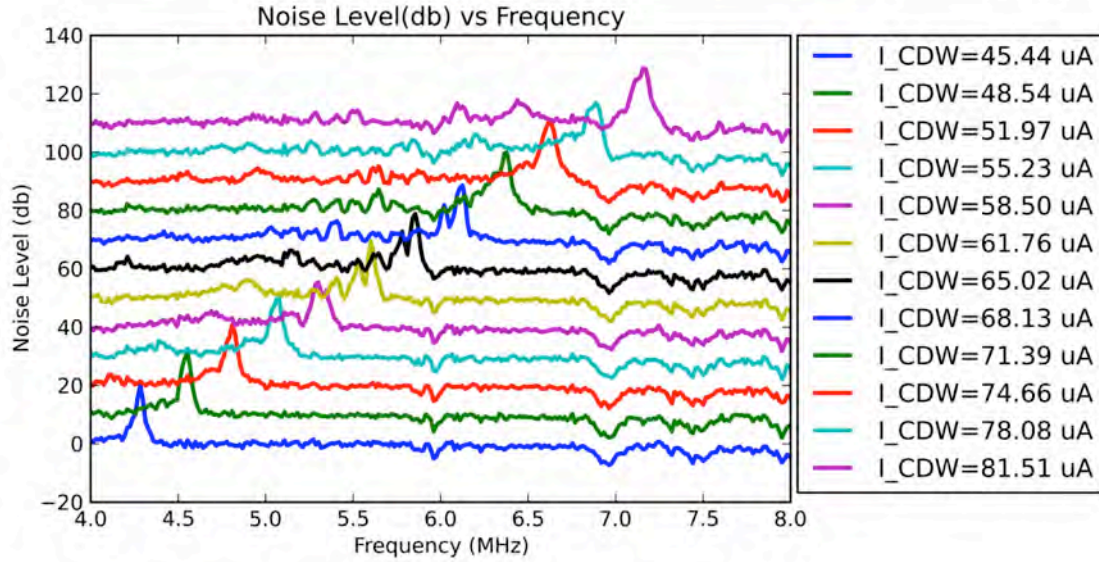


Figure 1.34- Narrow-Band noise characteristics of a NbSe₃ crystal. The signal was amplified with a low-noise amplifier circuit before being measured with a spectrum analyzer.

Figure 1.35 displays the peak frequency in NBN measurement versus the corresponding charge density wave current in a bulk NbSe₃ crystal. From the slope of the fitted line in this figure, n can be calculated to be $55.63 \times 10^{20} \text{ C/cm}^3$. Since the NBN measurements were performed at 49°K, the density of charge density carriers at 0°K can be estimated from the mean-field theory approximation shown in Figure 1.36.

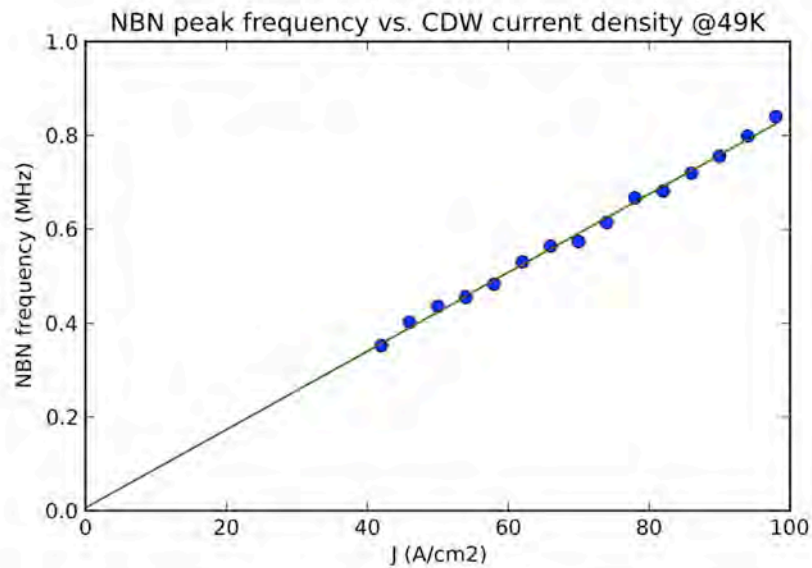


Figure 1.35 – Narrow-band noise peak frequency versus the CDW current density for a bulk NbSe₃ crystal. Green line is a fitted $f = cJ$ line.

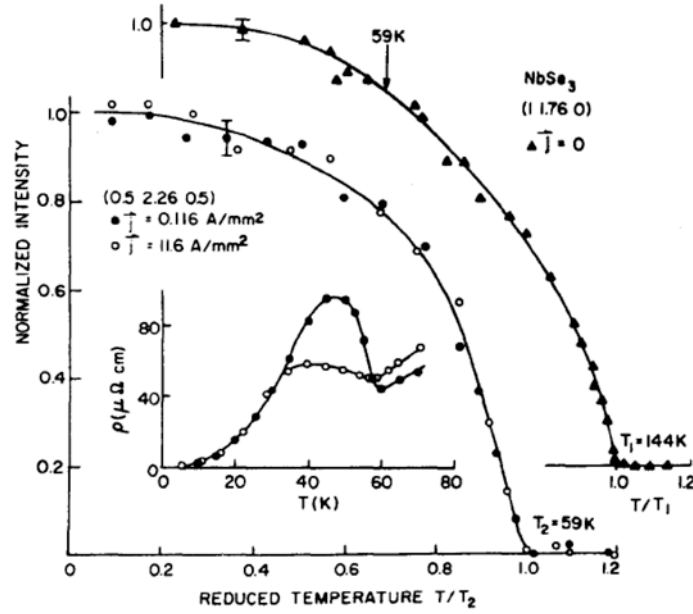


Figure 1.36: Normalized intensity of the x-ray peak versus temperature for both CDW states in NbSe₃. The solid line is the mean-field approximation. X-ray amplitude is directly proportional to the CDW order parameter Δ [65].

From Figure 1.36, it can be assessed that at 49K, ~60% of the carriers are excited. Therefore, the total density of charge density carriers can be approximated to be $88.12 \times 10^{20} \text{ C/cm}^3$. This value is in a good agreement with previous studies [8].

1.2.2.6 Thin NbSe₃ crystal measurements

The data presented in this section were measured from thin NbSe₃ crystals, exfoliated from the bulk crystal using the scotch-tape method described in section 1.2.2. Table 1.3 summarizes the dimension and room temperature resistance of the samples. From the room temperature conductivity σ [8], and the dimension of NbSe₃ crystals, the contact resistance can be estimated. The contact resistance in these samples was 15-20% of the total resistance. This amount was small enough to be ignored for this study, and therefore, two-probe measurements were performed.

I used the Atomic Force Microscopy technique to measure the thickness of the crystals, and the width and length were measured from Scanning Electron Microscopy image.

Sample No.	Thickness (nm)	Width (nm)	Length (μm)	Resistance at RT (k Ω)	Contact Resistance (%)
#1	55	550	7.4	0.76	19.5
#2	34	450	4.6	0.92	18.3
#3	31	280	3.2	1.08	14.6
#4	18	150	1.1	1.2	15.1

Table 1.3 – Thin NbSe₃ crystals dimension, room temperature resistance, and contact resistance calculated from room temperature conductivity $4 \times 10^3 \Omega^{-1} \text{cm}^{-1}$.

a) DC-Resistance versus Temperature

I measured the dc-resistance of thin NbSe₃ samples in the same way as described in section 1.2.1.4. Samples were biased with a dc-current well below the threshold field. A Keithley 181 Digital Nanovoltmeter was used to measure the corresponding voltage, while a PID temperature controller ramped up the temperature from 10K to 220K. Figure 1.37 shows the low-field dc-resistance versus temperature for 55nm, 34nm, 31nm, and 18nm thick, along with a bulk NbSe₃ samples. All curves are normalized to the resistance at 220K.

Figure 1.37 shows that in thin film NbSe₃ samples, the general behavior of the crystal, namely the overall metallic behavior of the crystal, remains intact. However, while thin film resistance closely follows the bulk crystal behavior in the first charge density wave region and above ($T > 59\text{K}$), a significant divergence from the bulk behavior is observed in the second charge density wave region ($T < 59\text{K}$). This divergence increases as the crystal becomes thinner.

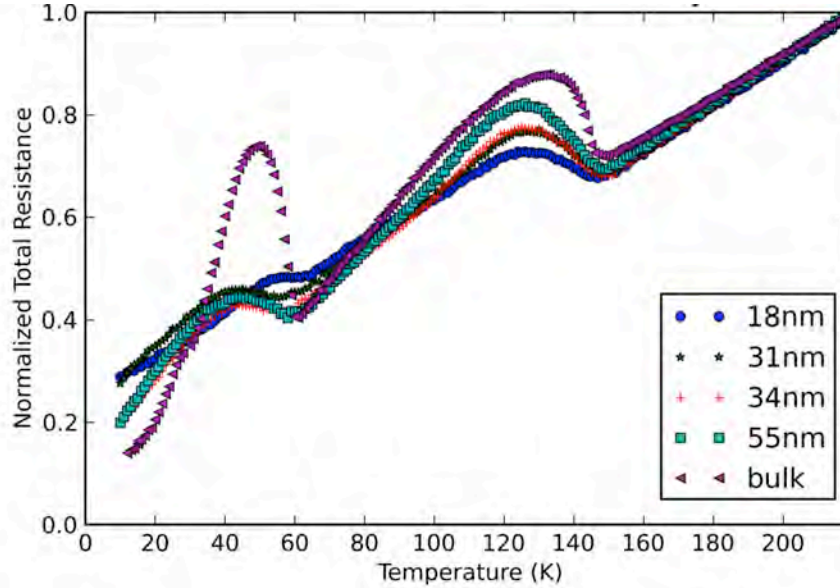


Figure 1.37: Normalized total resistance versus temperature for thin NbSe₃ crystals, compared with that of bulk crystal. As the crystal becomes thinner, the overall metallic behavior remains the same. However, the second CDW state deviates from that of the bulk.

In order to study the transition temperature, the first derivative of R versus temperature for thin NbSe₃ crystals are shown in Figure 1.38. Table 1.4 summarizes the two transition temperatures for different samples. From this table, no significant change in the first (T_{c1}), and second (T_{c2}) charge density wave transition temperatures were observed.

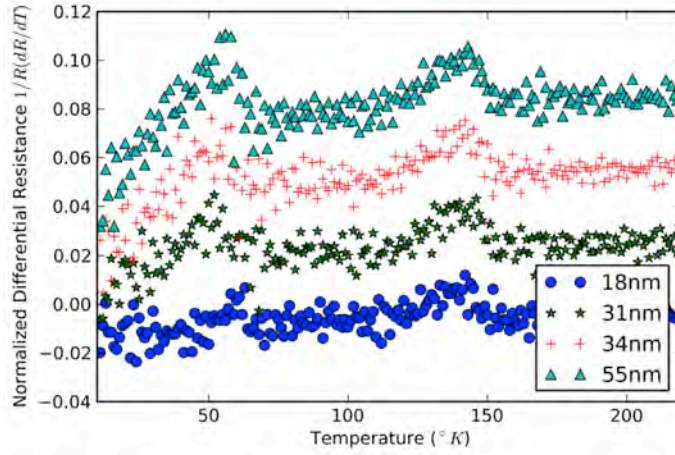


Figure 1.38: Differential resistance versus temperature for thin NbSe₃ crystals. The first and the second CDW transition temperatures can be measured from this plot.

Sample Thickness	Bulk	55nm	34nm	31nm	18nm
T _{c1} (K)	144	143	142	145	142
T _{c2} (K)	58	55	52	52	63

Table 1.4: Transition temperatures for the first and the second CDW in thin NbSe₃ crystals.

b) Threshold field measurements

Threshold field versus temperature for the first and the second charge density wave states are shown in Figure 1.39. No threshold field could be measured for the 18nm and 31nm samples in the second charge density wave region.

Figure 1.40 (a) shows the differential resistance versus applied electric field for 18nm sample at 49K and 110K. At 110K, a sharp drop at 2×10^4 V/cm suggests an active and sliding charge density wave state. However, at 49°K, no drop in the differential resistance was observed. The lack of drop in differential resistance can be attributed to the lack of CDW carriers.

Differential resistance versus applied electric field was also measured for the 55nm thick NbSe₃ crystal at 49K and 110K. The result is shown in Figure 1.40 (b). Finite threshold fields of 28 V/cm and 196 V/cm were observed at 49K and 110K, respectively. The finite threshold field suggests the existence of CDW carriers in the 55nm sample.

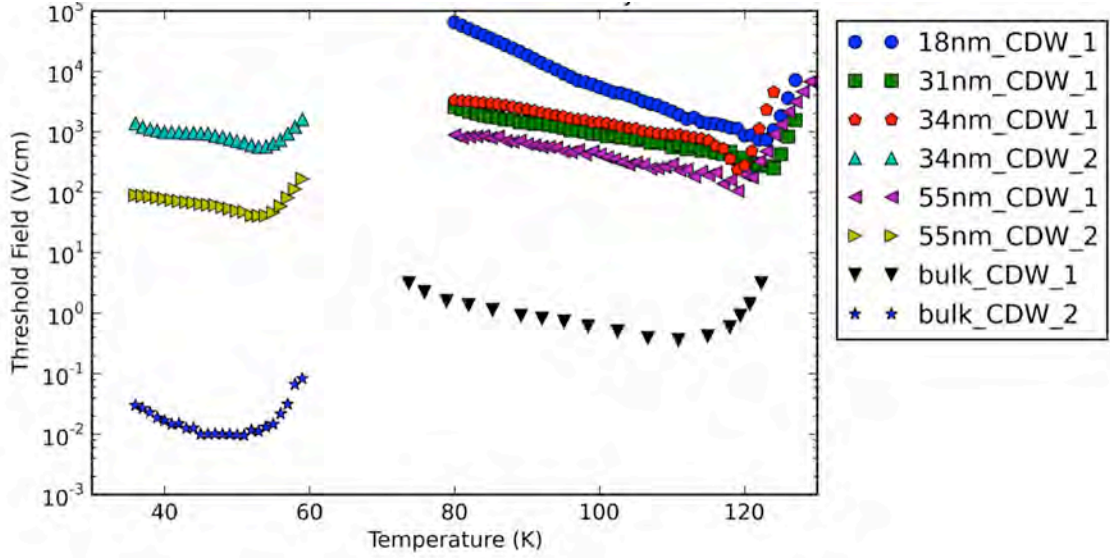


Figure 1.39: Threshold field versus temperature for the first and the second CDW in thin NbSe₃ crystals. The threshold field in both CDW states increases as the crystal becomes thinner. However, the second CDW threshold field diverges in very thin samples.

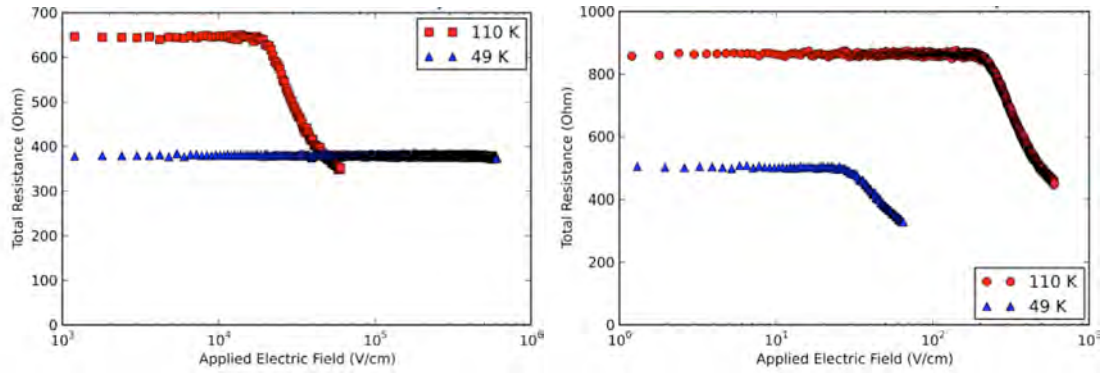


Figure 1.40: Differential resistance vs. applied electric field for (a) 18nm and (b) 5nm thick NbSe₃ crystals. No drop in the differential resistance was observed in the 18nm thick sample, which suggests the lack of sliding CDW state.

c) Narrow-Band Noise measurements

Peak noise frequency versus charge density current density for 31nm, 34nm, 55nm and the bulk NbSe₃ crystals, at 49K, are shown in Figure 1.41. In all instances f_{NBN} versus J_{CDW} show a linear relation where the slope of the fitting line becomes larger as the sample becomes thinner.

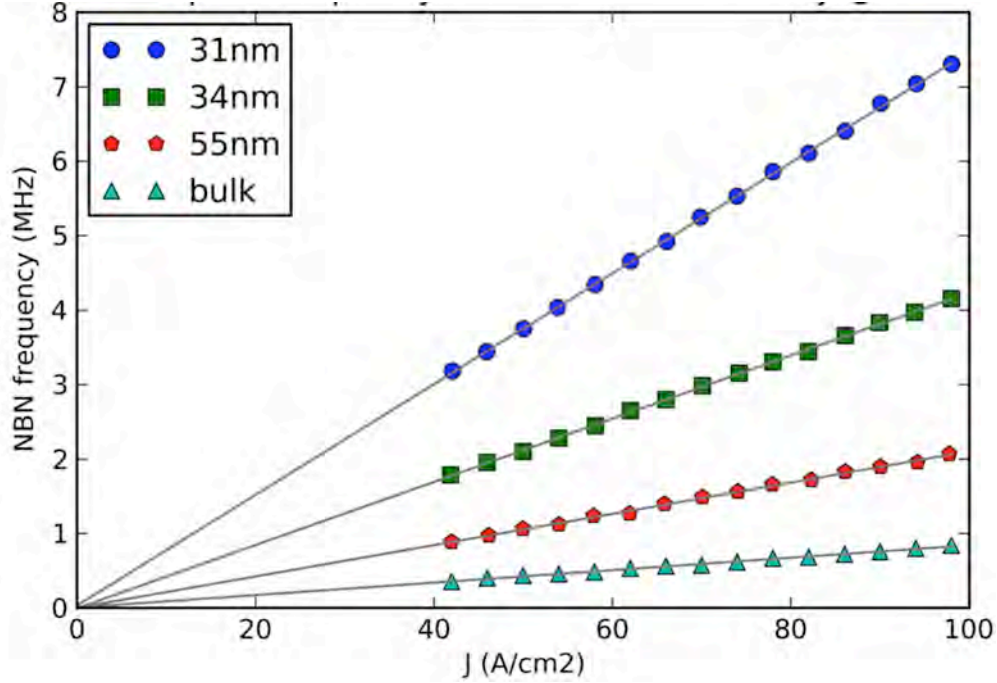


Figure 1.41: Narrow-band noise peak frequency vs. CDW current density for thin NbSe₃ crystals. The slope of the fitted line is proportional to the CDW carrier density.

From the slope of the fitted line, the charge carrier density can be estimated. Also the total CDW carrier density was estimated from the mean-field graph shown in Figure 1.36. Table 1.5 summarizes the n_c for different samples. This result suggests a decrease in the charge density wave carrier density, as the crystal becomes thinner.

Sample Thickness	Slope (MHz \times cm ² /A)	n_c (10 ²⁰ C/cm ³) (at T=49°K)	Total n_0 (10 ²⁰ C/cm ³) (Estimated at T=0K)
Bulk	0.008	55.65	88.12
55nm	0.021	22.47	37.45
34nm	0.042	10.78	17.98
31nm	0.074	6.02	10.04

Table 1.5: CDW carrier density for bulk and thin NbSe₃ crystals at 49°K (n_c) and 0 °K (n_0)

1.2.3 Discussion and Conclusions

McCarten et al [52] previously studied the effect of finite size and doping concentration on the charge density state in NbSe₃ and TaSe₃. In that study, NbSe₃ crystals thicker than 50nm were measured and “the vanishing of E_T in thin crystals near T_{P2} ,” “due to thermally assisted depinning of the CDW” was observed. [52] Furthermore,

they found that in “thin crystals, E_T increases with decreasing thickness as $E_T = K/t$, where K is roughly proportional to the impurity concentration.” They concluded that “the size dependence of CDW properties is due to a crossover in the dimensionality of the pinning from three to two dimensions which occurs when the crystal thickness becomes smaller than the CDW’s bulk transverse phase-phase correlation length.” [52]

The scotch-tape exfoliation method, and plasma treatment of the crystals before depositing the metal contacts, allowed us to further explore the effect of the dimension on NbSe₃ crystals, in the regime below 50nm.

While increasing of the threshold field in thin samples had been observed before, the asymmetrical nature of this effect had not been observed, and had been assumed to happen in crystals thinner than 50nm. Figure 1.42 show the threshold field versus temperature for NbSe₃ samples of various thicknesses from a previous study.

Furthermore, from table 1.5, the CDW carrier density at 49°K is observed to decrease in thinner samples. This decrease in the carrier density also suggests a weaker CDW state in the second CDW state in thin NbSe₃ crystals.

The size effect on CDW behavior can be explained by surface pinning interpretation. In small crystals (i.e. thinner samples), CDW “is more strongly pinned near crystal surfaces than in the bulk.” The surface pinning can be caused by surface impurities or by commensuration of the CDW wave vector with the underlying lattice period near the surface [66].

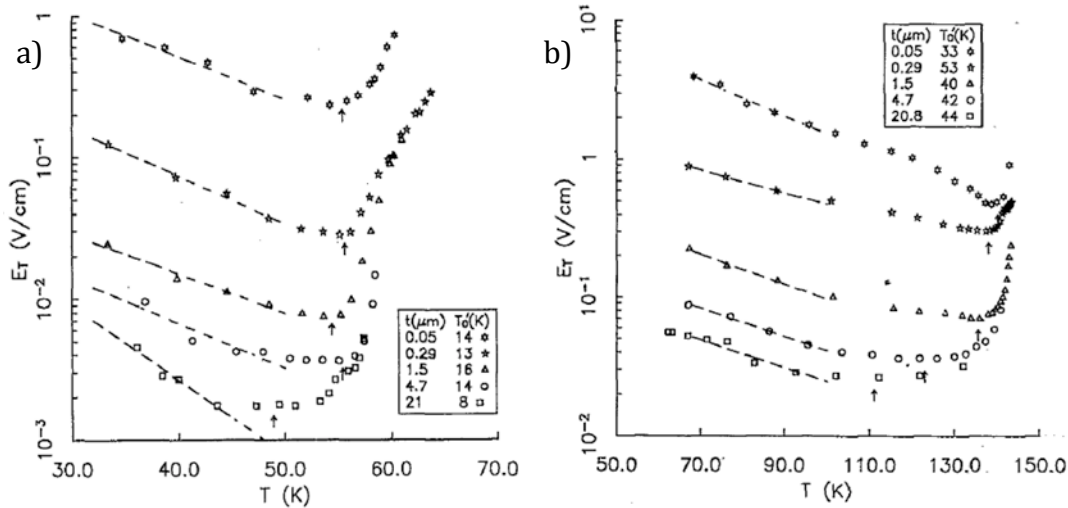


Figure 1.42: Threshold field vs. temperature for (b) the first and (a) the second CDW state in NbSe₃ with different thicknesses (above 50nm) [65].

As analyzed in [67], because of the surface pinning, E_T should be linearly proportional to the surface-to-volume ratio of the crystal. However, for ribbon line NbSe₃ crystals, with $w \gg t$:

$$\begin{aligned} \frac{\text{surface}}{\text{volume}} &= \frac{2 \times (l \times w + w \times t + l \times t)}{l \times w \times t} \\ &= 2 \times \left(\frac{1}{l} + \frac{1}{w} + \frac{1}{t} \right) \end{aligned}$$

$$\approx \frac{2}{t}$$

Therefore, $E_T \propto \frac{K}{t}$.

The threshold field for the first CDW state follows the $1/t$ rule as described in [67]. Figure 1.43 shows E_T versus t^{-1} for bulk and thin NbSe₃ samples at 120K. The dashed line is the fitted K/t line.

The transport measurement results on thin NbSe₃ crystals strongly suggest a non-symmetric effect on the first and the second charge density wave state—namely, that the second charge density wave is being pinned more strongly as the crystal becomes thinner. However, no apparent change in the transition temperature in either CDW states was observed. This asymmetric size effect was also observed in a previous study [52], in the form of vanishing E_T at T_{P2} .

Figure 1.44 shows the low-field resistance versus temperature in the first and the second CDW state regions. The asymmetric nature of the effect of the thickness can clearly be observed from these graphs.

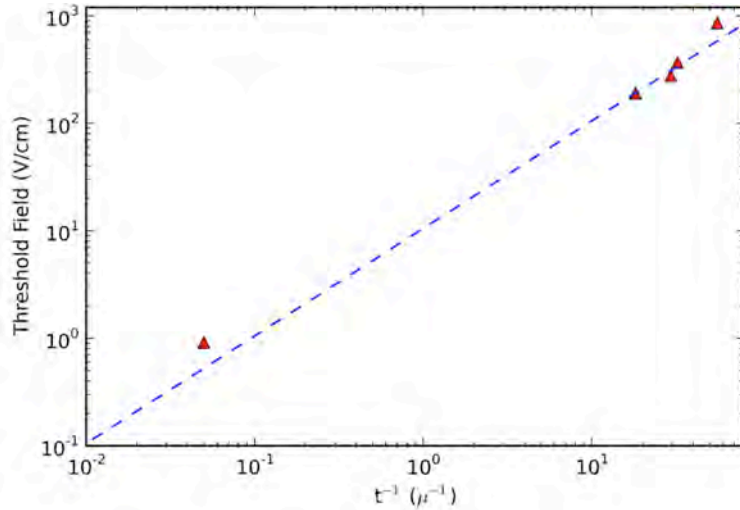


Figure 1.43: Threshold field versus inverse thickness at 120K. Dashed line is the fitted $1/t$ line. The threshold field follows $E_T \propto \frac{1}{t}$ rule in thin crystals, which suggests surface pinning mechanism.

The threshold field measurement (Figure 1.39) verifies the a-symmetrical nature of the size effect on CDW states in NbSe₃ further. From this graph, the threshold field of the second CDW state increases more rapidly than the first CDW, by reducing the thickness of the sample.

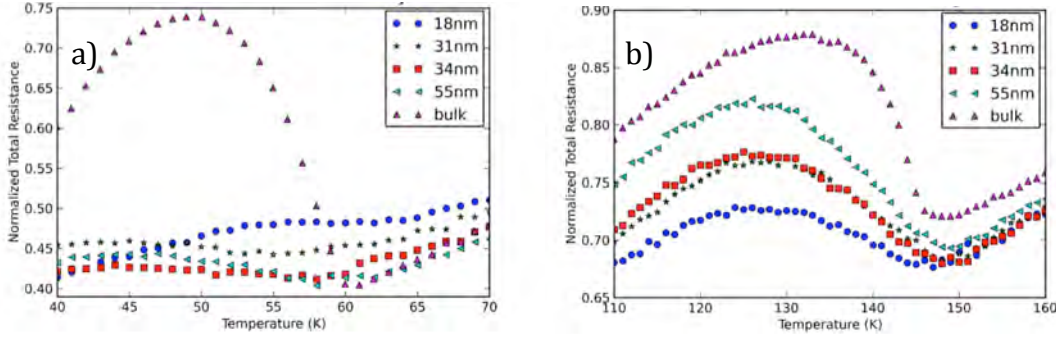


Figure 1.44: Low-field dc-resistance versus temperature in the first and the second CDW state in NbSe₃ bulk and thin crystals. As the crystals become thinner, the second CDW state deviates further from the bulk characteristics. However, the dc-resistance behavior in the first CDW region remains intact.

Theoretical analysis, along with experimental studies has concluded that the two CDW phases in NbSe₃ are independent, and therefore, have different properties and parameters. Band structure calculations by Shima et. al. [35] suggests that the localization of two NbSe₃ CDW phases occurs at two different reciprocal lattice locations. Furthermore, the first CDW phase, with T_{c1} transition temperature, localizes around two chains of III and III' (Figure 1.11-b). However, the second CDW phase, with T_{c2} transition temperature occurs around four chains I, II, I', II'. Therefore, “at two different sites of the two-chain area and the four-chain area, the effects of impurity [or surface] potential[s] on sliding modes which cause the non-Ohmic conduction may be different.”¹ [35]

In addition, due to the different localization chains of the two CDWs in NbSe₃, their respective orbital signatures are also different. The second CDW only has a d_{z^2} character, whereas the first CDW not only has a d_{z^2} character, but also a d_{xy} character. Therefore, “it is expected that an amplitude of CDW of the [first CDW] in the direction perpendicular to the chain is larger than that of the former.”

The difference in corresponding wave-vectors of the first and second CDW phases of NbSe₃ could explain their unequal finite-size effect. Figure 1.45 shows the x-ray diffraction scan through the (1, 2.243, 0) and (0.5, 2.263, 0.5) peaks at T=30K [65]. Also, the inset in this figure depicts the relative position of these peaks in the reciprocal space. This graph “demonstrate[s] the distinct difference between the chain-axis periodicity of the two CDW's”. Figure 1.46 (a) is a schematic of a thin exfoliated NbSe₃ crystal, and its corresponding crystal axis. Figure 1.46 (b) shows the NbSe₃ atomic structure, and also denotes a, b and c crystal axis [35]. The b-axis of the crystal is along the bulk needle axis, and corresponds to the largest length of thin exfoliated crystals, L.

The location of q_1 and q_2 in the reciprocal space suggests that the first CDW is exclusively formed along the b-axis (i.e. along the longest dimension in exfoliated crystals), whereas the second CDW has components parallel to the a-c plane (i.e. perpendicular to the longest dimension in exfoliated crystals). Thus, the perpendicular-to-

¹ The study cited in [35] only discusses the effect of impurity potentials. However, similar concept can be applied to surface potentials, which increases as the crystal dimension decreases.

b-axis component of the second CDW phase is strongly susceptible to the overall size of the crystal. Therefore, where no dramatic change in the first CDW phase was noticed, the second CDW phase was weakened considerably.

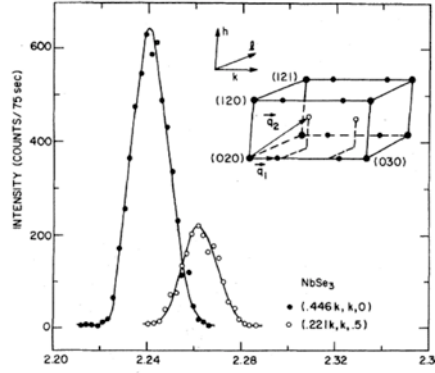


Figure 1.45: X-ray diffraction scans of the (1, 2.24, 0) and the (0.5, 2.26, 0.5) superlattice peaks at T=30 K. “The component of the CDW wave vector along b^* is clearly different for the two CDW's”. The q_1 and q_2 location in the reciprocal space is shown in the inset. [65]

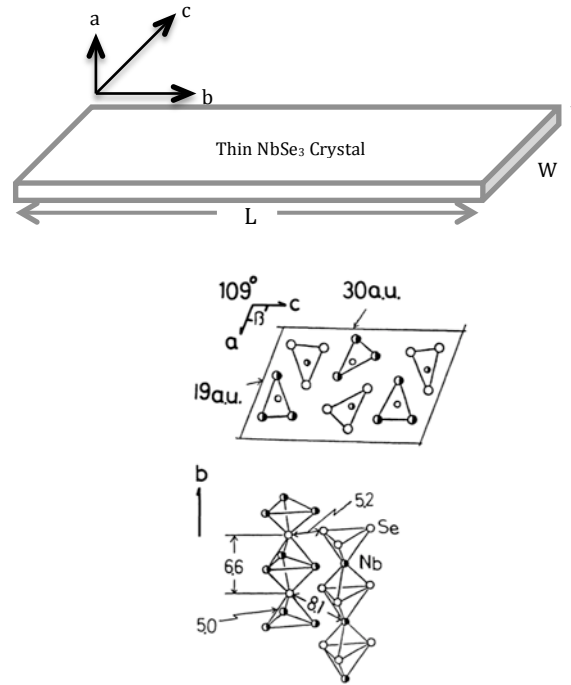


Figure 1.46: Exfoliated NbSe₃ crystals (b) and NbSe₃ crystal structure [35] (a). The largest dimension of exfoliated samples corresponds to the crystal b-axis.

1.3 Thin Blue Bronze $\text{K}_{0.3}\text{MoO}_3$ Crystals

I experimented with fabricating thin Blue Bronze $\text{K}_{0.3}\text{MoO}_3$ crystals using the exfoliation technique, similar to NbSe_3 crystals. The crystal structure of $\text{K}_{0.3}\text{MoO}_3$ is quasi-two-dimensional, as opposed to the crystal structure of NbSe_3 , which is quasi-one-dimensional. Also, the bonds between MoO_6 planes in $\text{K}_{0.3}\text{MoO}_3$ are stronger ionic bonds. Therefore, the scotch tape exfoliation approach is not very effective on blue bronze, because the bonds between the MoO_6 planes are too strong to break with the tape force. In the end, the thinnest crystals that I could fabricate were thicker than 60nm.

High contact resistance was another difficulty. Blue bronze crystals, even after plasma treatment, showed a relatively large contact resistance. I experimented with several materials as the metal contact, in order to achieve a low contact resistance. However, an acceptable contact resistance, similar to NbSe_3 , could not be realized.

Due to exfoliation problems and high contact resistance, I was not able to perform reliable electrical measurements on thin blue bronze crystals. However, here I describe the bulk crystal growth, exfoliation results, and discuss some preliminary results as a reference.

1.3.1 Device Fabrication and Characterization

1.3.1.1 Crystal growth

I used the electrochemical method to grow molybdenum bronze (blue $\text{K}_{0.3}\text{MoO}_3$ and red $\text{K}_{0.33}\text{MoO}_3$) crystals. The starting materials were K_2MoO_4 and MoO_3 with 99.99% purity from Sigma Aldrich®. I combined K_2MoO_4 and MoO_3 in 1:3.15 molar ratio, ground the mixture into a fine powder form, and melted it in a pyrex® beaker at 600°C. At this temperature, the two materials fused into one, and formed a black liquid. After cooling, I was left with a white solid material, which was a mixture of K_2MoO_4 and MoO_3 . Then, I re-ground the product into a fine power form, and placed it in another beaker, along with two platinum rods that were connected to a current source through a

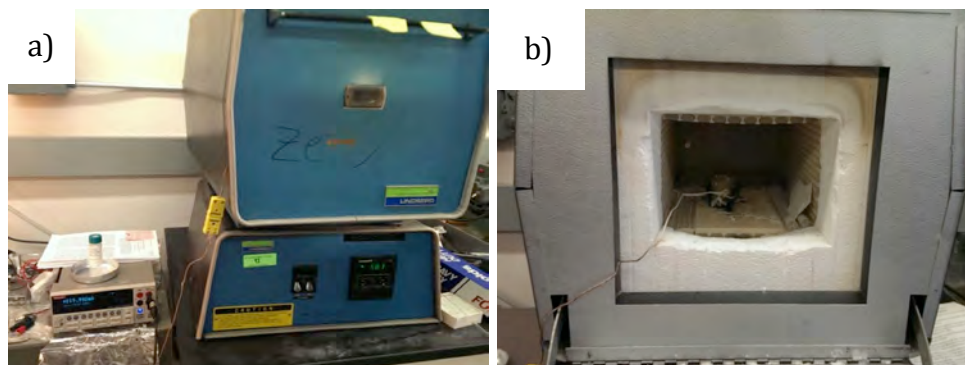


Figure 1.45: (a) The box oven and the current source used to grow the blue bronze $\text{K}_{0.3}\text{MoO}_3$ crystals. (b) The beaker containing a mixture of K_2MoO_4 and MoO_3 . The blue bronze crystals formed by passing a current through this mixture by a pair of platinum wires.



Figure 1.46: Optical image of blue bronze $\text{K}_{0.3}\text{MoO}_3$ crystals, grown with the electrochemical method. [68]

pair of heat-resistant wires.

The entire setup was then placed in a box oven and heated to 550°C . The crystal growth process was initiated with a 10mA of dc electric current. As the chemical reaction progressed, and the crystals were formed, the material inside the beaker became more resistive, and thus, the voltage increased to the source compliance value. The total reaction time was less than 24 hours. Figure 1.45 shows the box oven and the crystal growth system.

The precise temperature at which the reaction took place was crucial. In order for the electrochemical reaction to happen, the temperature of the material, had to remain slightly ($10\text{-}20^\circ\text{C}$) above its melting point. When the temperature was too low, the material would quickly solidify, and there would not be a reaction. On the other hand, when the temperature was too high, the internal energy of the ions were too high, and the applied electric field could not separate them and there would not be a reaction. I found that the optimal temperature for electrochemical growth of blue bronze crystals was $550\text{-}570^\circ\text{C}$.

The result of this electrochemical reaction was a hard black material. However, once it was cracked open, numerous small shiny crystals were spotted inside. This method resulted in both blue and red molybdenum bronze crystals. After removing the crystals from the rest of the material, they were separated based on their color. The typical size of the crystals was $2\text{mm} \times 2\text{mm} \times 1\text{mm}$. Figure 1.46 shows an optical image of blue bronze $\text{K}_{0.3}\text{MoO}_3$ crystals [68].

1.3.1.2 Exfoliation technique

As was mentioned before, exfoliation of blue bronze crystals was more difficult than NbSe_3 . The principal source of this difference was in the quasi-two-dimensional structure of blue bronze crystal, as opposed to the quasi-one-dimensional structure of NbSe_3 . In

order to achieve thin blue bronze samples, I tried several exfoliation approaches, and the most effective method was as follows:

Using a pair of tweezers, I held a small crystal of blue bronze a few centimeters above a clean piece of scotch tape, with its sticky side up. With a sharp razor, I scratched a corner of the crystal, and this resulted in several small $\text{K}_{0.3}\text{MoO}_3$ crystals on the tape. After that, I started the normal exfoliation with these small crystals. Because of their relatively small size, and thus large surface to volume ratio, the tape force could break plane-plane bonds, and successfully exfoliate them.

After exfoliating several times onto scotch tapes, I applied the final tape containing thin crystals to the target substrate, and examined exfoliated crystals on the substrate, under the optical and electron microscope. The thickness of the crystals was measured using an atomic force microcopy (AFM) system. I was able to exfoliate crystals with the thicknesses down to 10nm for NbSe_3 30nm for $\text{K}_{0.3}\text{MoO}_3$. Figure 1.47 shows the SEM micrograph of a typical NbSe_3 sample with exfoliated crystals on a silicon-silicon dioxide substrate with the pre-patterned alignment marks.

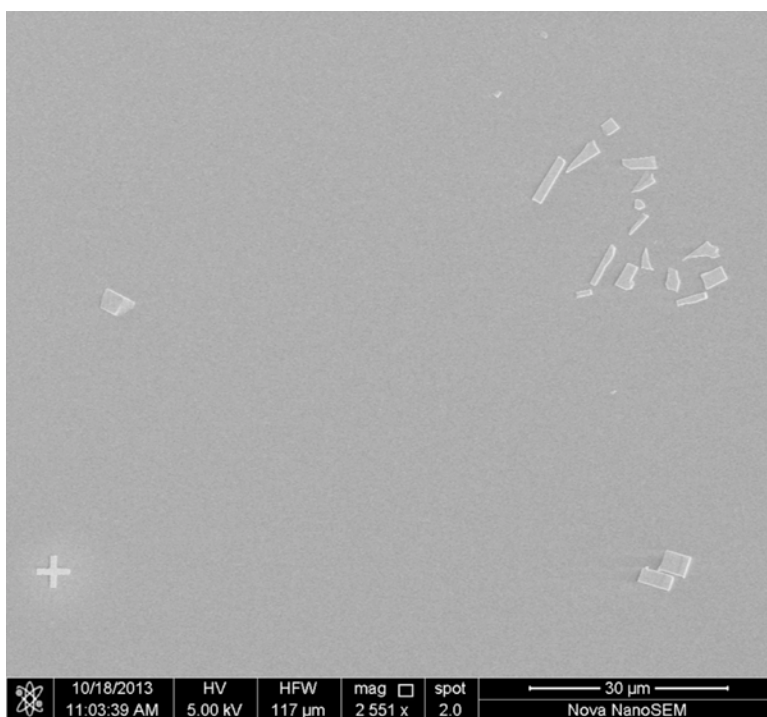


Figure 1.47: The SEM micrograph of blue bronze $\text{K}_{0.3}\text{MoO}_3$ crystals on a Si-SiO₂ substate with pre-patterned gold alignment marks

1.3.1.3 E-beam lithography and nitrogen plasma treatment

This step was preformed similar to what described for NbSe_3 crystals in section 1.2.1.3.

1.3.1.4 Electrical measurement methods

Room temperature electrical measurements, and preliminary resistance versus temperature measurements were performed in a cryogenic probe station system in the Zettl lab, which is located in 67 Birge Hall. Helium gas was used in order to cool down the sample down to 100°K. The CDW transition in blue bronze occurs at 180°K.

1.3.2 Results and Discussion

1.3.2.1 Exfoliation

The exfoliation technique, described in section 1.2.2, was effective in achieving blue bronze crystals as thin as 60nm. Figure 1.48 shows a Scanning Electron Microscopy (SEM) image of a typical exfoliated blue bronze sample (a) and its corresponding Atomic Force Microscopy (AFM) image (b). The inset in Figure 1.48 (b) is the height profile of the sample, which shows a ~90nm thin flake of blue bronze. The typical lateral dimension of the exfoliated crystals was 1-10μm.

Blue bronze crystal structure is composed of quasi-two-dimensional planes. Therefore, after exfoliation, low aspect ratio blue bronze crystals were expected. In my experiments, the typical aspect ratio of exfoliated blue bronze crystals were 1:1-1:3. However, in addition to the typical low-aspect ratio blue bronze crystals, a large number of high aspect ratio (larger and 1:10) blue bronze crystals were also observed. Further characterizations are required to find the crystal orientation of these crystals.

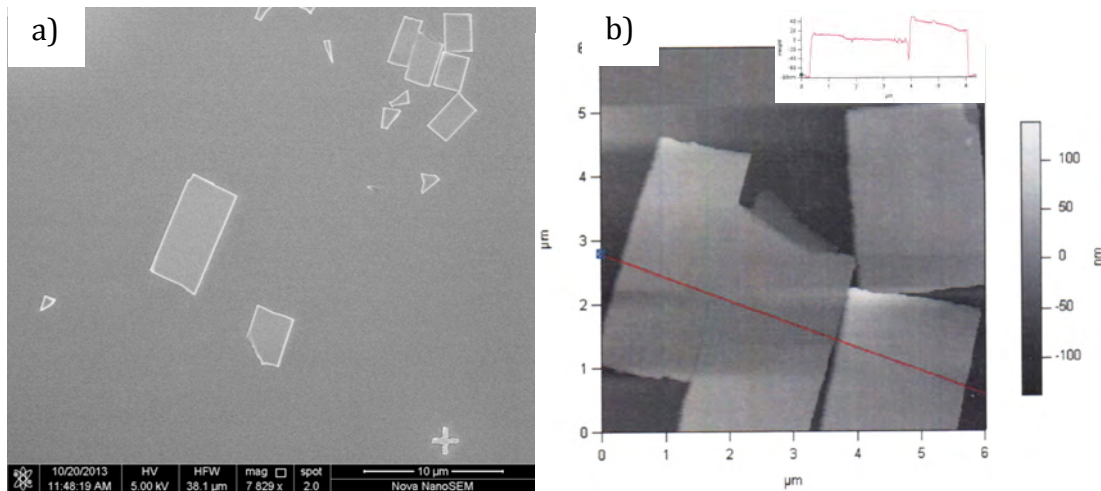


Figure 1.48: a) SEM micrograph b) AFM image of exfoliated blue bronze crystals. The inset in (b) is the height profile along the red line and shows a 90nm thin flake of blue bronze.

1.3.2.2 Contact resistance and plasma treatment

The plasma treatment step was performed on all blue bronze thin crystals, before contact metal deposition. Even though, the nitrogen plasma step reduced the contact resistance significantly, a typical residual contact resistance after the plasma treatment

step was 200-250% of the total crystal resistance. This value was calculated using the special conductivity of blue bronze [8]. Figure 1.49 shows a SEM image of a thin blue bronze device, fabricated on a Si-SiO₂ substrate.

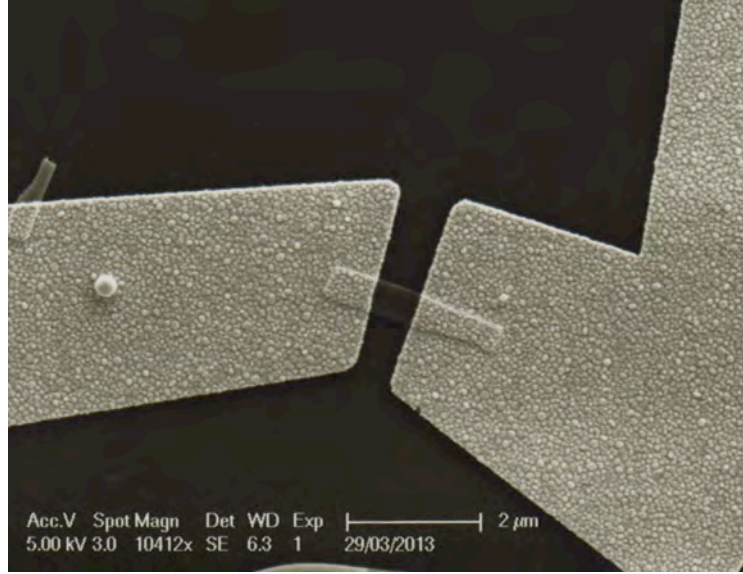


Figure 1.49: SEM image of a blue bronze device. An indium-chromium-gold tri-layer was used as the metal contact. A plasma treatment step enhanced the ohmic contact.

1.3.2.3 Device fabrication

Figure 1.50 (a) to (c) shows the different stages of the fabrication process for blue bronze. Exfoliated crystals on a silicon dioxide substrate, with pre-fabricated alignment marks, are shown in the SEM micrograph in Figure 1.50 (a). Next, large metal pads were patterned using an NPGS-SEM machine in the Zettl lab. This is depicted in the colored SEM image of Figure 1.50 (b). Finally, using a Crestec e-beam lithography machine in the Marvell Nanolab, the blue bronze and NbSe₃ crystals were connected to the large metal pads. This is shown in the optical image in Figure 1.50 (c). Two and Four-contact devices were fabricated in order to measure the contact resistance.

1.3.2.4 Preliminary electrical measurements

After plasma treatment, the blue bronze resistance decreased from few giga ohms to few tens of kilo ohms. Initial results from electrical measurements on thin blue bronze crystals suggest an increase in the CDW transition temperature. Blue bronze, in its bulk form, has a metal to semiconductor transition at 180K. In the resistance versus temperature measurement of a 60nm thin crystal of blue bronze, a transition temperature of 205°K was observed. However, more experiments are required in order to verify this finding, and determine its origin.

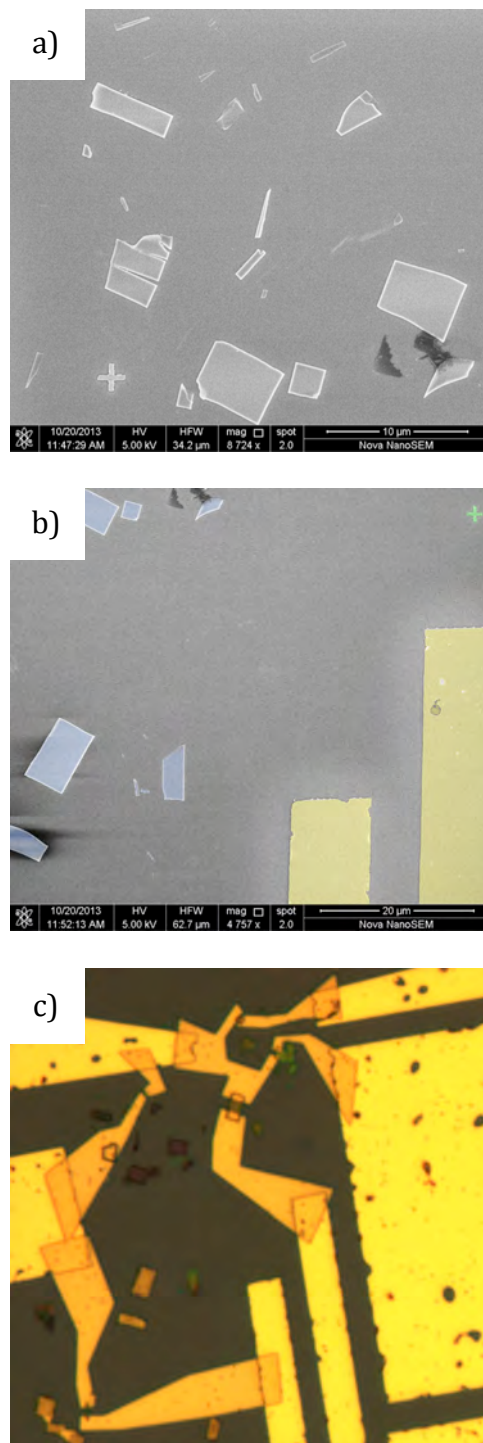


Figure 1.50: Fabrication process of a single blue bronze device. (a) The exfoliated crystals were analyzed and the desired crystals were mapped using SEM technique. (b) Large metal pads (Ti-Au bi-layer shown in yellow) were patterned with e-beam lithography using an NPGS system. (c) Small metal wires (In-Cr-Au tri-layers) were patterned to connect the crystals to large pads, with an e-beam lithography technique, using the Crestec machine at the Nanolab.

Chapter 2

Graphene under periodic potential

2.1 Theories and Background

Long before the first report of exfoliated graphene by Andre Geim [1,2], numerous theoretical studies on graphene had been conducted and published in the literature [3,4]. There were also multiple attempts to experimentally fabricate this material [5-8]. However, in the end, Andre Geim and Konstantin Novoselov won the 2010 Nobel Prize in Physics for “groundbreaking experiments regarding the two-dimensional material graphene” [9].

Since then, there have been countless experimental and theoretical investigations into the properties of this new material. These investigations have revealed several unique physical and electronic properties, along with many realized and potential applications.

In this section I give a brief background on Graphene and some of its unique electronic properties. My focus is on the behavior of charge carriers in graphene under an external periodic potential. Since, in first approximation, graphene can be considered a two-dimensional electron gas system, I start with summarizing the general properties of two-dimensional electron systems. Next, I review the theory of the unique band structure of graphene. And finally, I study the effect of applying a potential superlattice on a sheet of graphene.

2.1.1 Two-dimensional electron systems

A conductor forms a “two-dimensional electron system” (2DES), when its thickness is smaller than the wavelength of the electrons inside. Such a system, if the Coulomb interaction is ignored, can be approximated as a “gas” of free particles, or a “two-dimensional electron gas” (2DEG). 2DEG is able to move with no resistance in the 2D plane. In this approximation, electron movement along the third axis could be ignored. Several interesting quantum effects arise in such a system.

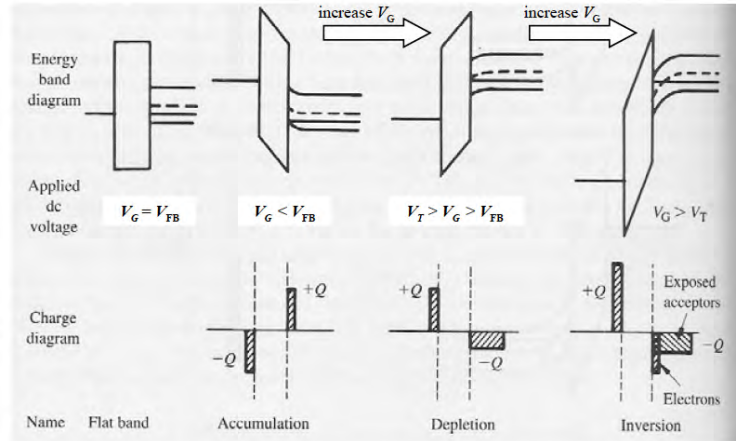


Figure 2.1: The energy band and charge diagram of a MOSFET device in flat band, accumulation, depletion and inversion ($V_G > V_T$) condition. The inversion layer can be modeled as a 2DES [10].

The most commonly known applications of 2DES are in MOSFETs (metal–oxide–semiconductor field-effect transistor) and HEMTs (high-electron-mobility transistors). In Figure 2.1 a schematic of a typical MOSFET band diagram is shown [10]. And, Figure 2.2 is the typical band-diagram of a GaAs/AlGaAs HEMT device [11].

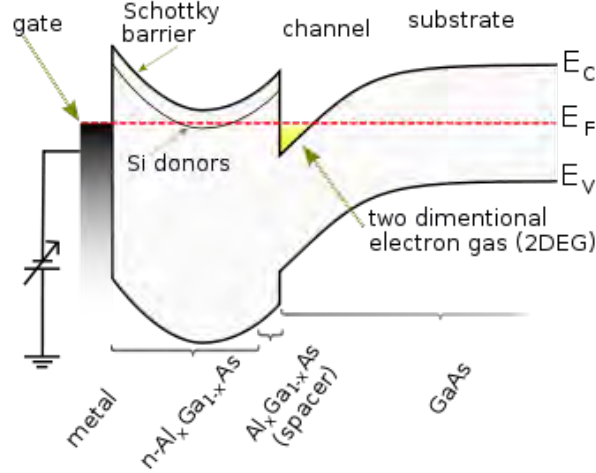


Figure 2.2: The typical band diagram of a GaAs/AlGaAs high electron mobility transistor (HEMT) device. A 2DEG is formed at the heterojunction. [11]

Elementary quantum mechanics tells us that an electron in a potential well $V(z)$ only occupies one of discrete energy levels E_n . If the electron is only trapped in one direction, but is free to move along the other two directions, using the effective mass theory, the wavefunction of such an electron could be found by solving [12]

$$[E(-i\nabla) + H']\Psi = i\hbar \left(\frac{\partial \Psi}{\partial t} \right) \quad (2.1)$$

where $H' = V(z)$. The energy of an electron in crystal could be expressed in terms of its reciprocal lattice wavenumber k . In a hypothetic infinite crystal, $E(k)$ forms energy bands. The first order approximation of energy eigenvalues near the band edge can be written as

$$E(\vec{k}) = E(\vec{k}_0) + \frac{1}{2} \sum_{i,j} \left(\frac{\partial^2 E}{\partial k_i \partial k_j} \right) k_i k_j \quad (2.2)$$

Hence, the $E(-i\nabla)$ operator in equation (2.1) can be written as

$$E(-i\nabla) = \sum_{i,j} \frac{p_i p_j}{2m_{i,j}} \quad (2.3)$$

Here, p_i and p_j are momentum operators, and the effect of the periodic potential is expressed in terms of the effective mass tensor

$$p_i = \frac{\hbar}{i} \frac{\partial}{\partial x_i} \quad (2.4)$$

$$\frac{1}{m_{ij}} = \frac{1}{\hbar^2} \frac{\partial^2 E(\vec{k})}{\partial k_i \partial k_j} \bigg|_{\vec{k}=\vec{k}_0}$$

Here, $1/m_{ij}$ components are evaluated at the band edge (k_0).

When $1/m_{ij}$ matrix is diagonal, the answer to $H\Psi = E\Psi$ is a function Ψ with the following general form:

$$\Psi_{n,k_x,k_y} = e^{ik_x x} e^{ik_y y} f_n(z) \quad (2.5)$$

where $f_n(z)$ is a solution to the equation

$$-\frac{\hbar^2}{2m_{zz}} \frac{d^2 f_n}{dz^2} + V(z)f_n = E_{n,z} f_n \quad (2.6)$$

Therefore, the total energy of electron is

$$E_n(k_x, k_y) = E_{n,z} + \frac{\hbar^2}{2m_{xx}} k_x^2 + \frac{\hbar^2}{2m_{yy}} k_y^2 \quad (2.7)$$

The $E_{n,z}$ energies ($n = 0, 1, 2, \dots$) have discrete values. Thus, each $E_n(k_x, k_y)$ form a “sub-band”, which is labeled by its corresponding n-value. Since electrons in these sub-bands are free to move in k_x and k_y directions, they can be modeled as a 2D electron gas system.

2.1.2 Theory of Graphene

Crystal structure

Graphene is a single sheet of carbon atoms, which are connected through sp^2 hybridization bonds. The resulting honeycomb structure is shown in Figure 2.3. The side length of a graphene unit cell is 2.461\AA [13]. Calculating the density of carbon atoms in this structure is a straightforward task and the result is 3.81×10^{15} atoms/cm². In graphite, which consists of graphene sheets stacking in a particular orientation (AB or Bernal stacking), the distance between the sheets is 3.37\AA [3]. In “AB” or Bernal stacking, adjacent graphene sheets are shifted by $1/3$ of a lattice constant, because it provides the most energetically favorable structure. This can be seen in Figure 2.4.

Graphene unit cell consists of two carbon atoms, which form two separate sublattices, A and B. Each sublattice is a network of triangles, and a graphene sheet can be visualized as a combination of the A and B sublattices, which are shifted relative to each other.

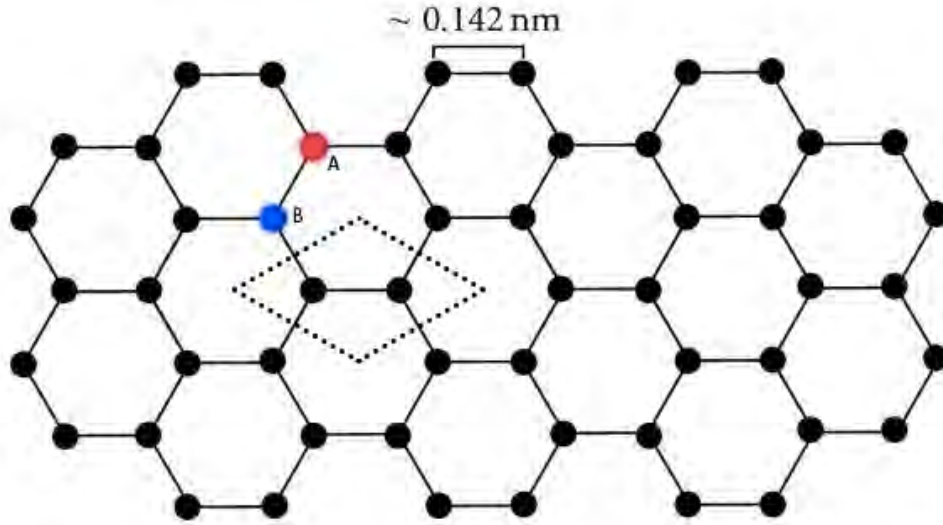


Figure 2.3: Graphene honeycomb structure. There are two atoms per unit cell and hence the crystal is made from two separate sublattices A and B. The nearest-neighbor carbon-carbon distance is 1.42 Å.

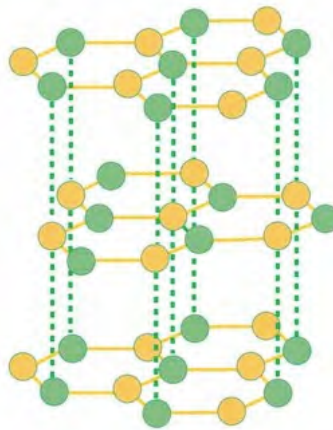


Figure 2.4: Graphite AB or Bernal stacking is energetically, the most favorable structure for graphene sheets.

Band structure

The energy band structure of graphene can be calculated using the tight-binding method, with considering the second-hopping correction [13]. Using this method, at the M-point of the reciprocal lattice, a 4 eV, and at the Γ -point, a 19 eV energy gap are observed [13]. The resulting band structure is six-fold symmetric, and the conduction and valence bands meet each other at K and K' points; thus, form six cones or “valleys”. However, only two of these valleys are unique and they are often referred to as the Dirac points.

By solving the energy spectrum of carriers in graphene, within a tight-binding Hamiltonian, it is straightforward to show that [14].

$$E_{\pm}(\mathbf{k}) = \pm t\sqrt{3 + f(\mathbf{k})} - t'f(\mathbf{k})$$

$$f(\mathbf{k}) = 2 \cos(\sqrt{3}k_y a) + 4 \cos\left(\frac{\sqrt{3}}{2}k_y a\right) \cos\left(\frac{3}{2}k_x a\right) \quad (2.8)$$

In this relation, the plus sign describes the upper band, and the minus sign describes the lower band. The band structure of graphene is shown in Figure 2.5.

By expanding the band structure in equation 2.6, close to K and K' vectors (i.e. the Dirac points), one can obtain the famous Dirac point energy-momentum dispersion relation as

$$E_{\pm}(\mathbf{q}) = \pm v_F |\mathbf{q}| + O\left[\left(\frac{q}{K}\right)^2\right] \quad (2.9)$$

where $v_F = 3ta/2$ is the Fermi velocity, and its value is $v_F \sim 10^6$ m/s. The onset in Figure 2.5 shows one of these Dirac points.

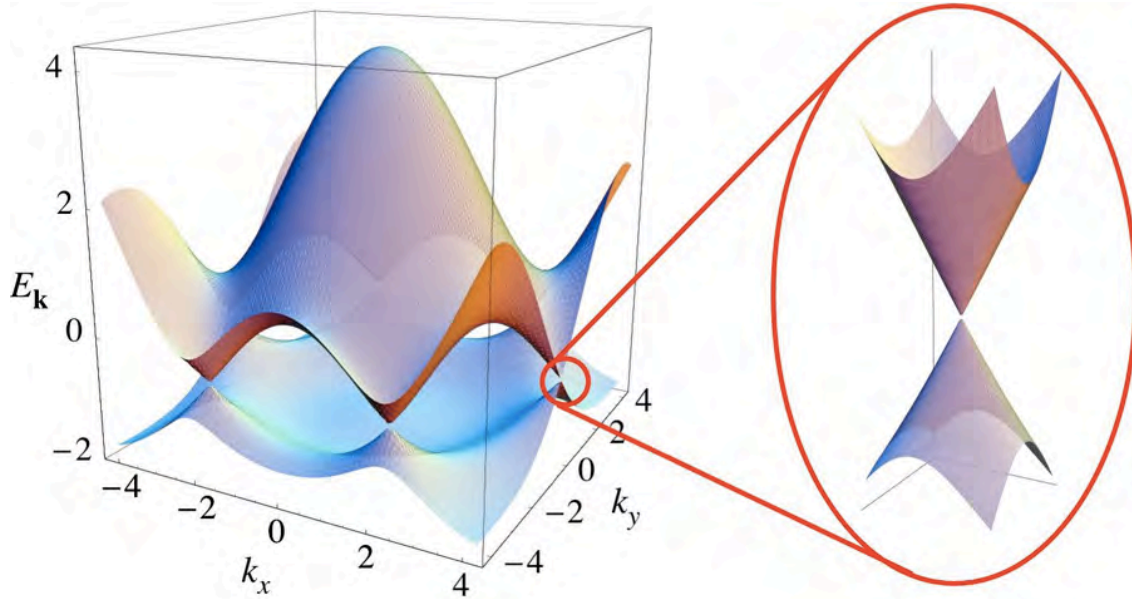


Figure 2.5 Band structure of graphene. Conduction and valence bands meet at K-points of the reciprocal lattice. These points are called Dirac points. At a Dirac point, the energy-momentum dispersion is linear [14].

The energy-momentum relation at each of these points, as the name suggests, is identical to the massless Dirac equation. The only difference is the existence of a “pseudospin” instead of the fermion spin. This pseudospin emerges from the phase difference of electron wavefunctions on two sublattices, and is responsible for the change in the electron mobility in the presence of an external periodic potential, as is discussed in section 2.1.3.

Density of states

The energy band structure around each Dirac points is symmetric. Therefore, one can calculate the density of states, using the standard procedure as follows [15].

The k-space volume of a single state is $(2\pi)^2/A$ (where A is the area of the sample). Thus, the total number of carriers in the material can be written as

$$N = 4 \frac{\pi k_F^2}{4\pi^2/A} = \frac{k_F^2 A}{\pi} \quad (2.10)$$

The factor of 4 comes from spin and “valley” degeneracy in graphene. Valley degeneracy stems from the existence of two energetically identical Dirac cones in graphene. Therefore, the Fermi wave vector k_F is only a function of 2-D charge density n in the material, i.e. $k_F = \sqrt{\pi n}$.

To calculate the density of state, we need to write N as a function of E_F . By assuming linear dispersion around the Dirac points, $E_F = \hbar v_F k_F$:

$$N = A \frac{E_F^2}{\pi \hbar^2 v_F^2} \quad (2.11)$$

Thus, the density of states per unit sample area will be

$$D(E_F) = \frac{2|E_F|}{\pi \hbar^2 v_F^2} = \frac{2\sqrt{n}}{\sqrt{\pi} \hbar v_F} \quad (2.11)$$

Relation 2.11 shows a zero density of states at the Fermi level.

Mobility

In the Drude model for electron transport, we assume that the charge carriers frequently scatter as they move inside a medium [16]. Therefore, in order to characterize the transport properties of a material, two parameters are needed: 1- the number of charge carriers (n) and 2- a parameter that shows how easy it is for electrons to travel through the material. This parameter could be either mobility μ , mean scattering time τ , or mean free path λ .

For graphene samples in this study, Drude model is valid because, the sample size is generally larger than the mean free path of electrons. Therefore, electrons undergo several collisions in traveling through the sample.

In Drude model, the conductivity σ can be written as

$$\sigma = ne\mu$$

where n is the carrier concentration, e is the electron charge, and μ is the mobility of charge carriers.

2.1.3 Effect of a periodic potential on graphene

The unexpected and interesting behavior of charge carriers in graphene under periodic potential, has been investigated theoretically [17-18], and realized experimentally in recent years. One example of such behaviors is the highly anisotropic propagation of charge carriers in graphene, where the group velocity of electrons could reduce to zero in one direction but remain unchanged in others [18]. Figure 2.6 is a schematic of graphene in a 1D (a) and a 2D (b) periodic potential.

In order to investigate this effect, consider applying a superlattice potential, with a spatial period, which is much larger than the nearest-neighbor carbon-carbon distance, on a sheet of graphene. In this situation, the momentum transfer from the superlattice is too small to scatter graphene electrons from one Dirac point to the other Dirac point. Therefore, one can simply study one Dirac point, without losing any information.

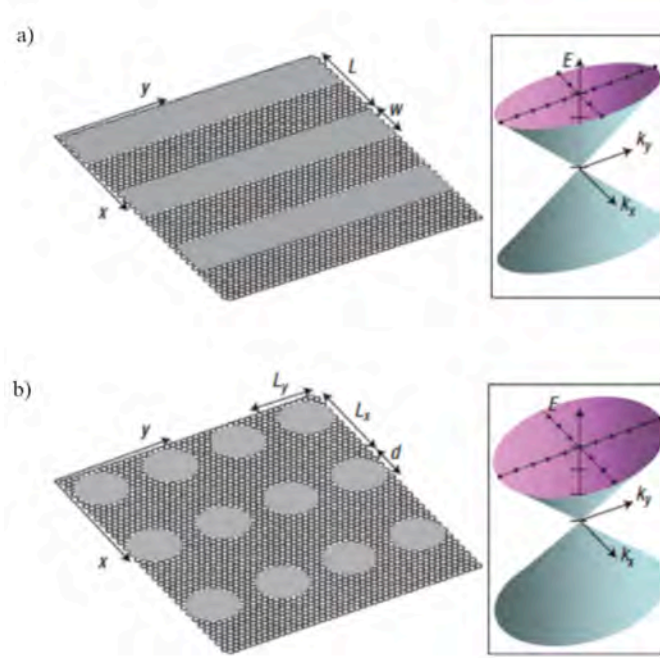


Figure 2.6 graphene under periodic potential or superlattice. The spatial period of the external potential is much larger than the nearest-neighbor carbon-carbon distance [18].

Since the unit cell of graphene has two carbon atoms, a two-component basis vector can represent charge carriers eigenstates. Working in the effective-hamiltonian formalism, the Hamiltonian that electrons, in the states that are near the K-point, feel can be written as:

$$H_0(\vec{k}) = \hbar v_0 \begin{pmatrix} 0 & -ik_x - k_y \\ ik_x - k_y & 0 \end{pmatrix} \quad (2.13)$$

where v_0 is the Fermi velocity, and \vec{k} the wavevector of quasiparticles, measured from the K point. The eigenstate of this Hamiltonian is

$$\langle \vec{r} | s, \vec{k} \rangle = \frac{1}{\sqrt{2}} e^{i(\vec{K} + \vec{k}) \cdot \vec{r}} \begin{pmatrix} 1 \\ i s e^{i\theta_k} \end{pmatrix} \quad (2.14)$$

where s is +1 or -1 for the eigenstate above or below the Fermi energy, respectively. And θ_k is the angle between the \vec{k} vector and \hat{k}_x direction. In this formalism, the energy spectrum is

$$E = s\hbar v_0 k \quad (2.15)$$

Then, when a periodic potential $U(r)$ is applied to graphene, the scattering amplitude between states can be written as:

$$\langle s, k | U(r) | s', k' \rangle = \sum_G \frac{1}{2} \left(1 + s s' e^{-i\theta_{k, k-G}} \right) U(G) \delta_{k', k-G} \quad (2.16)$$

Here G and $U(G)$ are the reciprocal lattice vector, and the corresponding Fourier transform component of the external periodic potential, respectively. And $\theta_{k, k-G}$ is the angle between $k - G$ and k . From 2.16, the energy dispersion relation and eigenstates of quasiparticles of graphene in a periodic potential can be obtained, by solving the following set of linear equations:

$$\begin{aligned} (E - \varepsilon_{s,k}) c(s, \vec{k}) = \\ \sum_{s', G} \frac{1}{2} \left(1 + s s' e^{-i\theta_{k, k-G}} \right) U(G) c(s', k - G) \end{aligned} \quad (2.17)$$

where E is the superlattice energy eigenvalue, and $\varepsilon_{s,k} = s\hbar v_0 k$ is the energy of quasiparticles before applying the periodic potential. $c(s, k)$ and $c(s', k - G)$ are amplitudes of the mixing among different unperturbed quasiparticle states.

For a weak external potential, where $U(G) \ll v_0 |G|$, quantum perturbation theory gives a moderately accurate approximation, which is also physically intuitive. Using the second order perturbation approximation

$$\frac{v_k - v_0}{v_0} = - \sum_{G \neq 0} \frac{2|U(G)|^2}{v_0^2 |G|^2} \sin^2 \theta_{k, G} \quad (2.18)$$

From Equation (2.18), it is clear that for weak external potentials, the amount of velocity renormalization scales with the square of potential amplitude. For a hypothetic material similar to graphene, except with no chiral carriers, Equation (2.16) becomes

$$\langle s, k | U(r) | s', k' \rangle = \sum_G U(G) \delta_{k', k-G} \quad (2.19)$$

And thus, Equation (2.18) becomes

$$\left(\frac{v_k - v_0}{v_0} \right)_{\text{non-chiral}} = - \sum_{G \neq 0} \frac{2|U(G)|^2}{v_0^2 |G|^2} \quad (2.20)$$

Equation (2.20) shows that the velocity renormalization in a non-chiral electronic system is isotopic, and independent of the transport direction.

One-dimensional graphene superlattice

Solving the set of equations 2.17 shows that for the states with wavevector k , the group velocity is highly anisotropic, and is a strong function of the k direction. For example, the normalized group velocity as a function of wavevector angle, for a 1D Kronig-Penny type periodic potential, with various barrier heights of U , spatial periods of L , and barrier widths of W is

$$\frac{v_k - v_0}{v_0} = - \left\{ \frac{U_{1D}^2 L^2}{\pi^4 v_0^2} \sum_{n>0} \frac{1}{n^4} \sin^2 \left(\frac{\pi w}{L} n \right) \right\} \sin^2 (\theta_{k,\hat{x}}) \quad (2.21)$$

This function is plotted in figure 2.7.

Figure 2.7 shows that for those states that their corresponding k vector is perpendicular to the periodic direction (v_{\perp}), group velocity is reduced the most. Whereas, when the k vector is parallel to the periodic direction, the group velocity is not changed whatsoever. This is a counter-intuitive outcome; because, the group velocity is reduced the most when charge carriers are moving parallel to the barriers, but it is not changed when the carriers are crossing the barriers.

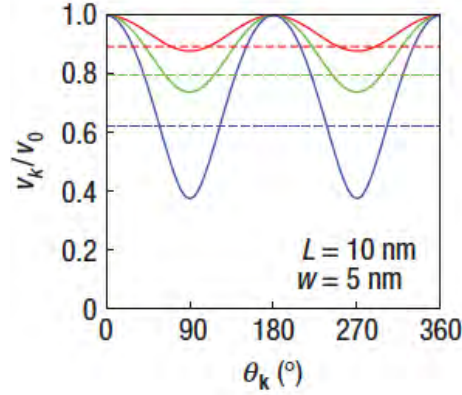


Figure 2.7: The group velocity of charge carriers parallel to k vector (k measured from the Dirac point) versus the angle θ_k between the k -vector and the direction of the periodic potential [18].

One can reduce the parallel-to-potential component of the group velocity to zero, by changing the potential height while keeping L and w constant, or by changing L while keeping U and w constant. These conditions are shown in Figure 2.8 and Figure 2.9, respectively.

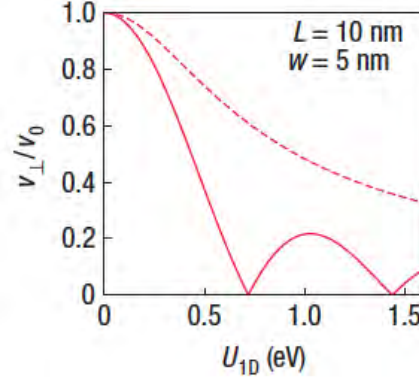


Figure 2.8: The group velocity of charge carriers in a 1D graphene superlattice, with k perpendicular to the periodic direction, v_{\perp} , in units of v_0 , versus U_{1D} (solid line), and that in a superlattice made from a fictitious system of non-chiral fermions with properties otherwise identical to those in graphene (dashed line) [18].

It is important to keep in mind that this phenomenon is a unique characteristic of charge carriers in graphene. And the pseudospin behavior of these carriers is responsible for this anisotropy. In order to better understand the physics of this effect, consider an invented two-dimensional system, identical to graphene in every aspect except the charge carrier chirality. When a 1D periodic potential is applied to this non-chiral 2D electron system, the group velocity will be reduced isotropically. The behavior of this system is shown with dotted line in Figure 2.8.

Another interesting phenomenon in graphene superlattices is energy gap opening at the edge of the brillouin minizone, as shown in Figure 2.10. When the chirality of charge carriers is not considered, gap opening at the MB is nearly constant and independent of k . However, in graphene, due to the pseudospin characteristic of charge carriers, the energy gap is a strong function of k , and is vanished when k is along the periodic potential direction, which is equivalent of minizone center in the reciprocal lattice.

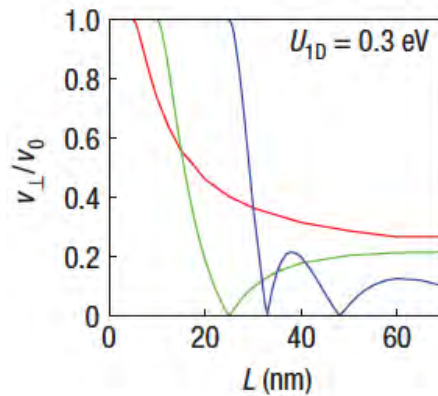


Figure 2.9: Graphene charge carriers' v_{\perp} versus spatial period (L) of the external periodic potential. Red, green and blue lines correspond to different potential widths (w) of 5 nm, 10 nm and 25 nm, respectively [18]. The external potential barrier height is kept fixed.

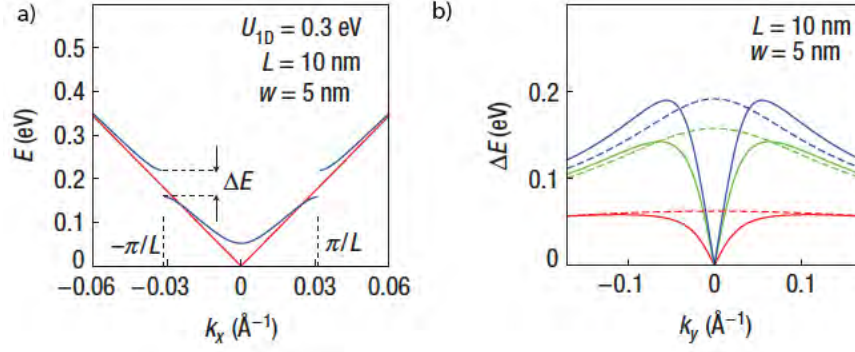


Figure 2.10: Energy gap at the superlattice Brillouin zone or MB of a 1D graphene superlattice. a) Energy of charge carriers in a 1D graphene superlattice versus the component of the wavevector k parallel to the periodic potential direction (k_x) at a fixed k_y . Red and blue lines correspond to k_y being zero and 0.012 \AA^{-1} , respectively. b) ΔE versus k_y for charge carriers in a 1D graphene superlattice (solid lines) and that in a superlattice made from a fictitious system with states without chirality but otherwise identical to graphene (dashed lines). Red, green and blue lines correspond to U_{1D} being 0.1 eV, 0.3 eV and 0.5 eV, respectively [18].

Particularly, this absence of the gap at the center of the minizone, can be explained as follows: Since the scattering potential's periodicity is much larger than the inter-carbon distance, it is not able to back-scatter the charge carriers [19-21], and therefore no energy gap opens at the center of the MB.

2.2 Device Fabrication

Prof. Steven Louie and his research group provided the theoretical inputs for this project.

2.2.1 Exfoliation of graphite

Mechanical exfoliation or “scotch-tape” technique is the first reported method for fabrication of graphene sheets [1]. Due to the weak interplanar pi-bonds, and strong in-plane sigma bonds, individual sheets of graphene can be removed from the graphite bulk by the scotch-tape exfoliation method.

In this method, first, Kish graphite or highly oriented pyrolytic graphite (HOPG) was thinned down with a sterile sharp razor blade, on a clean glass or mica surface. Then, a thin flake of graphite was transferred to a piece of scotch tape. After multiple folding and unpeeling of the tape onto itself, the graphite flake gradually became thinner, and randomly sized and distributed flakes of single or few sheets of graphene were made. Usually, when the majority of graphite flakes became optically transparent, the chance of finding single layer graphene sheets was maximized.

Then, the scotch tape containing thin graphite flakes were applied to a previously cleaned and prepared substrate. After leaving the tape on the sample for few minutes, the tape was removed slowly, and the substrate was examined under the optical microscope. Single sheets of graphene are distinguishable under optical microscope. Next, the tape residue was removed by merging the sample in acetone for few minutes, and a subsequent rinse in Isopropanol Alcohol-IPA.

The exfoliation process, which results in far better graphene quality than other methods (specifically CVD), is inherently a random process. And this randomness is one of the main disadvantages of using graphene in industrial applications.

A few notes on mechanical exfoliation of graphene:

- In order to achieve the maximum tape-to-substrate transfer rate, the substrate has to be very clean, and previously treated with weak oxygen plasma for a short period of time. In my experience 30 seconds of oxygen plasma at 50 W power and 50 sccm flows was sufficient.¹
- The brand and the type of tape are critical in the outcome. For example, the commonly used red scotch tape leaves an excessive amount of residue. I experimented with several tape brands, and I concluded that the blue dicing tape, has enough adhesion to exfoliate graphene, and leaves the least amount of residue on the substrate. I acquired this type of tape from the Berkeley Nanolab facilities.
- Distinguishing between single and few layer graphene flakes was challenging. A graphene flake sitting on a silicon substrate with 285nm of silicon oxide shows a high optical contrast with the substrate, and thus, easy to distinguish under an optical microscope. However, the contrast between single and multi layer flakes is small. I had access to the optical microscope equipment at Prof. Crommie’s lab, which includes RGB spectrum analyzer software. By analyzing the captured image of

¹ These parameters are specifically tuned for the plasma etching system at the Zettl lab in Physics Department of UC Berkeley.

exfoliated flakes on the substrate, this software determined whether a particular area of a flake is a single or a multi layer graphene sheet. In addition, I confirmed the number of layers with Raman spectroscopy.

Figure 2.11 shows a typical exfoliated graphene sample. I used substrates with 285nm of SiO₂ on Si for all my experiments. Before graphene transfer, I prepared the substrate by patterning a network of alignment marks (20 μm apart), using photolithography, depositing a Titanium-Gold (5nm-50nm respectively) bilayer, and a subsequent lift-off. I used this alignment mark network, to pattern the contact electrodes. Also, I treated the substrates with oxygen plasma as discussed above.

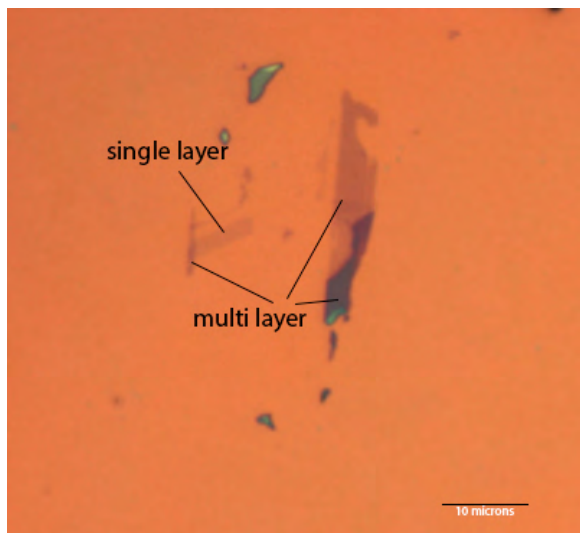


Figure 2.11: Single and few layer graphene flakes fabricated by mechanical exfoliation method on SiO₂/Si substrate which had pre-patterned alignment marks.

2.2.2 Graphene CVD growth and transfer method

As discussed above, the mechanical exfoliation technique is very slow and unpredictable. Also in this method, the resulting single layer graphene flakes, are typically few 10s of micron in size. However, chemical vapor deposition (CVD) technique can grow large sheets of single layer graphene, and the process is fast, reliable and scalable. The main disadvantage of the CVD method is the usually poor quality of the resulting graphene. CVD graphene is created from single crystal domains with different orientations that are patched together, and thus, it has a polycrystalline structure.

The first successful attempt to grow CVD graphene has been made in Ruoff group in 2009 [22]. In CVD mechanism hydrocarbon molecules from the precursor (i.e. methane CH₄) are absorbed on the substrate surface (i.e. copper). The substrate temperature is maintained at a level, which is high enough to break the hydrocarbon bonds, but at the same time, does not melt the substrate. Since copper has very low carbon solubility at this temperature, carbon atoms, broken from the precursor, are insoluble in the copper, and thus, graphitize on the surface.

Likewise, other transition metals have been used as catalysts to grow graphene. For example, CVD growth of graphene on Ni films results in few or many layer graphene sheets. This is mainly due to the higher solubility of carbon atoms in Ni films.

I followed the process that was developed by William Regan, a fellow Zettl group colleague, for graphene CVD growth and transfer. I also experimented with lower pressure in the graphene growth process, in order to get larger single crystal domains.

Figure 2.12 shows the carbon CVD system that I used for growing graphene. And Figure 2.13 is a schematic of the setup [22].

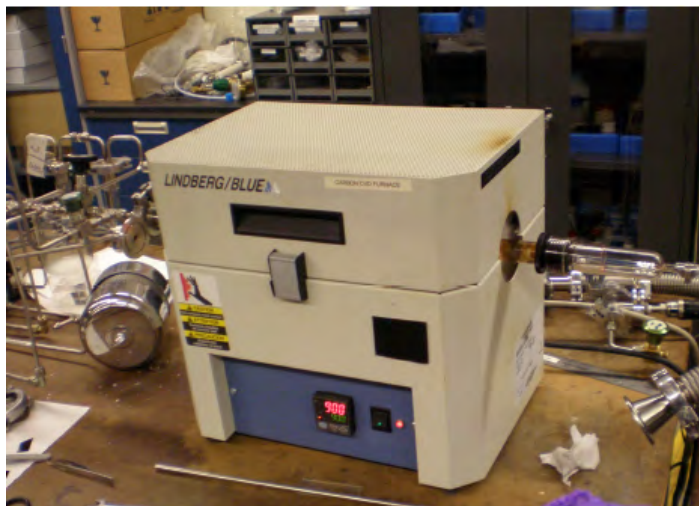


Figure 2.12: A picture of the carbon CVD system used for graphene and carbon nanotube synthesis. The substrate sits inside a quartz tube in a furnace; The precursor gas flows enter the quartz tube through stainless steel lines on the left, and exit to a vacuum pump on the right [23].

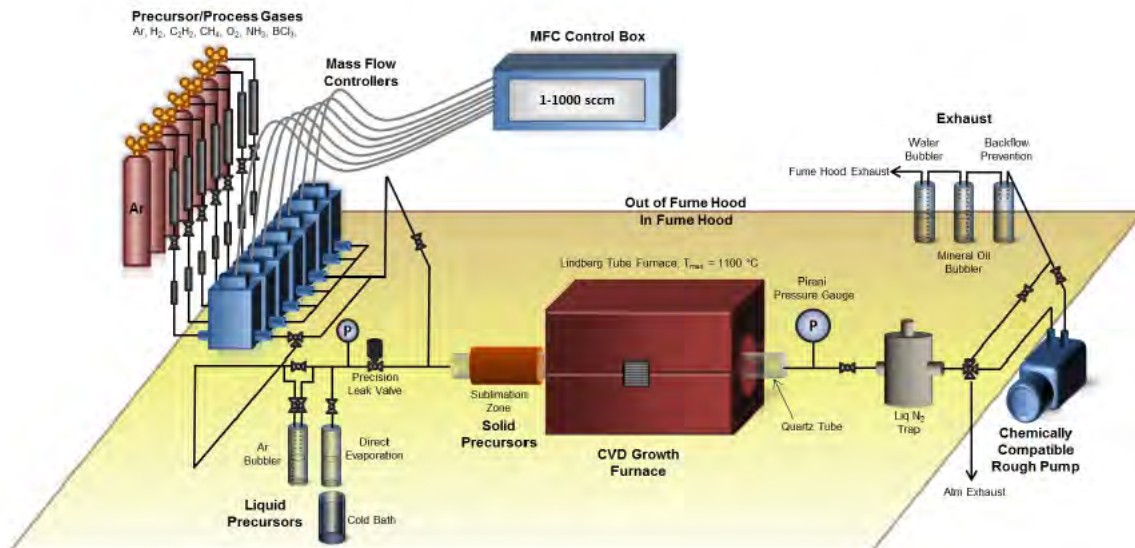


Figure 2.13: A schematic of the CVD system for graphene and hBN growth (This schematic is the courtesy of Kris Erickson) [24]

The process and parameters that I used to grow graphene is shown in Figure 2.14. I used methane gas as the hydrocarbon source, and a 25 μ m thick copper foil (Alfa Aesar No. 13382, 99.8%) as the catalyst.

I followed a three-step CVD growth process:

1. Annealing the copper foil at 1020°C in hydrogen for 20-30 minutes.
2. Growing with a low methane flow of 20 sccm for 5 minutes, to enlarge the single crystalline grains.
3. Growing with a high methane flow of 120 sccm for 5 minutes, to cover the entire copper surface, and form a uniform film.

When this process is complete, I opened the oven lid in order to cool down the sample to the room temperature rapidly. The hydrogen and methane flow was kept unchanged during the cooling step.

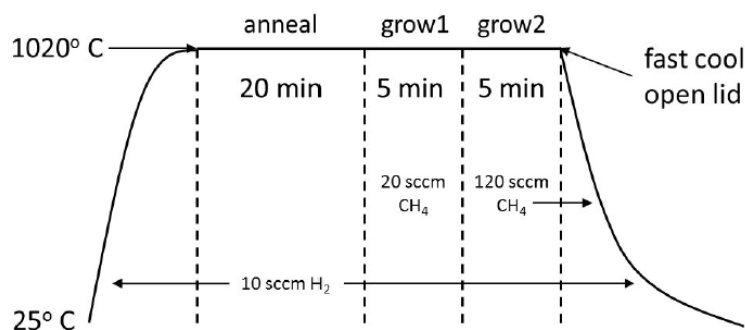


Figure 2.14: The CVD method used to grow graphene. The sample temperature was ramped up to 1020°C in 120sccm of hydrogen flow. Next, a 5 minutes slow growth with a 20sccm flow of methane, and a 5 minutes rapid growth with a 120sccm flow of methane were followed. Finally, the sample was rapidly cooled down to room temperature. [23]

The resulting graphene sheets, grown with this method, had of a few tens of μ m single crystalline grain size. Also, they covered the entire copper foil. After CVD growth, the copper foil became shinier, as shown in Figure 2.15.

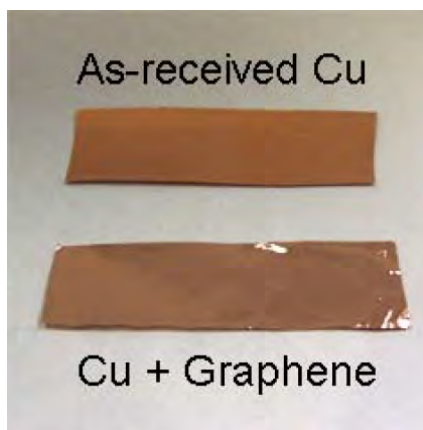


Figure 2.15: Comparison between a copper foil before and after graphene CVD growth [23].

The next step was to etch the growth catalyst (i.e. copper foil), in order to transfer the graphene sheet to another substrate. First, the copper foil, covered with the graphene film, was coated with a thin layer of a particular polymer. Then, the sample was floated on surface a copper etchant solution, which dissolves the copper from the bottom, and thus, leaves the graphene side intact. When the entire copper film was etched, the remaining graphene-polymer film was scooped out, on the target substrate. The final substrate, containing the graphene-polymer film, was slowly dried at 60 °C on a hotplate. Finally, the polymer was dissolved in acetone, and the sample was annealed in hydrogen at 300 °C to remove any polymer residue.

I used PMMA (Polymethyl methacrylate) as the transferring polymer. I experimented with two types of PMMA: A4 and A2, which are 4% and 2% weight solution in anisole, respectively. I used the spin coater at the Zettl lab, and the Headway spinners at Marvel Nanolab facilities. The polymer thickness is mainly a function of the polymer solution concentration, and the spin coating speed. The thickness of different PMMA concentrations as a function of spin speed is shown in Figure 2.16 [25].

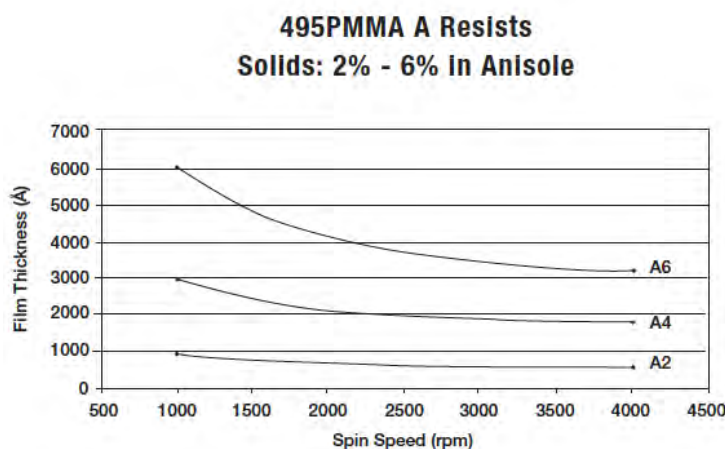


Figure 2.16: Film thickness versus spin speed, for different PMMA solutions. This data is provided in MicroChem PMMA datasheet [25]. I had similar thickness results.

Choosing the right polymer thickness is a trade-off between being able to easily see the floating graphene-polymer film on the etching liquid, and the remaining polymer residue on the final sample. On the one hand, when the PMMA film was too thin, after etching the copper, it was difficult to find and scoop out the practically transparent graphene-PMMA film. On the other hand, coating with a thick PMMA film resulted in a final graphene sample with lots of residue. Acetone and hydrogen annealing could not remove this amount of residue. Coating the sample with PMMA A2 at 3000 rpm, was found to result in a moderately visible graphene-PMMA film, and a clean final result.

Two commonly used etching solutions for copper are ferric chloride (FeCl_3) and sodium persulfate ($\text{Na}_2(\text{SO}_4)_2$). For an equal weight concentration, sodium persulfate etches the copper slower, and thus, more uniform than ferric chloride. Therefore, I used sodium persulfate as the etchant, and the etching process took a few hours at room temperature.

Scooping out the floating graphene-PMMA layers required practice and patience. For the etching solution, I used beakers that are deep enough for the scooping substrate, to easily fit under the graphene-PMMA film. I transferred the graphene-PMMA layers to another beaker containing clean DI water. I repeated this step two more times to remove any residue from the etching solution. Then, using the same method, the graphene-PMMA film was transferred to the final substrate.

I kept the substrate, containing the graphene-PMMA film on a hot plate at 60 °C overnight. This slow drying process ensures a good adhesion between the graphene sheet and the substrate. Next, In order to remove the PMMA layer, I submerged the sample in an acetone solution for 30 minutes. Then, the sample was rinsed in IPA, and blow-dried in nitrogen. Finally, using a tube furnace with a 50sccm hydrogen flow, the sample was annealed for 30 minutes. I used optical microscope and Raman spectroscopy, in order to verify the success of graphene transfer.

2.2.3 Device fabrication

The goal of this project was to study the effect of periodic potentials on the electronic transport of graphene. Several fabrication processes was considered in order to achieve this structure. Here, I discuss the main methods that I pursued, and their advantages and disadvantages.

Sub 15nm electron beam lithography

I will describe this method in more details in this manuscript. The main challenge in this technique was to lift-off and resolve smaller than 20nm features. Figure 2.17 shows a schematic of the final device fabricated with e-beam lithography.

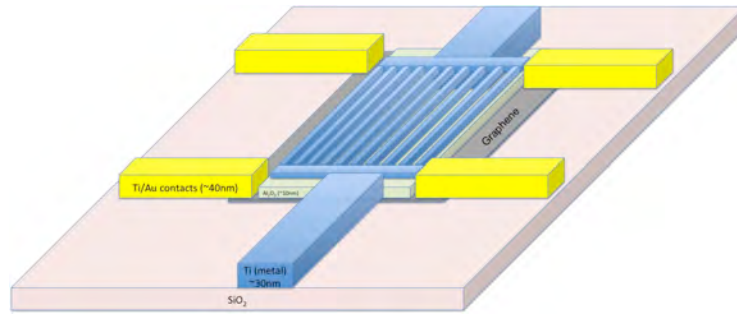


Figure 2.17: Schematic of a graphene device with a periodic potential. E-beam lithography technique was used to fabricate this device.

Thin Film stacking

This method will also be discussed in detail. In this method, an e-beam lithography step on the side of a silicon wafer (approximately 500μm thickness) was required. Figure 2.18 shows a stack of metal-oxide layers. The graphene device was fabricated on the side of this structure.



Figure 2.18: A multilayer metal-oxide stack. A graphene sheet was transferred on a side of this structure, and metal contacts were patterned.

Direct writing on graphene with TEM

From unclean samples and/or sample holders, carbohydrate residue remains in Transmission Electron Microscope (TEM) chambers. This carbohydrate residue can be used as "ink" for writing on a transparent substrate, like graphene. A former post-doctoral fellow at the Zettl group, Dr. Jannik Meyer, has showed that a properly focused electron beam, can break the hydrocarbon bonds, and deposit an amorphous carbon film on the substrate [26]. The resolution of this direct writing technique is extremely high, and below 1nm resolution has been achieved. The idea was to use this technique to pattern the desired periodic potential on graphene.

After refining and debugging the computer code, written by Dr. Meyer, and fine-tuning the TEM² alignments, I was able to reproduce and enhance previous results. The developed computer program in C++ language, converted an 8-bit TIFF input image to a file, containing a series of commands to control the TEM's beam position and dwell time. The C++ code is shown in Figure 2.19, and a typical output file is shown in Figure 2.20.

I was able to get 1nm resolution with this technique. Figure 2.21 (a) shows three lines, each smaller than 1nm wide, written on a graphene sheet in a TEM chamber. Figure 2.21 (b) is the initial TIFF image pattern.

The main challenge in this approach was to pattern the electrical contacts in order to measure the transport properties. This technique needed a TEM transparent layer, and therefore, the graphene sheet had to be suspended on a TEM grid (i.e. Quantifoil). Thus, no supporting substrate for the fabrication of electrical pads existed. Furthermore, the periodic potential was originated from the deposited amorphous carbon, which was a conductor, and had a significant affect the electrical properties of graphene. Also, in this approach, the potential barrier as fixed. Due to the mentioned shortcomings, we decided not to pursue this method.

² I used the Joel Transmission Electron Microscopy machine at Zettl group.

```

//////////
//compile: g++ main.cpp diff TIFF.cpp -Wno-deprecated -ltiff

#include "diff TIFF.h"
#include <iostream>
#include <stdio.h>
#include <math.h>
#include <cstdlib>

using namespace std;

int main(int argc, char **argv)
{
    if (argc!=2)
    {
        cerr<<"Usage: "<<argv[0]<<" infile.tif "<<endl;
        exit(3);
    }

    diff TIFF* pattern=new diff TIFF(argv[1]);

    pattern->tiffout("verify.tif");

    //get min, max
    int min=65536;
    int max=0;
    for (int x=0; x<pattern->width; x++)
        for (int y=0; y<pattern->length; y++)
        {
            int val=pattern->safeget(x,y);
            if (val<min) min=val;
            if (val>max) max=val;
        }

    cout<<"Min value: "<<min<<endl;
    cout<<"Max value: "<<max<<endl;
    cout<<"Enter exposure time corresponding to (max-min) value, in seconds: "
        <<endl;
    float expmax;
    cin>>expmax;
    cout<<"Enter pixel step size: "
        <<endl;
    int stp;
    cin>>stp;

    FILE* scanlist=fopen("scanfile.s", "w");

    int ox=0;
    int oy=0;
    int dx,dy;
    float time=0;
    float time2=0;

    fprintf(scanlist,"number stepsize = %i\n",stp);
    fprintf(scanlist,"number dose = %f\n",expmax/((float)(max-min)));
    fprintf(scanlist,"number shifttime = 0.257\n\n");

    for (int x=0; x<pattern->width; x++)
        for (int y=0; y<pattern->length; y++)
        {
            int value=((int)(pattern->safeget(x,y)-min));
            time+=value;
        }

    for (int x=0; x<pattern->width; x++)
    {
        for (int y=0; y<pattern->length; y++)
        {
            int value=((int)(pattern->safeget(x,y)-min));
            if (value>0)
            {
                dx=x-ox;
                dy=y-oy;
                ox=x;
                oy=y;
                fprintf(scanlist,
                    "EMBeamShift(%i*stepsize,%i*stepsize)\n",dx,dy);
                fprintf(scanlist,"sleep(dose*%i-shifttime)\n",value);
                time2+=value;
            }
        }
        //check whether Esc was pressed at the end of each line
        fprintf(scanlist,"if (GetKey()==27)\n\nbreak\n\n");
        fprintf(scanlist,"openandsetprogresswindow(\"Writing line %i of %i\", \"%i / %i done\", \"Esc to stop\")\n",
            x+1,pattern->width, ((int)(time2*expmax/((float)(max-min)))),
            ((int)(time*expmax/((float)(max-min)))));
    }

    //move beam away from final point to avoid a big black blob at the end
    dx=ox/4;
    dy=oy/4;
    fprintf(scanlist,
        "EMBeamShift(%i*stepsize,%i*stepsize)\n",dx,dy);

    fclose(scanlist);

    cout<<"Estimated write time: "<<time*expmax/((float)(max-min))<<" seconds"<<endl;

    return 0;
}

```

Figure 2.19: The computer program written in C++ language, that converts an 8-bit TIFF image to a list of commands for TEM machine.

```

number stepsize = 15
number dose = 0.000153
number shifttime = 0.257

if(GetKey()==27)
{
break
}
openandsetprogresswindow("Writing line 1 of 7","0 / 159 done","Esc to stop")
EMBeamShift(1*stepsize,1*stepsize)
sleep(dose*65535-shifttime)
EMBeamShift(0*stepsize,1*stepsize)
sleep(dose*65533-shifttime)
EMBeamShift(0*stepsize,1*stepsize)
sleep(dose*65535-shifttime)
EMBeamShift(0*stepsize,1*stepsize)
sleep(dose*65533-shifttime)
EMBeamShift(0*stepsize,1*stepsize)
sleep(dose*65535-shifttime)
if(GetKey()==27)
{
break
}
openandsetprogresswindow("Writing line 2 of 7","49 / 159 done","Esc to stop")
if(GetKey()==27)
{
break
}
openandsetprogresswindow("Writing line 3 of 7","49 / 159 done","Esc to stop")
EMBeamShift(2*stepsize,-4*stepsize)
sleep(dose*65535-shifttime)
EMBeamShift(0*stepsize,1*stepsize)
sleep(dose*65533-shifttime)
EMBeamShift(0*stepsize,1*stepsize)
sleep(dose*65535-shifttime)
EMBeamShift(0*stepsize,1*stepsize)
sleep(dose*65533-shifttime)
EMBeamShift(0*stepsize,1*stepsize)
sleep(dose*65535-shifttime)
if(GetKey()==27)
{
break
}
openandsetprogresswindow("Writing line 4 of 7","99 / 159 done","Esc to stop")
if(GetKey()==27)
{
break
}
openandsetprogresswindow("Writing line 5 of 7","99 / 159 done","Esc to stop")
EMBeamShift(2*stepsize,-4*stepsize)
sleep(dose*65535-shifttime)
EMBeamShift(0*stepsize,1*stepsize)
sleep(dose*65533-shifttime)
EMBeamShift(0*stepsize,1*stepsize)
sleep(dose*65535-shifttime)
EMBeamShift(0*stepsize,1*stepsize)
sleep(dose*65533-shifttime)
EMBeamShift(0*stepsize,1*stepsize)
sleep(dose*65535-shifttime)
if(GetKey()==27)
{
break
}
openandsetprogresswindow("Writing line 6 of 7","149 / 159 done","Esc to stop")
EMBeamShift(1*stepsize,-5*stepsize)
sleep(dose*65533-shifttime)
if(GetKey()==27)
{
break
}
openandsetprogresswindow("Writing line 7 of 7","159 / 159 done","Esc to stop")
EMBeamShift(1*stepsize,0*stepsize)

```

Figure 2.20: A typical output file from the written C++ program. By loading this file, with a .js extension, the TEM software could control the position and dwell time of the beam [26].

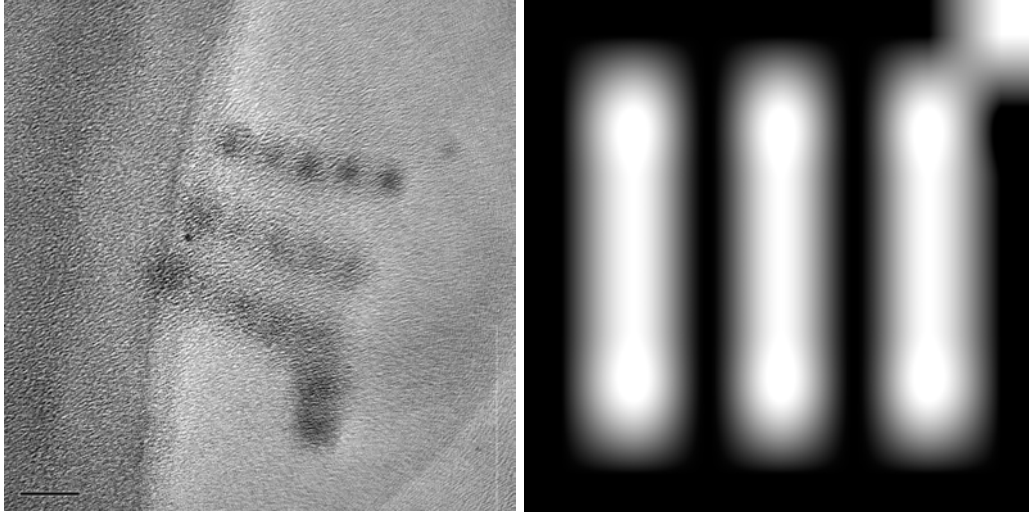


Figure 2.21: (a) Three straight lines written by direct writing in the TEM chamber. The width of each line is around 1nm. The scale bar is 2nm. (b) The 8-bit starting image file for this pattern. The written computer program converted this image to a series of commands, readable by the TEM software.

Focus Ion Beam (FIB) technique

Focused Ion Beam (FIB) is a microscopy technique, which can also be utilized for etching or deposition. In the etching mode, energetic heavy ions bombard a thin film to create a trench. Except, the smallest feature size that has been achieved with this technique is 65nm [26], which is far larger than the required feature size in this project.

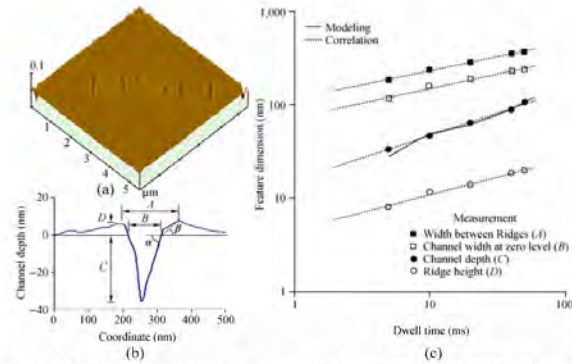


Figure 14.5 'ASU' nanochannel pattern on gold layer milled by 90 keV As^{2+} FIB: (a) AFM image at 5-ms dwell time, (b) channel cross-section and feature definition, (c) feature measurements for various dwell times

Figure 2.22: A nanochannel, etched into a gold thin film, using FIB technique. The trench width is approximately 65nm [26].

In the deposition mode, a small amount of metal (i.e. platinum), in the form of an organic gas, can be introduced in a FIB chamber. Thin metal lines can be formed by focusing the beam on a substrate, and thus, locally decompose the metal-containing gas.

Natural one-dimensional materials, like NbSe₃ or Hollandite crystals

Many natural crystals are known to have quasi one-dimensional structures. For example, Hollandite is a family of crystals, containing natural one-dimensional ionic wires. These crystals could potentially be employed, in a particular configuration, to apply a one-dimensional periodic potential on graphene.

However, in these natural materials, the distance between the conductive ionic wires is 5-10 Å, which is very close to the carbon-carbon distance in graphene. Therefore, this structure is not particularly suitable for the graphene-supperlattice experiment. However, because of the close match between these two fundamental distances, studying the graphene transport properties on Hollandite is an interesting separate experiment which worth pursuing. Figure 2.22 compares unit cell dimensions of Hollandite and graphene

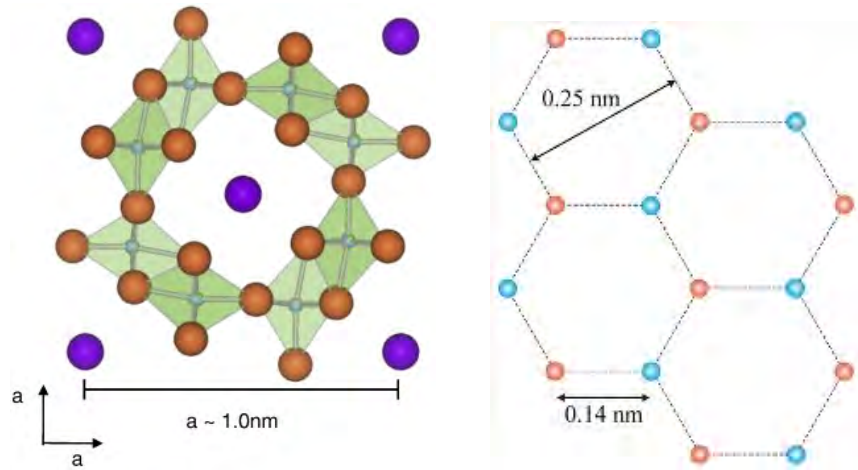


Figure 2.23: The dimension of a (a) Hollandite (b) graphene unit cell. This fundamental dimension is close in these two structures.

I thoroughly studied all the discussed fabrication options, and as a result, the first two methods (sub 15nm e-beam lithography and thin film stack) were experimented. These two methods are discussed in more details.

2.2.4 Sub 15nm electron beam lithography

In the theoretical study of the effect of periodic potential on graphene, the fundamental periodicity below which the effect was experimentally measurable was estimated to be 10-20nm. The modeling and simulation results suggested that the effect is negligible in larger superlattices. However, the highest e-beam resolution accessible with the SEM equipment in the Zettl lab³ was around 50nm.

Therefore, I improved the resolution of the e-beam lithography technique in the Zettl lab, by further aligning the electron-beam, depositing a thinner e-beam resist, and finding the optimized exposure dose. However, some parameters were not tunable. For example,

³ This SEM is equipped with Nanometer Pattern Generation System (NPGS) for electron beam and ion beam lithography.

in that particular SEM machine, the maximum accelerating voltage was 30kV, which was not sufficient for high-resolution e-beam lithography. Essentially, lower accelerating voltage means less energetic electrons. Therefore, in order to fully expose the e-beam resist, the area dose (or dwell time) of the beam had to be set higher, which significantly reduced the resolution. Furthermore, the minimum beam size in this particular SEM machine was around 10nm, which was too large for achieving features smaller than 20nm.

Due to all these limitations, I decided to use the e-beam lithography equipment at the Marvell Nanolab Facilities. The e-beam lithography machine in the Nanolab is a Crestec CABL-9510CC Electron Beam Lithography System, with a 50kV accelerating voltage. This machine is specifically designed for high-resolution e-beam lithography, with a nominal resolution of 10nm.

Several types of e-beam resists are commercially available. Generally, for lift-off purposes, positive-tone e-beam resists are used. In a positive-tone resist, the exposed sections of the resist dissolve in the developing solvent. For etching and other applications, negative-tone resist are more common. Some commercially available e-beam resists include:

Positive-tone:

- Polymethyl methacrylate (PMMA): This material can be purchased under MicroChem 950PMMA and MicroChem 495PMMA names. Numbers show the polymer's molecular weight. This product is available in different concentrations and solutions.
- ZEP520A: This is a relatively new e-beam resist, which is available through Zeon Chemical Corp. This resist is capable of resolving very small features. However, the main advantage of ZEP over PMMA is in its superior resistance in various etchant environments, including plasma. This high etching resistance makes ZEP, a suitable option for the processes that involve etching or acidic environment. Figure 2.24 shows an e-beam dose test experiment on a ZEP e-beam resist layer.

Negative-tone:

- SU-8: This is an epoxy-based negative photoresist. Even though, SU-8 is very sensitive to the electron-beam, however, it does not result in high-resolution structures. I could repeatedly achieve 100nm feature size on SU-8.
- XR-1541 (HSQ, hydrogen silsequioxane): This is a high-resolution negative-tone e-beam resist, which is available through Dow Corning®. I was able to repeatedly achieve 10nm feature size with this resist.

There is also a class of co-polymers that is used to enhance the lift-off process. The most well known resist in this category, is MicroChem MMA. However, when trying to achieve the smallest possible feature size, these co-polymers tend to drastically reduce the resolution. Therefore, I avoided using them when fabricating very small structures.

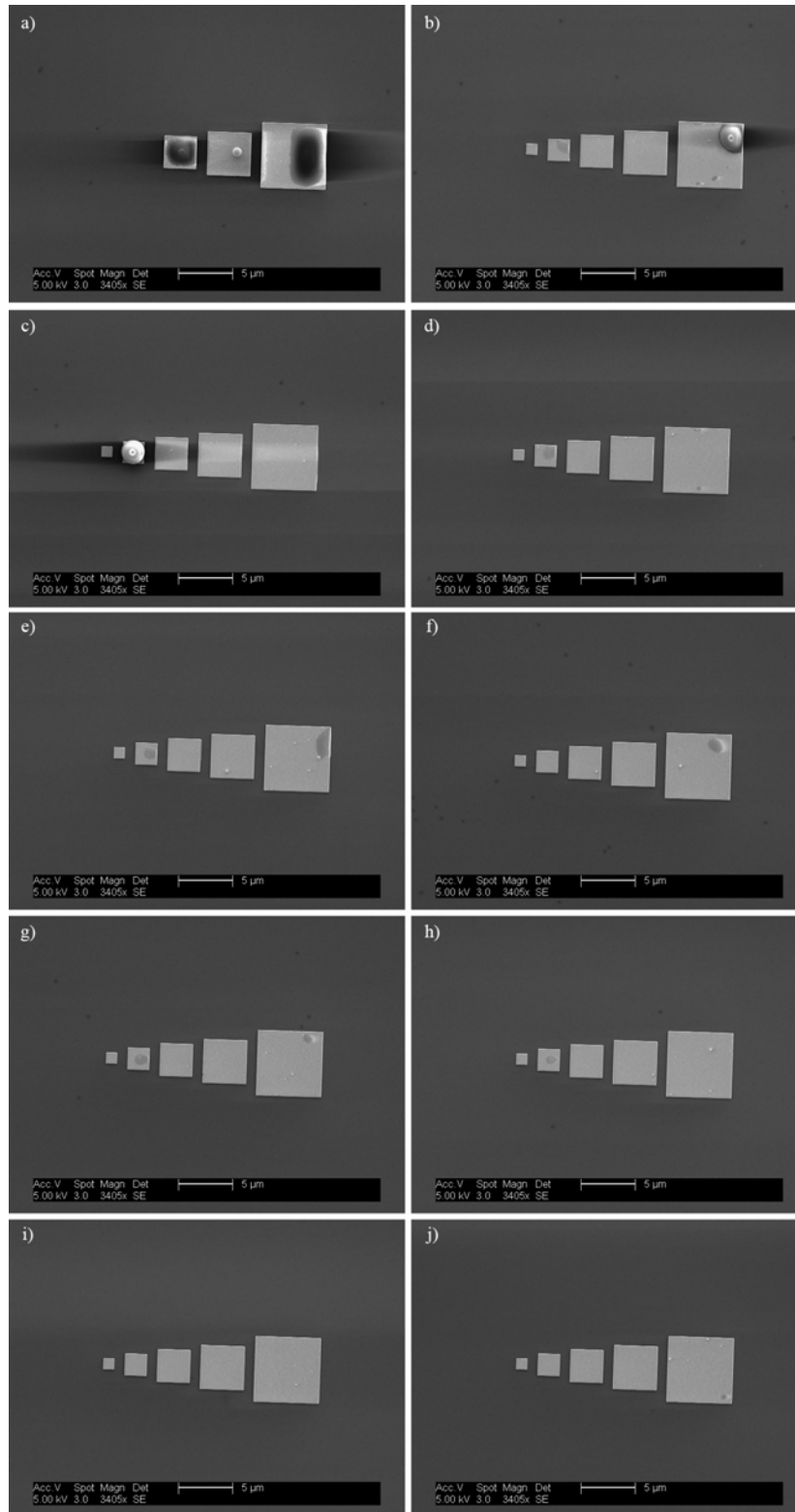


Figure 2.24: Dose test experiment of ZEP-520A e-beam resist by Crestec machine. (a) $150 \mu\text{C}/\text{cm}^2$, (b) $180 \mu\text{C}$, (c) $210 \mu\text{C}$, (d) $240 \mu\text{C}$, (e) $270 \mu\text{C}$, (f) $300 \mu\text{C}$, (g) $330 \mu\text{C}$, (h) $360 \mu\text{C}$, (i) $390 \mu\text{C}$ and (j) $420 \mu\text{C}$.

Here, I describe lithography processes, with which I achieved the best resolution using SEM and Crestec machines, located in the Zettl lab and the Nanolab, respectively. It is worth mentioning that, in order to obtain the highest possible resolution, the resist thickness had to be kept minimum. The trade-off is that, the lift-off of thicker metal layers is not possible.

E-beam lithography with FEI SEM XL 3000 equipped with Nanometer Pattern Generation System (NPGS)

This SEM machine, which is shown in Figure 2.25, is located in LeConte Hall 87. In addition to NPGS, this SEM machine is also equipped with an Electron Diffraction Spectroscopy (EDX), and a Nano-scaled Mechanical Manipulation (Attocube Stage) system.



Figure 2.25: FEI-SEM XL 3000 system located at 87 Birge Hall. This machine is equipped with a NPGS system for e-beam lithography.

Figure 2.26 shows E-beam lithography steps. These steps are described in detail below:

Cleaning the substrate

I used acetone and IPA as cleaning agents, and nitrogen blow for drying.

Coating the e-beam resist

In order to achieve the highest possible resolution, I used 950PMMA A2 (2% weight in anisole). I used the spinner machine in Birge Hall 129. The coating process was performed at 4000 rpm, and the resulting film was 40-50nm in thickness. In order to enhance the lift-off step, I often spun a MMA EL 6 (6% weight in ethyl lactate) layer at 4000rpm, under the PMMA resist. I baked the MMA at 150°C for 30 seconds, before spinning the PMMA. The overall thickness of the resulting MMA-PMMA bi-layer was 120-150nm.

Pre-bake

The spin coating step was followed by a 15 minute bake on hot plate at 180°C.

Depositing gold nanoparticles for focusing purposes

If the substrate is fully clean, the coated resist surface becomes completely flat and feature-less, which is required to achieve the best possible resolution. However, it is extremely difficult to focus on the surface of a flat film of e-beam resist. Since a perfect beam focus is essential in high-resolution e-beam lithography, while the sample was on the hot place, I manually dropped cast a small amount of a solution containing gold nanoparticles (Sigma Aldrich, Gold Nanoparticles, 10nm diameters in IPA) on the substrate corners. Subsequently, the resulting gold nanoparticles were used as focusing features.

Beam alignment and measurement

Perfect alignment of the beam is critical in achieving high-resolution lithography. Specifically, lens misalignments and stigmations have to be minimized. When perfectly aligned, the beam has the minimum size, and it is perfectly circular in shape. Next, I measured the beam current by magnifying the beam into a faraday cup, which collects all electrons in the beam. I repeated this procedure for all spot sizes. I normally used spot size 1 for the smallest features (100nm or less), spot size 3 for few-micron size features (5µm or less), and spot size 5 for large features, like contact pads. The typical current value for spot size 1 was 30pA.

Spot	Spacing	Area Dose
Spot 1	15nm	350 µC/cm ²
Spot 3	50nm	400 µC/cm ²
Spot 5	100nm	400 µC/cm ²

Table 2.1: The optimum value of area dose and line spacing, the two key parameters in the NPGS e-beam lithography process. These parameters are adjusted for the SEM machine in the Zettl group.

NPGS setup and writing

The NPGS software took a DesignCAD file, containing the desired pattern, and accordingly, sent commands to the SEM software. These commands controlled the beam shutter, beam deflection and the stage position. In order to align the new patterns with the previously made features, a picture of the sample can be incorporated in the DesignCAD file. Typically, I used a network of crosses as alignment marks. While setting up the NPGS software, I defined area that alignment marks were to be found, and their respective shapes. The NPGS searched the defined area for alignment marks, and automatically rotated and translated the whole design accordingly.

The two key parameters to set up, when writing patterns with the NPGS, are area, dose and spacing between exposures. Table 2.1 summarizes the optimum parameters for each spot size.

Before starting the NPGS program, I corrected the tilting error by manually focusing on four corners of the sample, using the deposited gold nanoparticles, and saving the resulting focusing information in the NPGS software. With this data, the NPGS software calculated the X-Y focus correction matrix. This step is critical, because without a perfect focus, high-resolution e-beam lithography is not possible.

Developing the exposed resist

I used a 1:3 mixture of MIBK-IPA, which is available for purchase from MicroChem. A 30 seconds soaking in this solution at room temperature was sufficient to completely develop the pattern.

Depositing the thin films

For a successful and clean lift-off step, the film thickness had to remain smaller than half of the resist thickness. On the MMA-PMMA bilayer resist, I usually deposited a 50-60nm thin film. The deposited films were Ti-Au or Cr-Au bilayers as metal contacts, or TiO₂-Ti as periodic potential.

Lift-off

Acetone is an effective solvent of PMMA and MMA. I usually immersed the sample in an acetone beaker and kept it overnight. Then, the sample was rinsed in acetone-IPA flow, and blew dry in nitrogen.

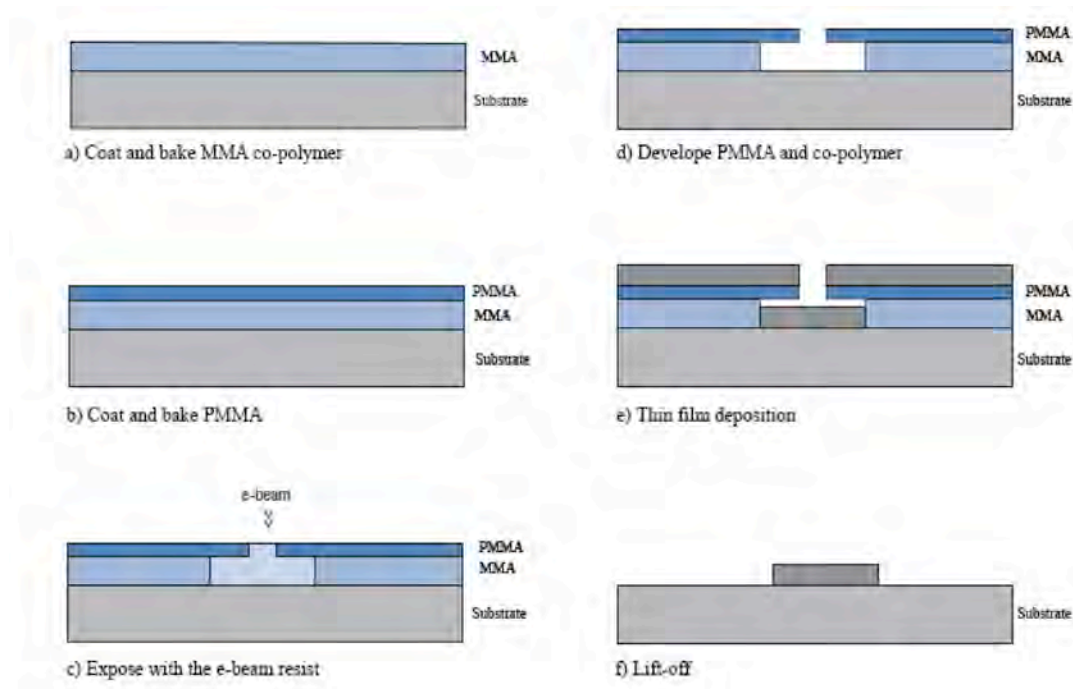


Figure 2.26: The e-beam lithography process for a MMA-PMMA bilayer resist.

E-beam lithography with Crestec CABL-9510CC Electron Beam Lithography System

This machine is located in the 3rd floor of the Marvell Nanolab Facilities, and is shown in Figure 2.27. Crestec is “a high precision e-beam lithography tool (writer) capable of resolving 10nm features” [28].



Figure 2.27: Crestec e-beam lithography machine, located in the UC Berkeley Marvel nanolab facilities. This machine is capable of resolving 10nm features [28].

The majority of e-beam lithography process with Crestec is similar to that of FEI SEM XL 3000:

Cleaning the substrate

As described above.

Coating the e-beam resist

I used Headway spinner machine to coat the substrate with PMMA or MMA. I used the following pre-programmed recipe:

1. First ramp: 500rpm to 4000rpm in 3 seconds
2. Main spin: 4000 rpm for 60 seconds

Also, I experimented with HSQ 2% negative-tone e-beam resist. I spun HSQ at 5000rpm for 60 seconds with no co-polymer layer.

Pre-bake

The pre-bake process for PMMA and MMA was similar to the one described above. However, I baked HSQ 2% for 4 minutes at 80 °C.

Depositing gold nanoparticles for focusing purposes

This step was not necessary in Crestec machine, because it was equipped with a built-in sample containing gold nanoparticles, which can be used to fine tune the stigmatism and focus.

Beam alignment and measurement

Crestec is equipped with a laser feedback system to compensate for X-Y focus misalignment. Perfect alignment of the beam could be verified, by focusing the beam on an arbitrary spot of the PMMA surface, and image the result after a few seconds; the mark left by the beam on the surface had to be a completely well-defined circular shape.

Crestec setup and writing

When the beam was properly aligned, I setup the software, by determining the beam current value, with which I wanted to write the patterns and the dwell time. For small features, I set the current at 50pA or 25pA. The dwell time was determined by performing several dose test experiments, to find the optimum condition for my experiment.

The alignment procedure in Crestec was performed with a joystick system, which was used to position the center of the each alignment mark, at the center of screen. The entire alignment process was performed twice.

Developing the exposed resist

The process for developing PMMA and MMA resists was similar to the one described above.

For developing HSQ resists, I used Tetramethylammonium hydroxide TMAH 25% solution in water. The samples were soaked in this solution for 30 seconds, and rinsed with DI water for 90 seconds, and followed by a blow dry in nitrogen.

Post-bake

PMMA and MMA layers do not need any post-bake treatment. However, I baked HSQ resists for 2 minutes at 120°C, in order to further enhance their physical structure, and increase their resistance in the plasma etch step.

Thin film deposition and lift-off processes were done as described previously.

2.2.5 Metal-Oxide multi-layer stack

I also experimented with other approaches in order to achieve a one-dimensional periodic potential, with the spatial period of ~10nm. One such approach was a multilayer stack of metal and oxide layers. A schematic of the process is shown in Figure 2.28. This fabrication process was conducted in collaboration with Dr. Jiyoung Chang, a post-doctoral fellow at Zettl group.

In this process, the graphene device was fabricated on the side of the stack structure, and the superlattice applied the desired one-dimensional potential on graphene. Key parameters in this fabrication procedure were the type of materials used in the stack, the number of layers, and the thickness of each layer.

Material

The main challenge was to choose a metal and oxide combination, which when stack up, had the minimum amount of stress. The stack made out of chromium and silicon dioxide combination showed a high amount of stress residue, which caused the entire stack to peel off. We also experimented with yttrium and titanium dioxide combination, and yttrium and silicon dioxide combination. These combinations showed high stress residue as well.

Figure 2.29 shows the intrinsic stress in chromium, iron, and titanium thin films as a function of thickness [29]. Titanium thin film is known to have a small amount of stress residue. Therefore, titanium and titanium dioxide combination was used in the multi-layer stack structure.

Film thickness

Practically, the metal and oxide layer thickness could be as thin as desired. However, for a periodic potential structure with a very small periodicity, the gate thickness (i.e. the space between the gate and graphene sheet) needed to be very small as well. A quick simulation showed that the thickness of the gate oxide had to be at least half of the distance between the metal layers, in order to have a significant charge separation on the graphene. In other words, for the charge concentration under metal layers to be twice as the charge concentration under oxide layers, the gate thickness had to remain very small. We were not able to grow a thinner than 5nm gate oxide, which had a low-leakage; therefore, the superlattice layer thickness was set to be twice that value, or 10nm.

Number of the layers

By consulting with Prof. Louie's group, who first proposed the theory of periodic potential effect on graphene, the number of layers was set to be more than 30 metal layers, or 60 layers total.

After fabricating the metal-oxide superlattice, and before transferring the graphene sheet a freshly cleaved surface was needed to expose. However, simply dicing the structure, was not an option, because it resulted it would blend the layers together. The best result was obtained by breaking the sample. In this method, first, using a diamond scribe, two deep marks on two far ends of the sample were created. Then, the sample was placed on a surface with small step, and by applying force on the floated part the sample was broken in half. The two resulting substrates have a smooth and well-defined metal-oxide superlattice on their cross section.

Before transferring the graphene sheet, the multi-layer stack had to become electrically separate from the graphene. Therefore, a thin oxide layer was deposited on the cross section. This oxide layer acted as the gate oxide.

At first, we experimented with a 5nm zirconium dioxide (ZrO_2) layer, deposited using Atomic Layer Deposition (ALD) technique. I used the ALD system at Prof. Javey's lab, and collaborated with Mahmut Tosun, a PhD student in that research group. However, the resulting ZrO_2 film showed large gate leakage. Next, yttrium oxide was tested. Several groups have been able to grow this material by oxidizing thin films of yttrium on hot plate. The resulting yttrium oxide films have shown to act as high quality gate oxides with low leakages []. We deposited a 2-3 nm yttrium film using e-beam evaporation technique, and then, oxidized it on a hot plate at 200 °C for one hour in air. The preliminary results of this approach were promising. However more experiments were needed to confirm the low gate leakage claim.

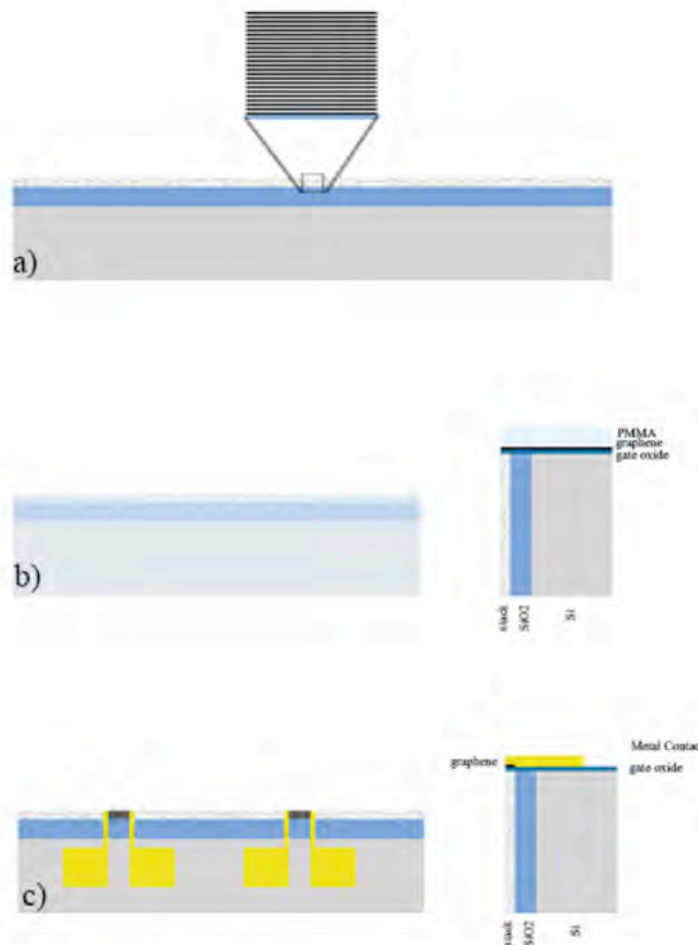


Figure 2.28: The fabrication process of a metal-oxide superlattice structure, and the graphene device. (a) A metal-oxide superlattice was fabricated by sequential deposition of metal and oxide films. (b) A graphene layer was transferred to the side of this superlattice structure. The superlattice applied the periodic potential. (c) Metal contacts were patterned on the graphene layer.

In order to successfully transfer graphene sheets on the narrow side, a long drying step was required, which ensured an adequate adhesion between the graphene layer and the gate oxide. Raman Spectroscopy was used to verify the successful transfer of graphene layer.

In order to pattern electrical contacts, the side of the substrate had to be coated with PMMA e-beam resist. However, standards spin coating on the narrow side of the silicon wafer was not possible. In order to overcome this issue, a PMMA layer, spun on another substrate (e.g. copper) was transferred on the side of the substrate. The transfer method was similar to graphene transfer described in section xxx, except no graphene layer was present between copper and PMMA. The transferred PMMA layer was flat, and uniform across the sample edges. Then, electrical contacts were fabricated using standard e-beam

lithography and lift-off techniques. Finally, The electrical properties of the device were measured in a cryogenic probe station.

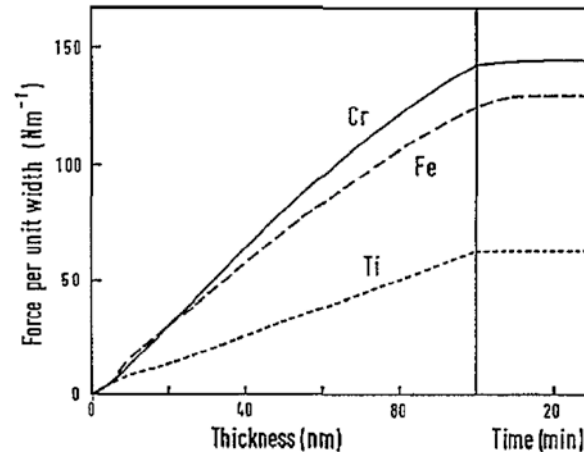


Figure 2.29: The intrinsic stress of chromium, iron and titanium thin films as a function of thickness [29].

2.3 Results and Discussion

2.3.1 Sub 15nm e-beam lithography

The first step of lithography was to deposit the large metal pads. A bilayer of titanium and gold, with 5nm and 45nm respective thicknesses, was patterned using the lift-off technique. Figure 2.29 shows Scanning Electron Microscopy (SEM) images of typical metal pad structures, which were made using the SEM machine equipped with the NPGS software at the Zettl lab. E-beam evaporation and lift-off processes were also conducted at the Zettl lab.

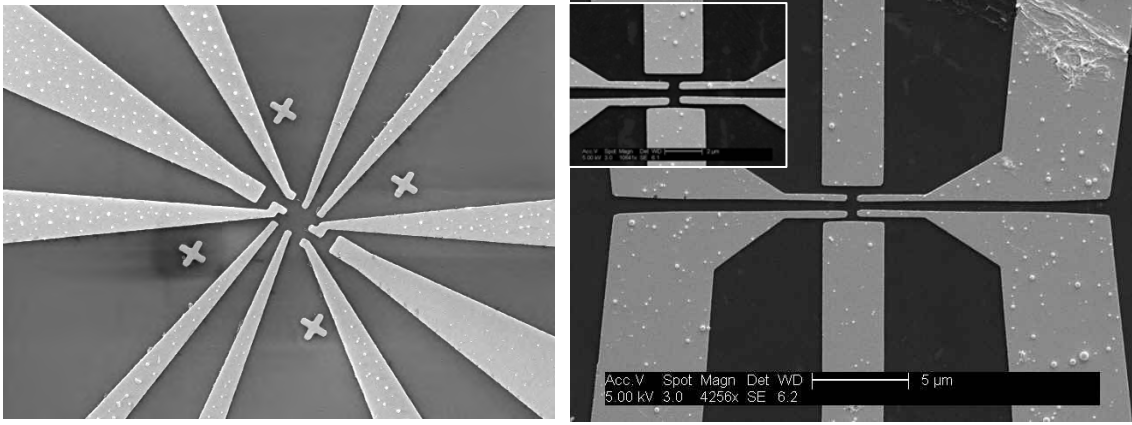


Figure 2.29: SEM micrograph showing the metal contact pads for two different graphene devices. After removing the graphene layer from unwanted areas, the periodic potential was fabricated at the center of the pads.

Figure 2.30 summarizes the four possible structures for a graphene superlattice device, fabricated by e-beam lithography techniques. Since dielectric constant of oxides (i.e. 80 for TiO_2 layers) were larger than air, among the four candidates, the device structure shown in Figure 2.30 (a) had the strongest charge modulation effect on graphene layer. Device structures shown in Figure 2.30 (b), (c), and (d), were easier to fabricate. However, due to the electric field expansion between the gate metal and the graphene layer, they show a significantly smaller modulation effect.

After fine-tuning the Crestec parameters thoroughly, and conducting several dose test experiments, I was able to obtain smaller than 15nm features on PMMA e-beam resists. However, in order to fabricate the desired periodic potential, a successful lift-off step of an oxide-metal bilayer was required. This bilayer was meant to act as the gate structure. Therefore, the key challenge in fabricating the oxide-metal bilayer device structure (Figure 2.30-a) was to resolve the sub 25nm features in the lift-off step. Figure 2.31 shows the lift-off result for 25nm and 15nm wide line structures. As shown in this image, no well-defined below-25nm structures could be fabricated with this technique.

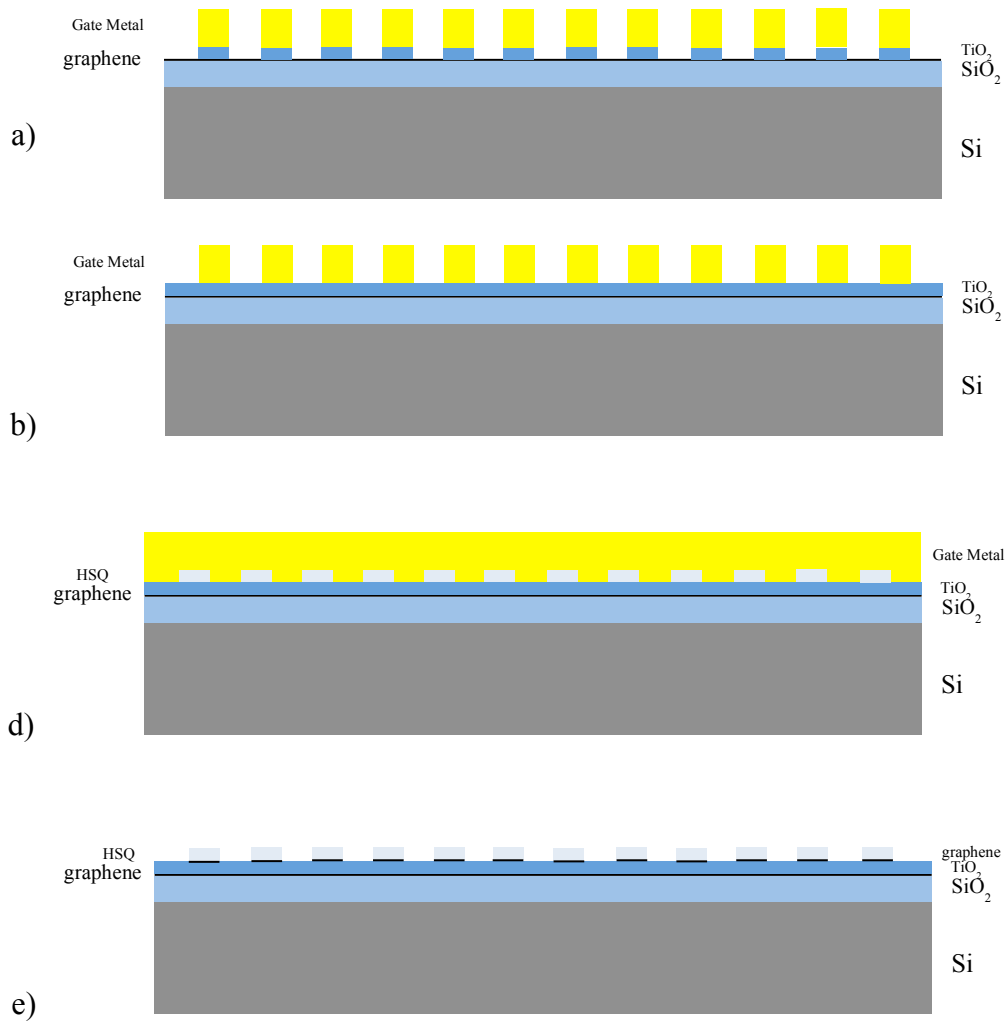


Figure 2.31: Four proposed structures for a graphene superlattice device. (a) Nanometer sized (10-15 nm wide) bi-layers of oxide-metal fabricated with a lift-off technique. (b) Metal fingers formed on a film of gate oxide. (c) HSQ fingers fabricated on a film of gate oxide and a thin film of metal covers the entire structure. The potential modulation comes from the difference in the effective dielectric constant of the regions with and without the HSQ fingers. (d) HSQ fingers acts as the etching mask to form fingers on a second graphene layer which is transferred on the gate oxide. The second graphene layer, provides the periodic potential for the other graphene layer underneath.

The device structure shown in Figure 2.30 (b) was easier to lift-off. In this process, first, the graphene layer was covered with a 3-5nm thick gate oxide using the ALD technique. Next, sub 20nm narrow metal lines were patterned on top of the oxide layer. However, since in this case, the surface underneath the e-beam resist is an insulating oxide, the resulting lithography resolution was degraded. Figure 2.32 shows 25nm, 20nm, and 15nm wide line, fabricated from titanium on a graphene sheet, covered with a 3nm aluminum oxide thin film. Therefore, no smaller than 20nm lines was achieved in this structure as well.

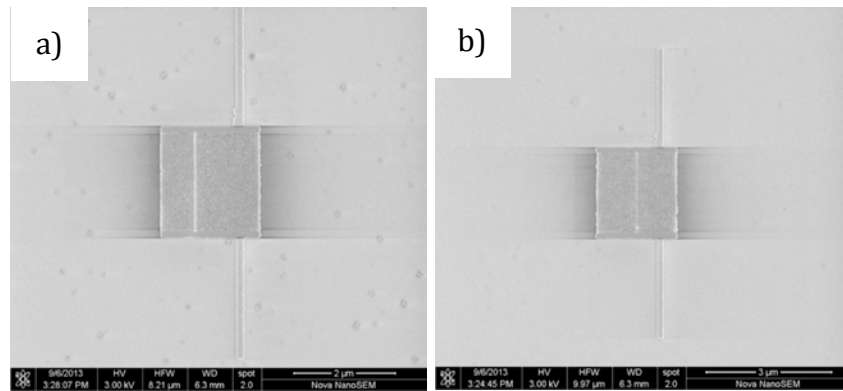


Figure 2.31: The lift-off results from a 30nm thick bi-layer of Cr-Au on a graphene sheet for (a) 25nm and (b) 15nm wide line structures.

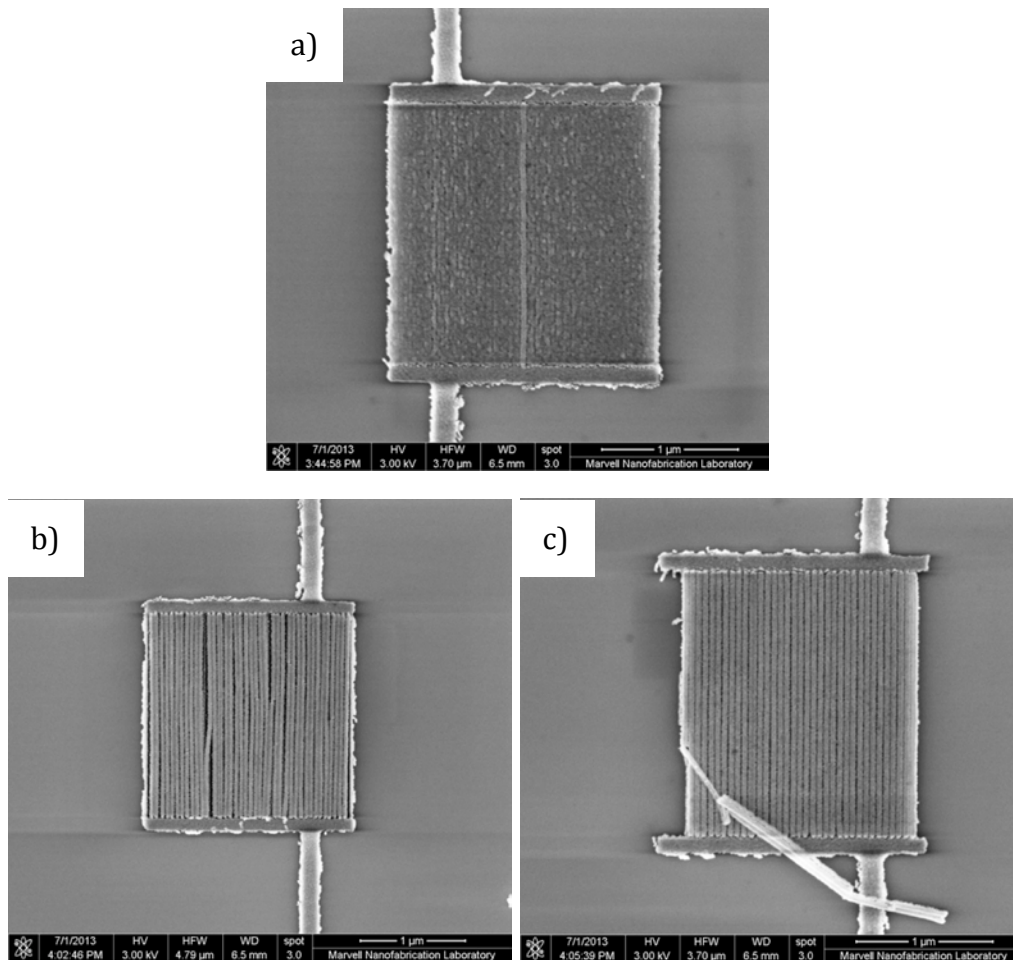


Figure 2.32: (a) 25nm, (b) 20nm and (c) 15nm wide line, fabricated from titanium, using lift-off technique. The substrate is a graphene sheet covered with a thin oxide film.

Figure 2.33 shows the SEM image of 25nm wide lines of HSQ 2% negative resist, patterned on a SiO₂ substrate, using the Crestec machine at the UC Berkeley Nanolab

facilities. For the optimum results, when the beam current was 50pA and 60000 dots per 60 μ m were exposed, the beam dwell time was tuned at 36 μ s. Figure 2.34 show results from the dose test experiment on HSQ 2% e-beam resist, using the Crestec machine.

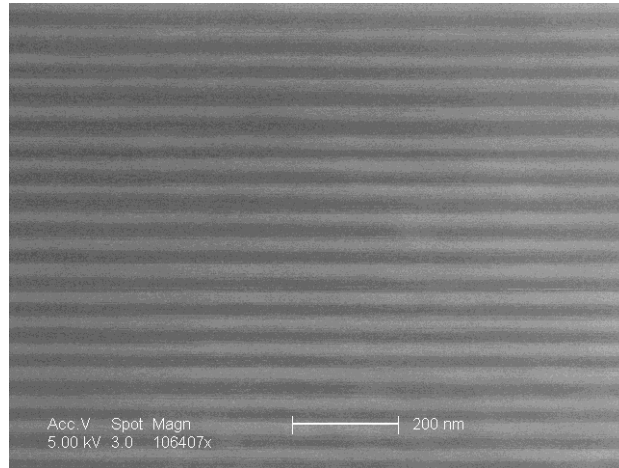


Figure 2.33. 15nm HSQ lines, written on a graphene sheet, using Crestec nanolithography tool at the UC Berkeley Nanolab facilities.

Finally, Figure 2.35 shows 15nm wide lines, patterned with HSQ on a graphene sheet. Due the excellent electrical conductivity of graphene, very high-resolution e-beam lithography was possible. Therefore, fabrication of sub-15nm lines of HSQ 2% on graphene layers was a proof of concept that the structure shown in Figure 2.30 (d) was

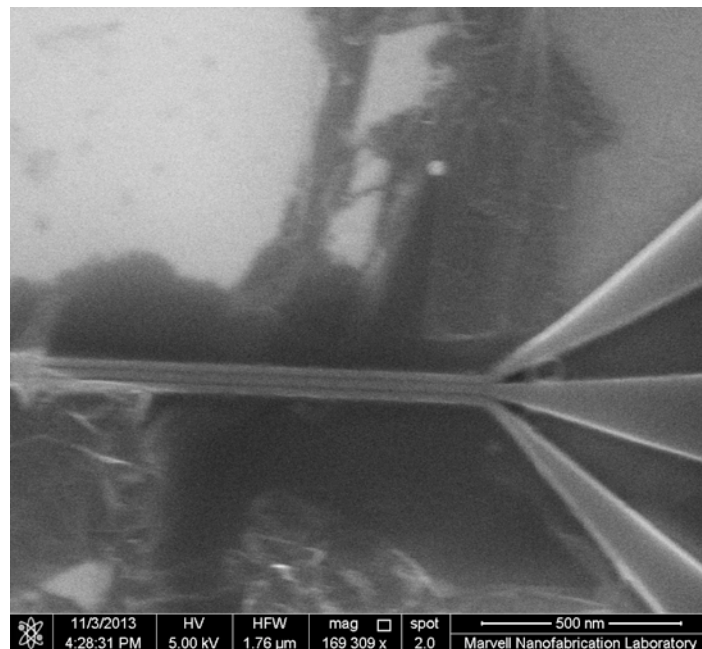


Figure 2.35: The SEM micrograph of 15nm lines of HSQ 2% on graphene using e-beam lithography technique.

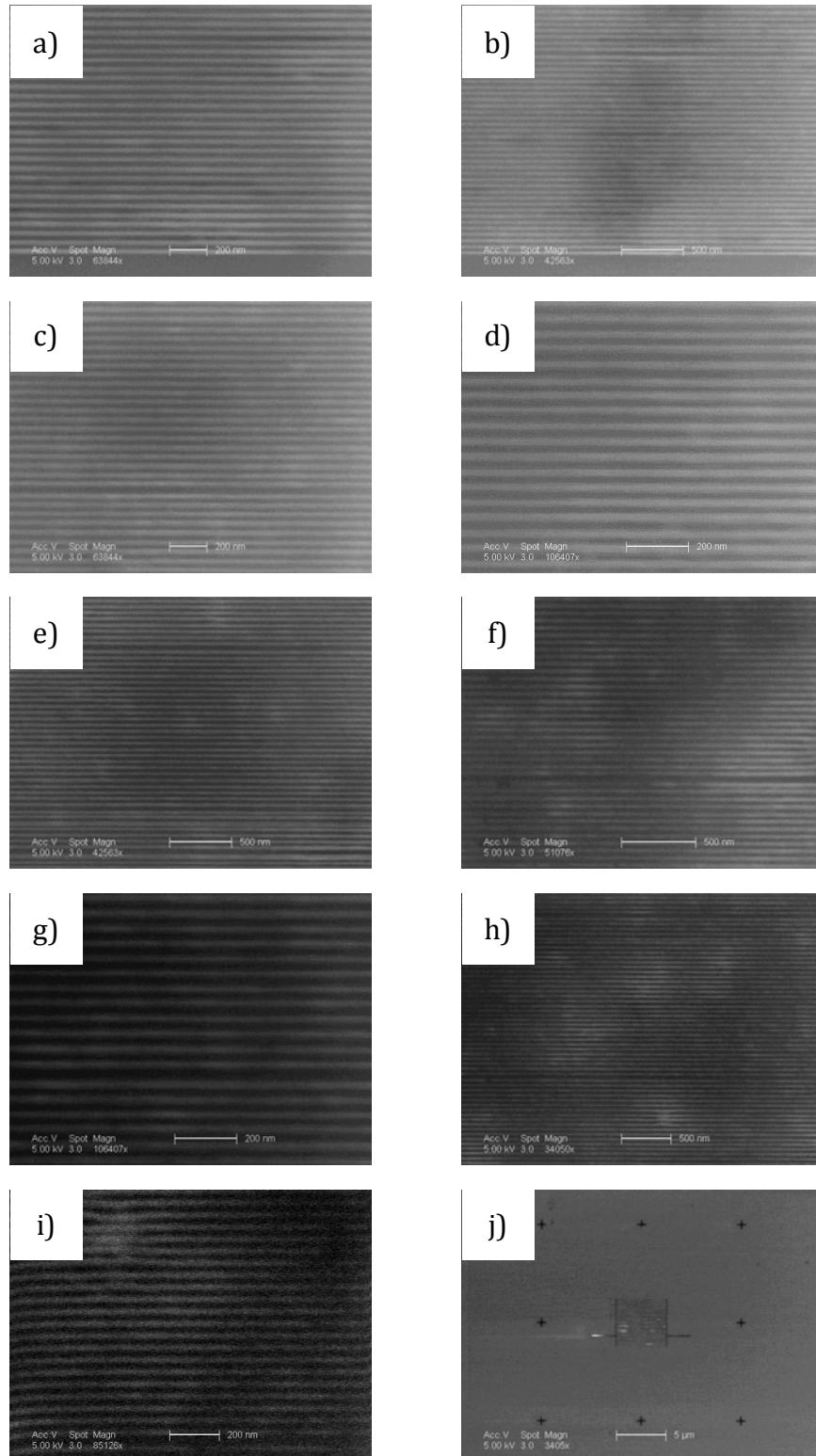


Figure 2.36: Dose test result on a HSQ 2% resist film, with 50 pA beam current using Crestec machine in the UC Berkeley Nanolab facilities. The images are of 20nm HSQ lines wirtten with 42 μ s (a), 40 μ s (b), 38 μ s (c), 36 μ s (d), 34 μ s (e), 32 μ s (f), 30 μ s (g), 28 μ s (h), 26 μ s (i), 24 μ s (j) dwell time.

The most reliable method that was used to verify a successful transfer of graphene single layers, and approximately measure their quality was Raman spectroscopy. Figure 2.36 shows a typical Raman spectrum, measured from a single layer graphene. The graphene layer was synthesized with the CVD method on copper foil, and was subsequently transferred to a SiO₂ substrate. In this measurement, the wavelength of Raman laser was 514nm. The larger peak is the 2D peak, which is located at 2680 cm⁻¹, and the smaller peak is the G peak, and it is located at 1585cm⁻¹. The G-peak height is nearly one third of the 2D peak height.

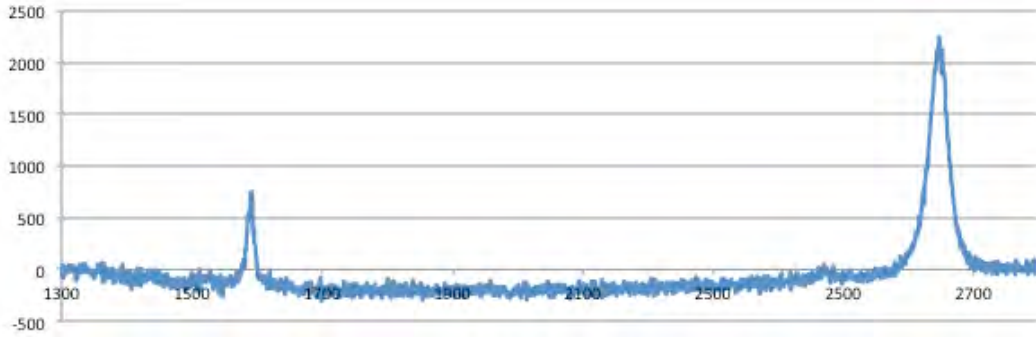


Figure 2.36: Raman spectrum of a single layer graphene, transferred on a Si-SiO₂ substrate. The spectrum was measured with a 514nm laser.

Figure 2.37 shows typical I_d versus V_g characteristics of a single layer graphene device at different V_d s. The measurement was performed before fabricating the potential superlattice, and at room temperature. The V shape I_d - V_g curve is the signature of graphene devices. The device has its maximum resistance ($\sim 350\text{K}\Omega$) at the Dirac point.

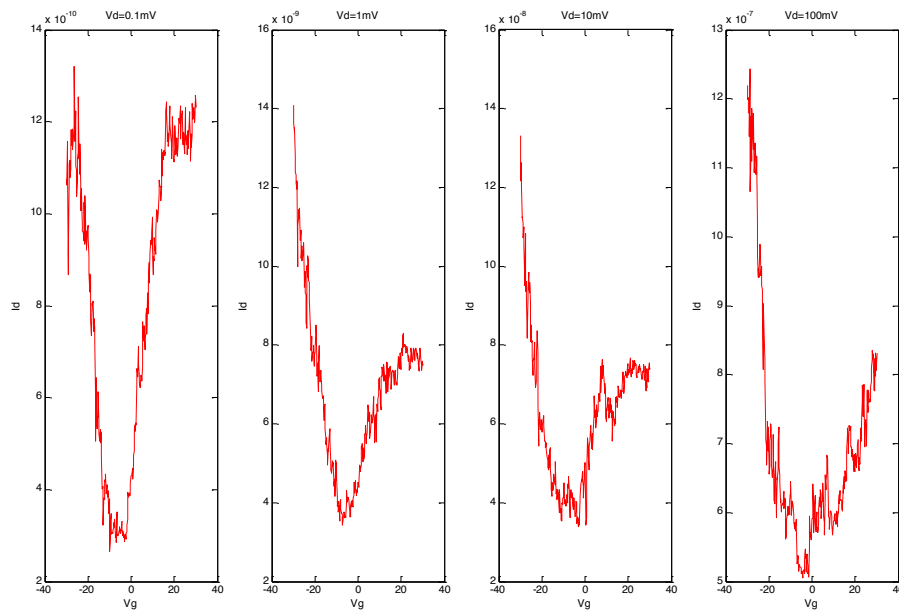


Figure 2.37: I_d versus V_g for a typical graphene device at room temperature, measured before fabricating the potential superlattice.

2.3.2 Metal-Oxide multilayer stack system

All experiments in this section were performed in collaboration with Dr. Jiyoung Chang.

Figure 2.39 displays the cross section SEM image of a metal-oxide superlattice, fabricated by stacking 90 layers of chromium and 90 layers of Al_2O_3 , alternatively. The thickness of each layer is 7-7.5 nm, and the entire superlattice thickness is 1350 nm. Cr and Al_2O_3 layers were deposited using an e-beam evaporation system, without breaking the vacuum. Figure 2.3 shows that the side surface of the sample as not smooth at edges, and thus, the surface was not suitable for transferring the graphene layer, and the subsequent e-beam lithography steps. We were able to further improve the surface roughness by breaking the silicon wafer along its crystallographic orientation.

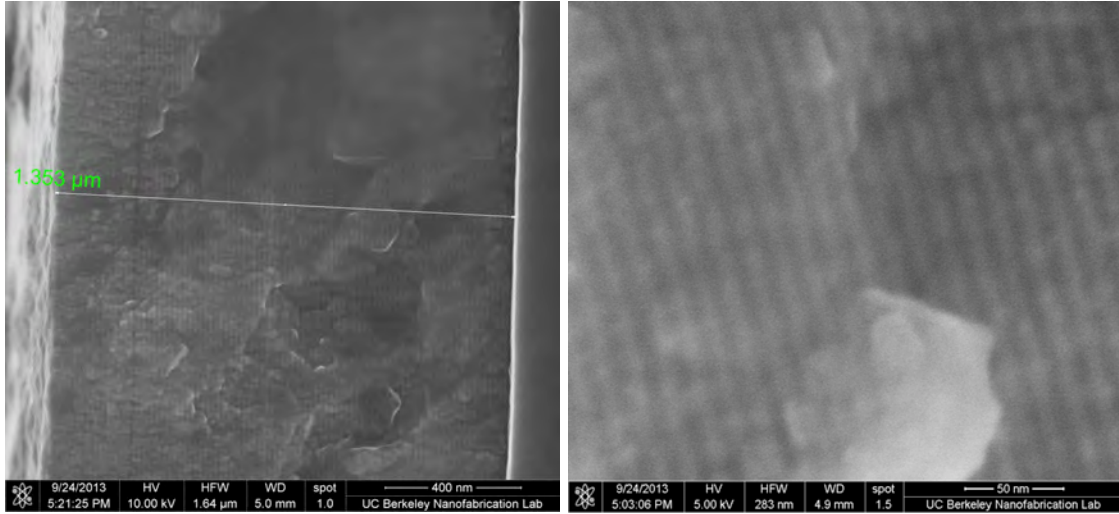


Figure 2.39: SEM micrograph of a metal-oxide superlattice consists of 180 layers of Cr and Al_2O_3 . The thickness of each layer is 7-7.5 nm.

At the time of writing, this project was still underway. Graphene transfer and electrical contact lithography steps had been completed, and low-temperature electrical measurement in a Cryogenic Probe Station was in progress.

2.3.3 Conclusion and future experiments

The desired structure to observe the superlattice effect in graphene, fell within the nominal resolution range of the accessible lithography systems. However, the nominal resolutions are usually measured in an ideal situation, where the substrate is very conductive, and the e-beam resist is ultra thin. Among the proposed structures, shown in Figure 2.31, the configuration in Figure 2.31 (d) was the most promising one. In this structure, electron beam creates the periodic potential on a very thin HSQ layer, which is coated on a graphene layer - a highly conductive substrate. In addition, no lift-off step is required in this method. At the time of writing, this method was also being pursued.

Chapter 3

Other experiments

3.1 C₆₀ filled carbon and boron-nitride nanotubes

Joseph Jankowski, an undergraduate student researcher at the Zettl lab, helped me with all experiments described in this chapter.

Motivations

The superconductivity behavior of alkali-metal compounds of fullerene (C₆₀) has been known since 1991 [1-2]. For example, K₃C₆₀ and Rb₃C₆₀ crystals show superconductivity transitions at T_c of 20.3 K and 30.5 K, respectively [3]. However, the underlying mechanism of this phenomenon is still a point of debate, and several theories have been proposed [3]. Since the superconductivity effect is closely related to the energy and types of phonons in a material, low-dimensional structures with altered phonon spectrum are an effective medium to study and analyze the superconductivity behavior. The goal in this project was to fabricate a one-dimensional chain from C₆₀ molecules, and then, dope them with potassium or rubidium atoms. The result would be a one-dimensional K₃C₆₀ or Rb₃C₆₀ structures. In order to achieve such one-dimensional structure, C₆₀ molecules were intercalated inside nanotubes. In Figure 3.1 shows the schematic of a double helix structure, made from C₆₀ molecules inside a nanotube [4].

The nanotube could be made out of carbon, or boron-nitride, and also, it could be a single-wall or a multi-wall structure.

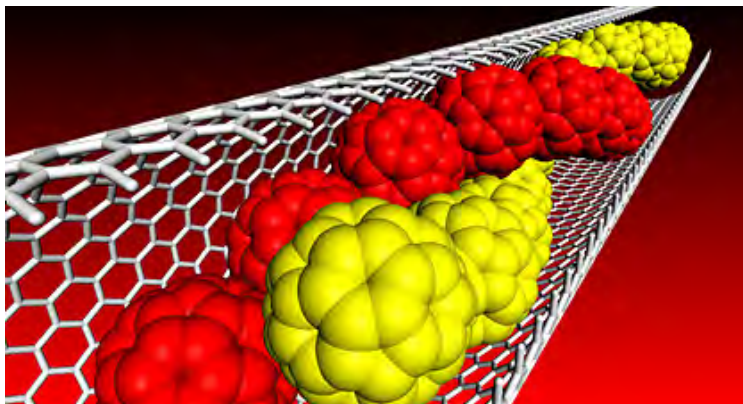


Figure 3.1: A double helix structure created by C_{60} molecules inside a nanotube. The tube could be made out of carbon or boron-nitride [4].

While using carbon nanotube would allow us to easily create electrical contacts with the C_{60} chain, the highly conductive graphitic tube walls could interfere with the transport measurement. In the same way, while using boron-nitride nanotubes would have the advantage of making C_{60} chains electrically insulated, it could complicate the fabrication of electrical contacts with the chains. Therefore, in order to compare the effect, I fabricated device structures, with both, carbon and boron-nitride nanotubes,.

Fabrication process

Since, most typical carbon nanotube growth methods result in capped carbon nanotubes, before filling multiwall carbon nanotubes with C_{60} molecules, first, tubes had to become uncapped.

In order to open the caps, carbon nanotubes were oxidized at around 600°C for 10 minutes in air. The exact length of oxidation was critical, because, short oxidation steps left most nanotubes capped, while long oxidation steps destroyed the entire, or a significant portion of nanotubes. In addition, the oxidation temperature and duration were strong functions of carbon nanotubes quality. For example, opening the cap in high quality tubes, created by arc-discharge method at the Zettl lab, was very challenging. The oxidation process was monitored using a Thermogravimetric Analyzer (TGA) system at the Zettl lab, where the sample total mass was monitored during the course of oxidation.

In the gas form, C_{60} Molecules are attracted by nanotubes through van der Waals force [5]. Therefore, the previously un-capped carbon nanotubes, and C_{60} crystals (99.5% purity from Sigma Aldrich) were placed in a 1/4" quartz tube. Then, using a vacuum pump, the quartz tube was pumped down to 10^{-5} Torr, and was sealed using a hydrogen torch. The resulting quartz ampule was placed in a box oven at 570°C for 36 hours. The vapor pressure of C_{60} in this condition is 1-100 mTorr [6]. Next, the ampules were left to cool down to the room temperature, and C_{60} -filled nanotubes were removed.

Transmission Electron Microscopy (TEM) analysis showed full and partially filled nanotubes, fabricated with this method, which is depicted in Figure 3.2. In order to protect C_{60} molecules from the TEM high-energy electron beam while imaging, a lower accelerating voltage (80kV as opposed to 100kV) was set.

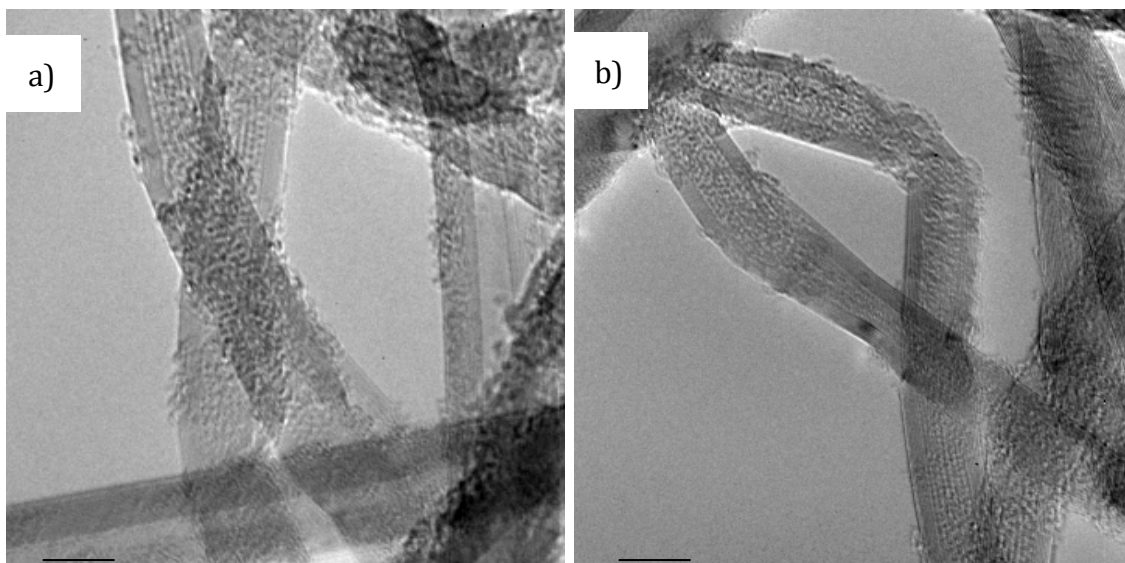


Figure 3.2: TEM images of multi-wall carbon nanotubes filled with C_{60} buckyballs. The scale bars are 10 nm.

After TEM examining the samples by TEM, C_{60} filled carbon nanotubes were dispersed in an Isopropanol Alcohol (IPA) solution, with an ultrasound dispersion tool for one hour. Next, by coating at 2000 rpm, carbon nanotubes were transferred to a silicon substrate with a 300nm SiO_2 layer, and pre-patterned alignment marks. Then, SEM technique was used to find and map C_{60} filled nanotubes on the substrate. Finally, metal contacts were patterned by e-beam lithography technique. In addition, in order to verify the existence of C_{60} molecules inside tubes, silicon-nitride Si_3N_4 membranes were used as the substrate, which allowed TEM examination of nanotubes.

Figure 3.3 shows the SEM micrograph of the final structure of a C_{60} filled carbon nanotube device, made on a silicon-nitride membrane. Electrical contacts were made from titanium-gold bi-layers. Electrical measurements on the device were conducted in the Zettl group's cryogenic probe station, located at 67 Birge Hall.

Further experiments

At the time of writing, the electrical measurements of C_{60} filled carbon nanotubes were in progress. Similar device structures with boron-nitride nanotubes instead of carbon nanotubes were also fabricated.

Theoretically, C_{60} chains require a substantial amount of extra electric charge¹ in order to become superconductor. In this experiment, the applied field from the back-gate provided the extra charge.

¹ In K_3C_{60} or Rb_3C_{60} , potassium or rubidium atoms provide this extra charge.

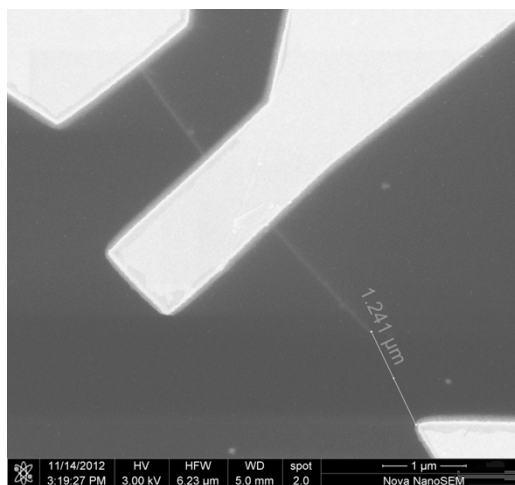
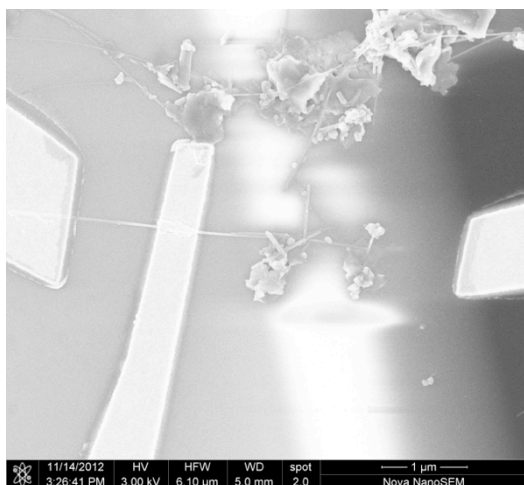
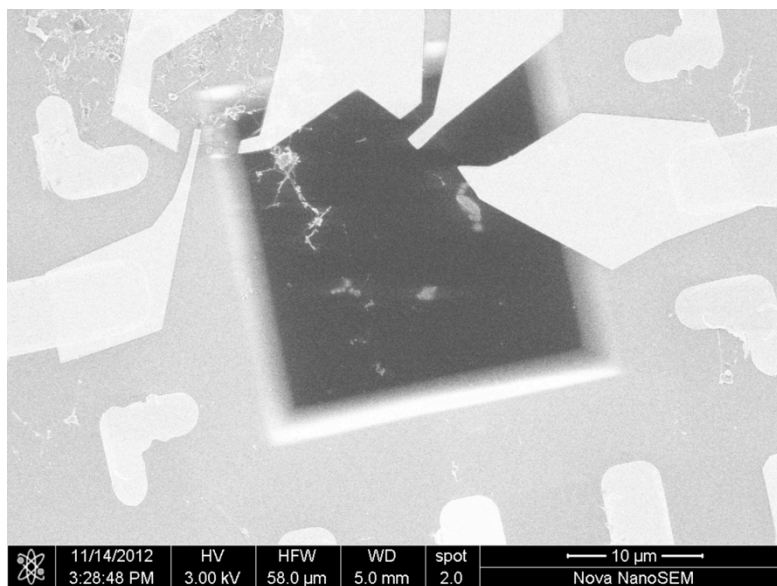


Figure 3.3: C_{60} filled carbon nanotube devices made on a 20nm thin silicon-nitride membrane. The metal contacts are a Ti-Au bi-layer.

3.2 Single boron-nitride nanotube optical waveguide and transducer

Motivations

Nanoelectromechanical systems in general, and nano-scale cantilevers in particular hold the world's record of sensitivity in measuring displacement [7], force [8], and mass [7,9,10]. However, they usually suffer from bandwidth [11-12], or optical diffraction [13-14] limits. This project was based on a report in which, a nano-scale silicon nanocantilever transducer was fabricated. Due to the non-interferometric mechanism of transduction in this structure, it did not suffer from the diffraction limit [15]. Figure 3.4 shows the device structure.

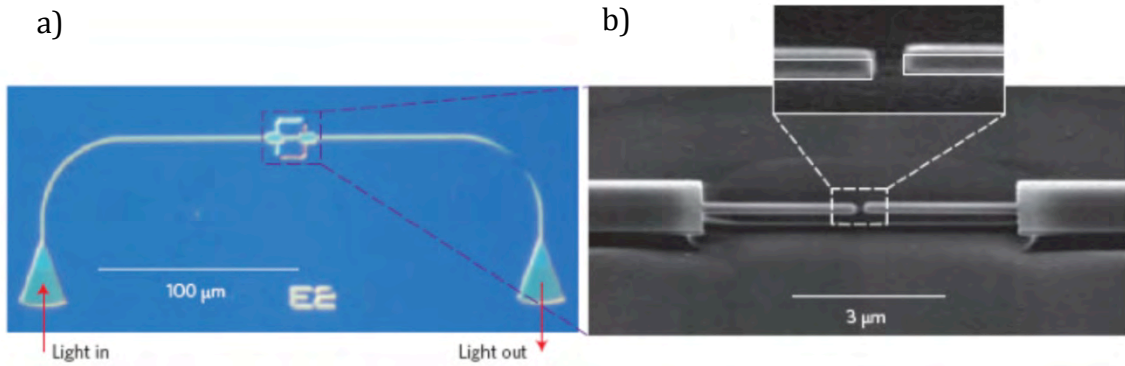


Figure 3.4: (a) “Optical microscope image of the photonic circuitry, showing the nanomechanical cantilevers in the centre and the two grating couplers at the ends of the waveguides.” (b) “SEM image of the end-to-end coupled waveguide nanocantilever devices. The inset shows how the ends of the nanocantilevers are offset by 25 nm in the out-of-plane direction. The waveguide cross-section is $500 \times 110 \text{ nm}^2$ ” [15]

Due to the high Young's modulus, and the low mass density of nanotubes, they tend to be superior candidates as nano-cantilevers. However, since this type of transducer was an optomechanical system, a large band gap material (i.e. boron-nitride nanotube) was required. The diameter of a typical multiwall boron-nitride nanotube is significantly smaller than the silicon nano-cantilever used in the reported experiment². Therefore, in order to verify that the boron-nitride nanotubes were able to act as optical waveguides, I fabricated a similar structure, but with no gap in the middle. I used a single boron-nitride nanotube, and in order to compensate for the smaller nanotube cross-section, I performed the experiments with lasers in the visible range³.

Fabrication Process

The device structure consisted of two optical waveguides, attached to a single boron-nitride nanotube, which is located in the center. In order to couple the incoming laser beam to the optical mode of waveguides, optical couplers were created at each

² The silicon nanocantilever's cross-section was $110 \times 500 \text{ nm}^2$, and the diameter of a typical boron-nitride nanotube is 30-100 nm.

³ The transducer in ref. 15 is a broadband system working at the near infrared (NIR) range.

waveguide's end. The laser beam entered one of waveguides through its optical coupler, and after passing through the boron-nitride nanotube and the second waveguide, exited from the following coupler, and was detected by a CCD, or a photodetector device.

I replicated the same waveguide structure that was used in ref. 15. However, I experimented with different materials in the waveguide structure. Table 3.1 shows a list of experimented materials and their corresponding energy gap, and refractive index.

Material	Gap (eV)	n
Al ₂ O ₃	8.8	1.63
TiO ₂	3.5	2.45-2.9
ZrO ₂	5.8	2
SU-8	In UV	1.57

Table 3.1: Comparison between materials that was tested for the optical waveguide body. The structure guided the optical beam to, and from the boron-nitride nanotube.

In order to achieve a high-quality waveguide, it has to be created from high refractive index materials, with small surface roughness. Among the tested materials, SU-8 had the lowest refractive index. However, using SU-8 significantly simplified the fabrication process by eliminating the lift-off step. SU-8 is a negative tone e-beam and photoresist. Therefore, after examining all the materials listed in table 3.1, SU-8 polymer was selected as the waveguide material.

In order to fabricate the device, first, I dispersed the boron-nitride nanotubes (BNNT), by sonicating BNNTs in IPA for one hour. Then, I transferred the tubes to a Si-SiO₂ substrate with pre-patterned alignment marks, by spin coating at 2000 rpm. Next, SU-8 waveguides were attached to boron-nitride nanotubes, using e-beam lithography technique. The rectangular shape at each waveguide's end is an optical coupler, which is responsible to match the incoming light to the proper waveguide's optical mode.

Boron-nitride tubes in this experiment were 10-20µm in length, and 50-100nm in diameter. The thickness of the SU-8 layer was around 300 nm.

Results and Future Experiments

Figure 3.5 shows typical waveguide structures, fabricated from the materials mentioned in Table 3.1. Figure 3.6 is the AFM image of a device made from ZrO₂ (a) and TiO₂ (b,c). As displayed in Figure 3.6, the resulting oxide layers, deposited with the ALD machine built in the Zettl lab, exhibited a poor surface roughness. Figure 3.7 shows the final structure of the device, made with SU-8 waveguides, which is connected to a boron-nitride nanotube at the center.

Optical measurement experiments were conducted at the Prof. Wang's lab in Physics Department. The measurement setup consisted of a stage to mount the sample, a 514 nm

laser, and a CCD detector. The laser beam was focused on one of the couplers with a 30° angle. The output was detected from the other waveguide using the CCD camera.

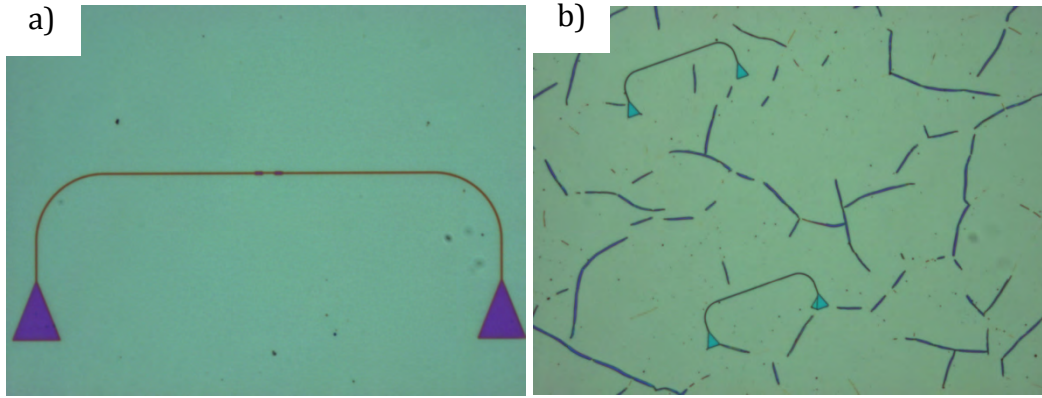


Figure 3.5: Waveguide structures made from ZrO_2 (a) and Al_2O_3 (b). Oxide layers were deposited by ALD technique, and waveguide structures were formed using the lift-off method.

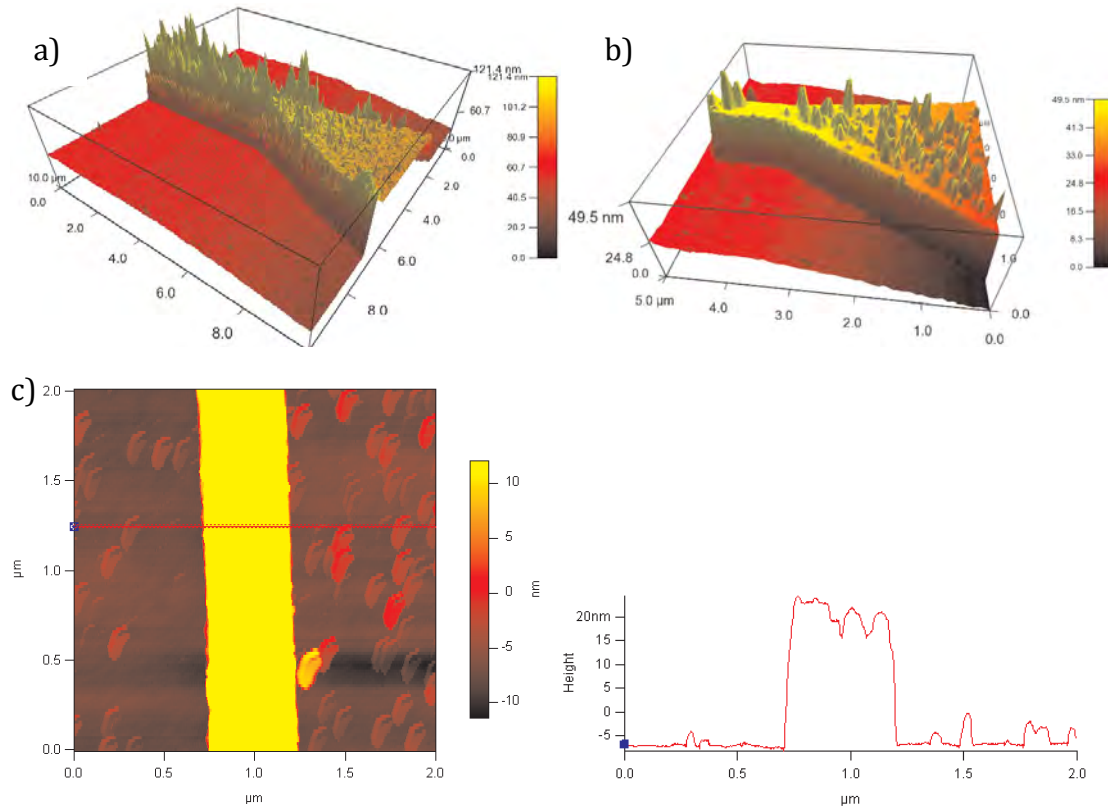


Figure 3.6: AFM analysis of oxide layers deposited with a ALD technique. 30 nm layers of ZrO_2 (a) and TiO_2 (b and c) show large surface roughnesses. The inset in (c) is the height profile along the red line.

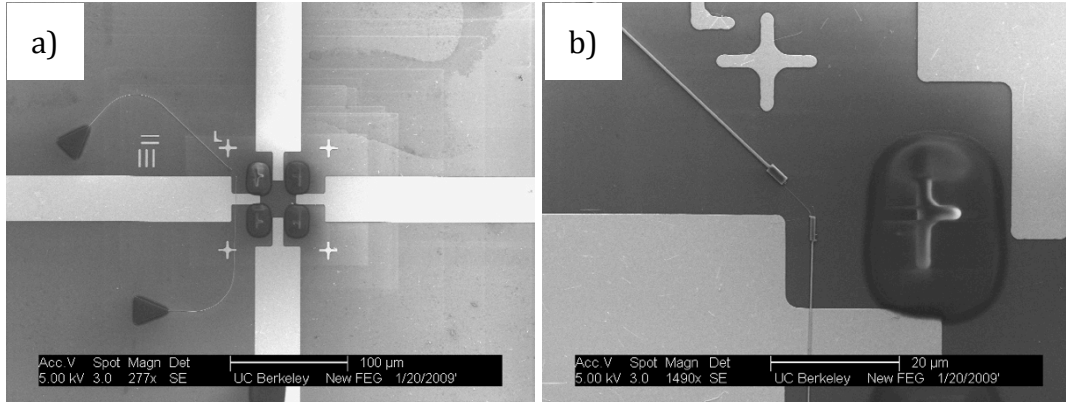


Figure 3.7: SEM micrograph of the waveguide device structure. Two SU-8 waveguides are connected to a 10 μm long boron-nitride nanotube at the center.

Figure 3.8 shows the output as measured by the CCD camera, from the device shown in Figure 3.7. The same experiment was conducted on a similar device, except with no BNNTs. This result shows that a single boron-nitride nanotube is able to perform as an optical waveguide. However, in order to calculate the energy loss in the waveguide, a more quantitative analysis was required. Energy loss measurements could be conducted with photodetectors by measuring the output beam power, and compare it to the source power. The next step in this project was to measure the boron-nitride waveguide device with a photodetector, and find the energy loss.

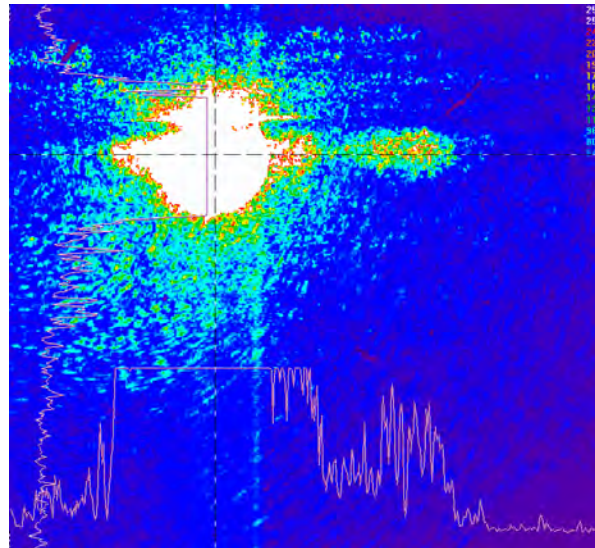


Figure 3.8: The output signal from the second SU-8 waveguide, detected by a CCD camera, confirming that the beam was able to pass through the BNNT.

In addition, other experiments such as etching the underneath substrate to suspend the boron-nitride nanotube, fabricating a single-clamped BNNT cantilever, by leaving a small gap between the nanotube and one of waveguides, and measuring the sensitivity of the resulting device as a mass, or a force sensor.

Bibliography

Chapter 1

1. Peierls, Rudolf E. *Quantum Theory of Solids*. Oxford: Clarendon Press, 1955. 108.
2. Frohlich, H. "On the Theory of Superconductivity: The One-Dimensional Case." *Proceedings of the Royal Society A: Mathematical, Physical and Engineering Sciences* 223, no. 1154 (1954): 296-305. doi:10.1098/rspa.1954.0116.
3. Grüner, G., and A. Zettl. "Charge Density Wave Conduction: A Novel Collective Transport Phenomenon in Solids." *Physics Reports* 119, no. 3 (1985): 117-232. doi:10.1016/0370-1573(85)90073-0.
4. *Electronic Properties of Inorganic Quasi-One-Dimensional Materials*. Edited by Pierre Monceau. Vol. 2. The Netherlands: Reidel Dordrecht, 1985. 139.
5. Hütiray, G., and J. Solyom, eds. *Lecture Notes in Physics*. Vol. 217. Berlin: Springer-Verlag, 1985.
6. Jérôme, D., and L. G. Caron. *Low-dimensional Conductors and Superconductors*. New York: Plenum Press, 1987.
7. Miller, Joel S., and Arthur J. Epstein. *Synthesis and Properties of Low-dimensional Materials*. Vol. 313. New York: New York Academy of Sciences, 1978. 128.
8. Grüner, G., and A. Zettl. "Charge Density Wave Conduction: A Novel Collective Transport Phenomenon in Solids." *Physics Reports* 119, no. 3 (1985): 117-232. doi:10.1016/0370-1573(85)90073-0.
9. Ziman, J. M. "Chapter 5." In *Principles of the Theory of Solids*. Cambridge: Cambridge University Press, 1979.
10. Laughlin, Robert B. "The Lindhard Function." The Lindhard Function. April 15, 2008. Accessed April 07, 2015. <http://large.stanford.edu/courses/2008/ph373/yao1/>.
11. Lee, P., T. Rice, and P. Anderson. "Fluctuation Effects at a Peierls Transition." *Physical Review Letters* 31, no. 7 (1973): 462-65. doi:10.1103/PhysRevLett.31.462.
12. Kuse, D., and H. Zeller. "Evidence for One-Dimensional Metallic Behavior in $\text{K}_2\text{Pt}(\text{CN})_4\text{Br}_{0.3} \cdot (\text{H}_2\text{O})_n$." *Physical Review Letters* 27, no. 16 (1971): 1060-063. doi:10.1103/PhysRevLett.27.1060; Renker, B., H. Rietschel, L. Pintschovius, W. Gläser, P. Brüesch, D. Kuse, and M. Rice. "Observation of Giant Kohn Anomaly in the One-Dimensional Conductor $\text{K}_2\text{Pt}(\text{CN})_4\text{Br}_{0.3} \cdot 3\text{H}_2\text{O}$." *Physical Review Letters* 30, no. 22 (1973): 1144-147. doi:10.1103/PhysRevLett.30.1144.

13. Devreese, J. T., Roger Evrard, and Van Doren Victor E. *Highly Conducting One-dimensional Solids*. New York: Plenum Press, 1979. 69-373.
14. Monceau, P., N. Ong, A. Portis, A. Meerschaut, and J. Rouxel. "Electric Field Breakdown of Charge-Density-Wave—Induced Anomalies in NbSe₃." *Physical Review Letters* 37, no. 10 (1976): 602-06. doi:10.1103/PhysRevLett.37.602.
15. Fleming, R., D. Moncton, and D. Mcwhan. "X-ray Scattering and Electric Field Studies of the Sliding Mode Conductor NbSe₃." *Physical Review B* 18, no. 10 (1978): 5560-563. doi:10.1103/PhysRevB.18.5560.
16. Fleming, R., and C. Grimes. "Sliding-Mode Conductivity in NbSe₃: Observation of a Threshold Electric Field and Conduction Noise." *Physical Review Letters* 42, no. 21 (1979): 1423-426. doi:10.1103/PhysRevLett.42.1423.
17. Fleming, R. "Electric-field Depinning of Charge-density Waves in NbSe₃." *Physical Review B* 22, no. 12 (1980): 5606-612. doi:10.1103/PhysRevB.22.5606.
18. Lee, P., and T. Rice. "Electric Field Depinning of Charge Density Waves." *Physical Review B* 19, no. 8 (1979): 3970-980. doi:10.1103/PhysRevB.19.3970.
19. Grüner, G., A. Zettl, W. Clark, and John Bardeen. "Field and Frequency Dependence of Charge-density-wave Conduction in NbSe₃." *Physical Review B* 24, no. 12 (1981): 7247-257. doi:10.1103/PhysRevB.24.7247.
20. Lee, P., and T. Rice. "Electric Field Depinning of Charge Density Waves." *Physical Review B* 19, no. 8 (1979): 3970-980. doi:10.1103/PhysRevB.19.3970.
21. Sridhar, S., D. Reagor, and G. Gruner. "Inertial Dynamics of Pinned Charge-density-wave Condensates. II. Orthorhombic TaS₃." *Physical Review B* 34, no. 4 (1986): 2223-230. doi:10.1103/PhysRevB.34.2223.
22. Wu, Wei-Yu, A. Jánossy, and G. Grüner. "Correlation between the Static Dielectric Constant and Threshold Electric Field for Sliding Charge Density Wave Conduction." *Solid State Communications* 49, no. 11 (1984): 1013-017. doi:10.1016/0038-1098(84)90412-5.
23. Monceau, P., J. Richard, and M. Renard. "Interference Effects of the Charge-Density-Wave Motion in NbSe₃." *Physical Review Letters* 45, no. 1 (1980): 43-46. doi:10.1103/PhysRevLett.45.43.
24. Mozurkewich, George, and George Grüner. "Volume Dependence of Current Oscillations in NbSe₃: A Finite-Size Effect." *Physical Review Letters* 51, no. 24 (1983): 2206-209. doi:10.1103/PhysRevLett.51.2206.

25. Brown, S., and L. Mihaly. "Coherent Voltage Oscillations Induced by Sliding Charge-Density Waves: Interface or Bulk Phenomenon?" *Physical Review Letters* 55, no. 7 (1985): 742-45. doi:10.1103/PhysRevLett.55.742.
26. Fleming, R. "Electric-field Depinning of Charge-density Waves in NbSe₃." *Physical Review B* 22, no. 12 (1980): 5606-612. doi:10.1103/PhysRevB.22.5606.
27. Richard, J., P. Monceau, M. Papoular, and M. Renard. "Fnoise in NbSe₃." *Journal of Physics C: Solid State Physics* 15, no. 35 (1982): 7157-164. doi:10.1088/0022-3719/15/35/013.
28. Meerschaut, A., and J. Rouxel. "Le Seleniure NbSe₃: Obtention Et Structure." *Journal of the Less Common Metals* 39, no. 2 (1975): 197-203. doi:10.1016/0022-5088(75)90194-0.
29. Roucau, C., R. Ayroles, P. Monceau, L. Guemas, A. Meerschaut, and J. Rouxel. "Electron Diffraction and Resistivity Measurements on the One-dimensional Orthorhombic and Monoclinic Structures of TaS₃. Comparison with NbSe₃." *Physica Status Solidi (a)* 62, no. 2 (1980): 483-93. doi:10.1002/pssa.2210620216.
30. Wilson, J. "Bands, Bonds, and Charge-density Waves in the NbSe₃ Family of Compounds." *Physical Review B* 19, no. 12 (1979): 6456-468. doi:10.1103/PhysRevB.19.6456.
31. Monceau, P., J. Richard, and M. Renard. "Charge-density-wave Motion in NbSe₃. I. Studies of the Differential Resistance DV/dI." *Physical Review B* 25, no. 2 (1982): 931-47. doi:10.1103/PhysRevB.25.931.
32. Monceau, P., J. Richard, and M. Renard. "Interference Effects of the Charge-Density-Wave Motion in NbSe₃." *Physical Review Letters* 45, no. 1 (1980): 43-46. doi:10.1103/PhysRevLett.45.43.
33. Ong, N.p., and C.m. Gould. "Frequency Pulling and Heterodyning Observed in Voltage Spectrum of the Fröhlich Conductor NbSe₃." *Solid State Communications* 37, no. 1 (1981): 25-31. doi:10.1016/0038-1098(81)90881-4.
34. Nakamura, S., and R. Aoki. "Satellite Electron-diffraction in NbSe₃ below T = 59 K." *Solid State Communications* 27, no. 2 (1978): 151-53. doi:10.1016/0038-1098(78)90821-9.
35. Kamimura, Hiroshi. *Theoretical Aspects of Band Structures and Electronic Properties of Pseudo-one-dimensional Solids*. Dordrecht: Reidel, 1985. 231.
36. Bullett, D. W. "Electron States in One-dimensional Niobium Chalcogenides: NbSe₃ and FeNbSe₃." *Journal of Physics C: Solid State Physics* 15, no. 14 (1982): 3069-077. doi:10.1088/0022-3719/15/14/014.

37. Devreux, F. "⁹³Nb NMR Study of NbSe₃." *Journal De Physique France* 43, no. 10 (October/November 1982): 1489-495. doi:10.1051/jphys:0198200430100148900.
38. Bouchard, George Henry, Jerome H. Perlstein, and Michell J. Sienko. "Solid-state Studies of Potassium Molybdenum Bronzes." *Inorganic Chemistry* 6, no. 9 (1967): 1682-685. doi:10.1021/ic50055a016.
39. Buder, R., J. Devenyi, J. Dumas, J. Marcus, J. Mercier, C. Schlenker, and H. Vincent. "Two-dimensional Electronic Properties of the Purple Potassium Molybdenum Bronze K_{0.9}Mo₆O₁₇." *Journal De Physique Lettres* 43, no. 2 (1982): 59-65. doi:10.1051/jphyslet:0198200430205900.
40. Hagenmuller, P. "Les Bronzes Oxygénés." *Progress in Solid State Chemistry* 5 (1971): 71-144. doi:10.1016/0079-6786(71)90017-3.
41. Fogle, William, and Jerome Perlstein. "Semiconductor-to-Metal Transition in the Blue Potassium Molybdenum Bronze, K_{0.30} MoO₃; Example of a Possible Excitonic Insulator." *Physical Review B* 6, no. 4 (1972): 1402-412. doi:10.1103/PhysRevB.6.1402.
42. Devreese, J. T., L. F. Lemmens, Van Doren Victor E., and J. Van. Royen. *Recent Developments in Condensed Matter Physics*. Vol. 2. New York: Plenum Press, 1981. 181.
43. Travaglini, G., P. Wachter, J. Marcus, and C. Schlenker. "The Blue Bronze K_{0.3}MoO₃: A New One-dimensional Conductor." *Solid State Communications* 37, no. 7 (1981): 599-603. doi:10.1016/0038-1098(81)90143-5.
44. Pouget, J.p., S. Kagoshima, C. Schlenker, and J. Marcus. "Evidence for a Peierls Transition in the Blue Bronzes K_{0.30}MoO₃ and Rb_{0.30}MoO₃." *Journal De Physique Lettres* 44, no. 3 (1983): 113-20. doi:10.1051/jphyslet:01983004403011300.
45. Dumas, J., C. Schlenker, J. Marcus, and R. Buder. "Nonlinear Conductivity and Noise in the Quasi One-Dimensional Blue Bronze K_{0.30}MoO₃." *Physical Review Letters* 50, no. 10 (1983): 757-60. doi:10.1103/PhysRevLett.50.757.
46. Fogle, William, and Jerome Perlstein. "Semiconductor-to-Metal Transition in the Blue Potassium Molybdenum Bronze, K_{0.30} MoO₃; Example of a Possible Excitonic Insulator." *Physical Review B* 6, no. 4 (1972): 1402-412. doi:10.1103/PhysRevB.6.1402.
47. Pouget, J.p., S. Kagoshima, C. Schlenker, and J. Marcus. "Evidence for a Peierls Transition in the Blue Bronzes K_{0.30}MoO₃ and Rb_{0.30}MoO₃." *Journal De Physique Lettres* 44, no. 3 (1983): 113-20. doi:10.1051/jphyslet:01983004403011300.

48. Lee, P., and T. Rice. "Electric Field Depinning of Charge Density Waves." *Physical Review B* 19, no. 8 (1979): 3970-980. doi:10.1103/PhysRevB.19.3970.
49. Travaglini, G., P. Wachter, J. Marcus, and C. Schlenker. "The Blue Bronze K_{0.3}MoO₃: A New One-dimensional Conductor." *Solid State Communications* 37, no. 7 (1981): 599-603. doi:10.1016/0038-1098(81)90143-5.
50. Jérôme, D., and L. G. Caron. *Low-dimensional Conductors and Superconductors*. New York: Plenum Press, 1987.
51. Tsutsumi, Kitomi, Tsuyoshi Tamegai, Seiichi Kagoshima, Hideki Tomozawa, and Masatoshi Sato. "Transport Properties of the Charge-Density-Wave State in KMoO₃." *Journal of the Physics Society Japan* 53, no. 11 (1984): 3946-951. doi:10.1143/JPSJ.53.3946.
52. McCarten, J., D. Dicarolo, M. Maher, T. Adelman, and R. Thorne. "Charge-density-wave Pinning and Finite-size Effects in NbSe₃." *Physical Review B* 46, no. 8 (1992): 4456-482. doi:10.1103/PhysRevB.46.4456.
53. Maher, M., T. Adelman, S. Ramakrishna, J. McCarten, D. Dicarolo, and R. Thorne. "Charge-density-wave Phase Slip and Current Conversion in NbSe₃." *Physical Review Letters* 68, no. 20 (1992): 3084-087. doi:10.1103/PhysRevLett.68.3084.
54. Zaitsev-Zotov, S. V. "New Phenomena in CDW Systems at Small Scales." ArXiv:1107.4444 [cond-mat.mes-hall].
55. Hundley, Michael Frederic. *Static and Dynamic Properties of Charge Density Wave Conductors and Other Low Dimensional Materials*. (Doctoral dissertation), 1988.
56. Takahide, Yamaguchi, Shinya Uji, Kengo Enomoto, Takako Konoike, Taichi Terashima, Mitsuka Nishimura, Taku Tsuneta, Katsuhiko Inagaki, Satoshi Tanda, and Kazuhiko Yamaya. "Finite-size Effects on Transverse Magnetoresistance of NbSe₃." *Physical Review B* 71, no. 13 (2005). doi:10.1103/PhysRevB.71.134409.
57. Walter, U., R. Thomson, B. Burk, M. Crommie, A. Zettl, and John Clarke. "Scanning Tunneling Microscopy of the Blue Bronzes (Rb,K)_{0.3}MoO₃." *Physical Review B* 45, no. 20 (1992): 11474-1480. doi:10.1103/PhysRevB.45.11474.
58. Nanofab, University of Alberta. *ZEP Exposure and Development Results*, February 14, 2011. Accessed April 7, 2015. http://www.nanofab.ualberta.ca/wp-content/uploads/downloads/2011/02/ZEP_Exposure_Results.pdf.
59. Zettl, Alexander K. *Charge-density-wave Transport in Transition-metal Trichalcogenides*. (Doctoral dissertation), UCLA, 1983.
60. "DT-670 Specifications." DT-670 Silicon Diodes. Accessed April 07, 2015.

<http://www.lakeshore.com/products/Cryogenic-Temperature-Sensors/Silicon-Diodes/DT-670/Pages/Specifications.aspx>.

61. Texas, Instruments. *UA733C, UA733M Specifications*.
<http://www.ti.com/lit/ds/symlink/ua733.pdf>.
62. Keysight. "E4402B ESA-E Specifications." E4402B Spectrum Analyzer. Accessed April 07, 2015. <http://goo.gl/VyEbGz>.
63. Lide, David R. *CRC Handbook of Chemistry and Physics: A Ready-reference Book of Chemical and Physical Data*. Boca Raton, FL: CRC, 2008. 12-114.
64. Bardeen, John, E. Ben-Jacob, A. Zettl, and G. Grüner. "Current Oscillations and Stability of Charge-Density-Wave Motion in." *Physical Review Letters* 49, no. 7 (1982): 493-96. doi:10.1103/PhysRevLett.49.493.
65. Fleming, R., D. Moncton, and D. Mcwhan. "X-ray Scattering and Electric Field Studies of the Sliding Mode Conductor NbSe₃." *Physical Review B* 18, no. 10 (1978): 5560-563. doi:10.1103/PhysRevB.18.5560.
66. Dicarlo, D., J. McCarten, T. Adelman, M. Maher, and R. Thorne. "Size Effects and Charge-density-wave Pinning in Nb_{1-x}Ti_xSe₃: Evidence for Weak Pinning by a Nonisoelectronic Impurity." *Physical Review B* 42, no. 12 (1990): 7643-646. doi:10.1103/PhysRevB.42.7643.
67. Blue Bronze Crystals. Digital image. Wikipedia.
<http://upload.wikimedia.org/wikipedia/commons/3/35/KMoO3Bronze.JPG>.

Chapter 2

1. Novoselov, K. S. "Electric Field Effect in Atomically Thin Carbon Films." *Science* 306, no. 5696 (2004): 666-69. doi:10.1126/science.1102896.
2. Novoselov, K. S. "Two-dimensional Atomic Crystals." *Proceedings of the National Academy of Sciences* 102, no. 30 (2005): 10451-0453. doi:10.1073/pnas.0502848102.
3. Wallace, P. "The Band Theory of Graphite." *Physical Review* 71, no. 9 (1947): 622-34. doi:10.1103/PhysRev.71.622.
4. Slonczewski, J., and P. Weiss. "Band Structure of Graphite." *Physical Review* 109, no. 2 (1958): 272-79. doi:10.1103/PhysRev.109.272.
5. Boehm, H. P., A. Clause, G. O. Fischer, and U. Hofmann. "Dünnste Kohlenstoff-folien." *Zeitschrift Für Naturforschung* 17, no. B, 150.

6. Dresselhaus, M.s., and G. Dresselhaus. "Intercalation Compounds of Graphite." *Advances in Physics* 30, no. 2 (1981): 139-326. doi:10.1080/00018738100101367.
7. Zhang, Yuanbo, Joshua P. Small, William V. Pontius, and Philip Kim. "Fabrication and Electric-field-dependent Transport Measurements of Mesoscopic Graphite Devices." *Applied Physics Letters* 86, no. 7 (2005): 073104. doi:10.1063/1.1862334.
8. Berger, Claire, Zhimin Song, Tianbo Li, Xuebin Li, Asmerom Y. Ogbazghi, Rui Feng, Zhenting Dai, Alexei N. Marchenkov, Edward H. Conrad, Phillip N. First, and Walt A. De Heer. "Ultrathin Epitaxial Graphite: 2D Electron Gas Properties and a Route toward Graphene-based Nanoelectronics." *The Journal of Physical Chemistry B* 108, no. 52 (2004): 19912-9916. doi:10.1021/jp040650f.
9. "Andre Geim - Facts." Andre Geim - Facts. Accessed April 07, 2015. http://www.nobelprize.org/nobel_prizes/physics/laureates/2010/geim-facts.html.
10. "MOS Capacitors." EE130 Lecture Notes. Accessed April 07, 2015. <http://www-inst.eecs.berkeley.edu/~ee130/sp03/lecture.html>.
11. "High Electron Mobility Transistor." Digital image. Wikipedia. Accessed April 7, 2015. http://upload.wikimedia.org/wikipedia/commons/3/30/High_Electron_MobilityTransistor_-_electron_energy_band_structure_%28DE%29.svg.
12. Streetman, Ben G. *Solid State Electronic Devices*. Englewood Cliffs, NJ: Prentice-Hall, 1980.
13. Reich, S., J. Maultzsch, C. Thomsen, and P. Ordejón. "Tight-binding Description of Graphene." *Physical Review B* 66, no. 3 (2002). doi:10.1103/PhysRevB.66.035412.
14. Neto, A. H. Castro, N. M. R. Peres, K. S. Novoselov, and A. K. Geim. "The Electronic Properties of Graphene." *Reviews of Modern Physics* 81, no. 1 (2009): 109-62. doi:10.1103/RevModPhys.81.109.
15. Gannett, William Joy. *Electronic Transport in Novel Graphene Nanostructures*. (Doctoral dissertation), University of California, Berkeley, 2012.
16. Ashcroft, Neil W., and N. David Mermin. *Solid State Physics*. New York: Holt, Rinehart and Winston, 1976.
17. Park, Cheol-Hwan, Li Yang, Young-Woo Son, Marvin Cohen, and Steven Louie. "New Generation of Massless Dirac Fermions in Graphene under External Periodic Potentials." *Physical Review Letters* 101, no. 12 (2008). doi:10.1103/PhysRevLett.101.126804.
18. Park, Cheol-Hwan, Li Yang, Young-Woo Son, Marvin L. Cohen, and Steven G.

- Louie. "Anisotropic Behaviours of Massless Dirac fermions in Graphene under Periodic potentials." *Nature Physics* 4, no. 3 (2008): 213-17. doi:10.1038/nphys890.
19. Ando, Tsuneya, and Takeshi Nakanishi. "Impurity Scattering in Carbon Nanotubes - Absence of Back Scattering -." *Journal of the Physics Society Japan* 67, no. 5 (1998): 1704-713. doi:10.1143/JPSJ.67.1704.
 20. Ando, Tsuneya, Takeshi Nakanishi, and Riichiro Saito. "Berry's Phase and Absence of Back Scattering in Carbon Nanotubes." *Journal of the Physics Society Japan* 67, no. 8 (1998): 2857-862. doi:10.1143/JPSJ.67.2857.
 21. Mceuen, Paul, Marc Bockrath, David Cobden, Young-Gui Yoon, and Steven Louie. "Disorder, Pseudospins, and Backscattering in Carbon Nanotubes." *Physical Review Letters* 83, no. 24 (1999): 5098-101. doi:10.1103/PhysRevLett.83.5098.
 22. Li, X., W. Cai, J. An, S. Kim, J. Nah, D. Yang, R. Piner, A. Velamakanni, I. Jung, E. Tutuc, S. K. Banerjee, L. Colombo, and R. S. Ruoff. "Large-Area Synthesis of High-Quality and Uniform Graphene Films on Copper Foils." *Science* 324, no. 5932 (2009): 1312-314. doi:10.1126/science.1171245.
 23. Lindberg CVD Furnace. Digital image. Zettl Group Internal Site. Accessed May 13, 2015.
http://research.physics.berkeley.edu/zettl/stuffinternal/wiki/lib/exe/detail.php?id=cvd&media=lindberg_blue_furnace.jpg.
 24. Erickson, Kristopher John. (2012). *Synthesis and Functionalization of Carbon and Boron Nitride Nanomaterials and Their Applications*. (Doctoral dissertation) UC Berkeley: Chemistry. Retrieved from: <https://escholarship.org/uc/item/9zd4z0nm>
 25. MICROCHEM. Nano PMMA and Copolymer. Accessed April 13, 2015.
http://microchem.com/pdf/PMMA_Data_Sheet.pdf.
 26. Meyer, Jannik C., C. O. Girit, M. F. Crommie, and A. Zettl. "Hydrocarbon Lithography on Graphene Membranes." *Applied Physics Letters Appl. Phys. Lett.* 92, no. 12 (2008): 123110. doi:10.1063/1.2901147.

Chapter 3

1. Hebard, A. F., M. J. Rosseinsky, R. C. Haddon, D. W. Murphy, S. H. Glarum, T. T. M. Palstra, A. P. Ramirez, and A. R. Kortan. "Superconductivity at 18 K in Potassium-doped C60." *Nature* 350, no. 6319 (1991): 600-01. doi:10.1038/350600a0.
2. Holczer, K., O. Klein, S.-M. Huang, R. B. Kaner, K.-J. Fu, R. L. Whetten, and F. Diederich. "Alkali-Fulleride Superconductors: Synthesis, Composition, and

- Diamagnetic Shielding." *Science* 252, no. 5009 (1991): 1154-157. doi:10.1126/science.252.5009.1154.
3. Degiorgi, L., G. Briceno, M. S. Fuhrer, A. Zettl, and P. Wachter. "Optical Measurements of the Superconducting Gap in Single-crystal K3C60 and Rb3C60." *Nature* 369, no. 6481 (1994): 541-43. doi:10.1038/369541a0.
 4. "Inovação Unicamp." Digital image. Inovação Unicamp. Accessed April 11, 2015. <http://www.inova.unicamp.br/inovacao/report/entre-douglasgalvao.shtml>.
 5. Berber, Savas, Young-Kyun Kwon, and David Tománek. "Microscopic Formation Mechanism of Nanotube Peapods." *Physical Review Letters* 88, no. 18 (2002). doi:10.1103/PhysRevLett.88.185502.
 6. Piacente, V., G. Gigli, P. Scardala, A. Giustini, and D. Ferro. "Vapor Pressure of C60 Buckminsterfullerene." *The Journal of Physical Chemistry* 99, no. 38 (1995): 14052-4057. doi:10.1021/j100038a041.
 7. Li, Mo, H. X. Tang, and M. L. Roukes. "Ultra-sensitive NEMS-based Cantilevers for Sensing, Scanned Probe and Very High-frequency Applications." *Nature Nanotechnology* 2, no. 2 (2007): 114-20. doi:10.1038/nnano.2006.208.
 8. Rugar, D., R. Budakian, H. J. Mamin, and B. W. Chui. "Single Spin Detection by Magnetic Resonance Force Microscopy." *Nature* 430, no. 6997 (2004): 329-32. doi:10.1038/nature02658.
 9. Ilic, B. "Attogram Detection Using Nanoelectromechanical Oscillators." *Journal of Applied Physics* 95, no. 7 (2004): 3694. doi:10.1063/1.1650542.
 10. Yang, Y. T., C. Callegari, X. L. Feng, K. L. Ekinici, and M. L. Roukes. "Zeptogram-Scale Nanomechanical Mass Sensing." *Nano Letters* 6, no. 4 (2006): 583-86. doi:10.1021/nl052134m.
 11. Huang, Xue Ming Henry, Christian A. Zorman, Mehran Mehregany, and Michael L. Roukes. "Nanoelectromechanical Systems: Nanodevice Motion at Microwave Frequencies." *Nature* 421, no. 6922 (2003): 496. doi:10.1038/421496a.
 12. Truitt, Patrick A., Jared B. Hertzberg, C. C. Huang, Kamil L. Ekinici, and Keith C. Schwab. "Efficient and Sensitive Capacitive Readout of Nanomechanical Resonator Arrays." *Nano Letters* 7, no. 1 (2007): 120-26. doi:10.1021/nl062278g.
 13. Carr, Dustin W., S. Evoy, L. Sekaric, H. G. Craighead, and J. M. Parpia. "Measurement of Mechanical Resonance and Losses in Nanometer Scale Silicon Wires." *Applied Physics Letters* 75, no. 7 (1999): 920. doi:10.1063/1.124554.
 14. Azak, N. O., M. Y. Shagam, D. M. Karabacak, K. L. Ekinici, D. H. Kim, and D. Y.

Jang. "Nanomechanical Displacement Detection Using Fiber-optic Interferometry." *Applied Physics Letters* 91, no. 9 (2007): 093112. doi:10.1063/1.2776981.

15. Li, Mo, W. H. P. Pernice, and H. X. Tang. "Broadband All-photonic Transduction of Nanocantilevers." *Nature Nanotechnology* 4, no. 6 (2009): 377-82. doi:10.1038/nnano.2009.92.